

# Interactions between drifting snow and surface dynamics

THÈSE N° 8513 (2018)

PRÉSENTÉE LE 5 AVRIL 2018

À LA FACULTÉ DE L'ENVIRONNEMENT NATUREL, ARCHITECTURAL ET CONSTRUIT  
LABORATOIRE DES SCIENCES CRYOSPHERIQUES  
PROGRAMME DOCTORAL EN GÉNIE CIVIL ET ENVIRONNEMENT

ÉCOLE POLYTECHNIQUE FÉDÉRALE DE LAUSANNE

POUR L'OBTENTION DU GRADE DE DOCTEUR ÈS SCIENCES

PAR

Philip CRIVELLI

acceptée sur proposition du jury:

Prof. A. Berne, président du jury  
Prof. M. Lehning, directeur de thèse  
Prof. K. Nishimura, rapporteur  
Dr S. Horender, rapporteur  
Dr E. Paterna, rapporteur



ÉCOLE POLYTECHNIQUE  
FÉDÉRALE DE LAUSANNE

Suisse  
2018



who always does what he is already able to do  
always remains what he already is.  
— Henry Ford

To my wife Nora, the biggest inspiration in my life.



# Acknowledgements

During my thesis, I had the support of countless people helping me to bring this endeavor to a successful end. My supervisors, colleagues, but all so my family and friends outside academia.

First and foremost I want to thank Michi Lehning for his immeasurable effort and support, his excellent guidance, patience and enthusiastic motivation accompanying me through the last four and a bit more years. I wish to include in my acknowledgement Jessica Ritzi for her essential support dealing with all the bureaucracy at EPFL. Thanks also to Alexis Berne for presiding my examination as well as Enrico Paterna, Kouichi Nishimura and Stefan Horender for reviewing this thesis and being part of my examination committee.

A special thank belongs to Enrico Paterna for assisting me during most parts of my thesis. Thanks for all the fruitful discussions and the great atmosphere in the office, the wind tunnel and everywhere else. Without his support, this thesis could have become an invincible challenge. Furthermore I am thankful to Stefan Horender for writing the proposal for the funding of this study and his support during the early stages of my work. I also want to thank Charles Fierz for his inputs and support as the leader of the group I was working in as well as Christian Sommer for adding to the great atmosphere in the office and the wind tunnel. My thanks include my predecessor Benjamin Walter for the valuable discussions and appreciated inputs concerning my work and the life as a PhD at the institute.

I am also thankful to all my colleges and coworkers at the SLF for their time and smiles, the discussions in the office floors and on days out in the mountains or the streets. Thanks for having a great time at the SLF: Quirine Krol, Anna Haberkorn, Franziska Gerber, Florian Kobierska, César Vera, Nander Wever, Bert Kruyt, James Glover, Walter Steinkogler, Fabian Wolfesperger, Joel Fiddes, Sebastian Schlögl and many more.

My biggest thank goes to my family, my mother Heidi, my sister Janine and particularly my wife Nora. She was the person driving me through all the good and less good times the last few years. Furthermore I want to thank all my friends, be it from my youth, the time in the army, going to the mountains with or from elsewhere.

Last but not least I want to thank the Swiss National Science Foundation (SNF) for financing this project.

*Davos Dorf, December 2017*

Ph. C.



# Abstract

In the cryosphere, the snow cover is the fastest changing component. Amongst other characteristics, the snow cover acts as a resource of water or has the ability to reflect the sun's radiation and therefore significantly influence the climate on a global scale. During the winter period in the northern hemisphere, up to 23% of the earth's surface is covered with snow. In alpine regions starting at a certain elevation or at high latitudes, snow is the predominant state of the surface during winter time. Changes in the distribution of this snow cover are driven by different processes such as precipitation or melting. One main driver for the changes of this snow cover is aeolian transport, the transport of snow by the wind which is often referred to as drifting and blowing snow. In polar regions with predominant snow surfaces, little precipitation and subfreezing temperatures the redistribution of snow has a major role for the hydrological mass balance. Besides the redistribution of mass as a hydrological resource, in alpine regions, the redistribution of snow also has a major effect on the danger of avalanches.

Understanding how the snow surface responds to the forces of the wind is the key to understand the subsequent redistribution of the snow. Aeolian transport of snow has been previously described in literature, mainly focusing on the transport of the particles in the boundary layer, also with reasonable temporal resolution. Little attention has been given to the quantification of changes at the snow surface. This work takes a new approach to look at the changes of the snow surface in combination with the horizontal mass-flux during events of drifting snow. It aims to quantify these changes on a relatively high spatial and temporal resolution by means of a Kinect sensor.

This dissertation is divided in four sections. Chapter 1 introduces the concepts and theoretical background of drifting and blowing snow as well as outlining the thesis. Each subsequent chapter presents the main results as they have been or will be published in journal articles (Chapter 2-4).

In Chapter 2 we compare two of the most common methods of quantifying mass flux, particle numbers and particle-size distribution for drifting snow events, (i) the snow-particle counter (SPC), a laser-diode-based particle detector, and (ii) particle tracking velocimetry based on digital shadowgraphic imaging. The two methods were correlated for mass flux and particle number flux. A calibration study with artificially scattered sand particles and glass beads provides suitable settings for the shadowgraphical imaging as well as obtaining a first correlation of the two methods in a controlled environment. In addition, using snow collected in trays during snowfall, several experiments were performed to observe drifting snow events in a cold wind tunnel. The results demonstrate a high correlation between the

## Acknowledgements

---

mass flux obtained for the calibration studies ( $r \geq 0.93$ ) and good correlation for the drifting snow experiments ( $r \geq 0.81$ ). The study was designed and performed to optimize the settings of the digital shadowgraphic imaging system for both the acquisition and the processing of particles in a drifting snow event. The results suggest that these optimal settings can be transferred to different imaging set-ups to investigate sediment transport processes. This first study served as an introduction to the wind tunnel as well as it build confidence in the quality of the SPC device, which was used in all subsequent studies.

Chapter 3 presents the introduction of a new measurement tool to the wind tunnel. Prior to this study the quantification of snow transport in cold wind tunnels as well as in the field has often been performed with particle counting methods which are limited to sampling relatively small volumes at one point. These methods, which measure only horizontal mass fluxes, are unable to distinguish between erosion or deposition of snow. In order to quantify changes at the snow surface during events of drifting snow, the Kinect sensor was introduced as a new, low-cost tool enabling the recording of relatively high resolutions both in time and space which is unmatched by most other current methods. For the specific setting in our wind tunnel, we found that for low wind speeds, there is a balance between erosion and accumulation on the snow surface, while at higher wind speeds erosion dominates. The spectral analysis revealed significant differences in the power spectral density between the surface mass flux and the horizontal particle mass flux. We show that for the saltation-length-scale parameter  $\lambda = 1$ , the integrated particle flux can be used to estimate the total surface mass flux in the wind tunnel ( $r = 0.93$ ). These results serve as an important base to interpret mass flux measurements from the field in the next step.

In Chapter 4 we investigate and quantify the development of the snow surface in an alpine environment during an event of drifting and blowing snow using a Microsoft Kinect device. The results are compared to measurements of the surface change forced by drifting snow in controlled wind tunnel experiments. Finally the results are compared to similar developments of the snow surface influenced by precipitation and drifting particles on a scale up to a few hundred meters in Antarctica. In the spatial domain we find a strong streamwise variability in the dynamics of the snow height evolution. With respect to the temporal domain, after a few hours in the experiments, the changes in the snow height decrease from a centimeter-per-minute scale to millimeter-per-minute scale. Therefore we conclude that the potential of drifting and blowing snow to shape snow surface structures is strongly dependent on the drifting snow duration. For time scales in the range of days, sintering was found to increase the threshold of the snow to erosion. Relating the one-height flux measurement to the flux profile, it was found that a log-normal flux profile approximation is most reasonable across experiments from the diverse sites.

**Keywords.** Aeolian processes, Aerodynamic entrainment, Boundary-layer flow, Drifting and Blowing snow, Kinect, Mass flux, Particle transport, Saltation, Shadowgraphy, Turbulent boundary-layer, Snow deposition and erosion, Wind tunnel.



# Zusammenfassung

Die Schneedecke ist die am schnellsten ändernde Komponente in der Kryosphäre. Sie ist beispielsweise ein bedeutender Wasserspeicher oder besitzt die Eigenschaft Sonnenstrahlung zu reflektieren und damit massgeblich das Klima auf einer globalen Ebene zu beeinflussen. In alpinen Regionen ab einer gewissen Höhe oder genügend hohen Breitengraden ist die Oberfläche regelmässig und über längere Perioden mit Schnee bedeckt, so dass während der Wintermonate in der nördlichen Hemisphäre bis zu 23% der gesamten Erdoberfläche mit Schnee bedeckt sind. Änderungen in der Schneehöhenverteilung werden durch Prozesse wie Niederschlag oder Schmelze gesteuert. Eine weitere Einflussgrösse für solche Änderungen ist der Äolische Transport, das heisst der Transport von Schnee durch den Wind. Üblicherweise nennt man diesen Prozess Schneeverfrachtung. In Polarregionen welche ganzjährig mit Schnee bedeckt sind, wenig Niederschlag fällt und tiefe Durchschnittstemperaturen herrschen hat die Schneeverfrachtung einen grossen Einfluss auf die hydrologische Massenbilanz. Weiter hat nebst der Umverteilung von Schnee als Wasserressource hat die Schneeverfrachtung besonders in alpinen Regionen einen grossen Einfluss auf die Lawinengefahr.

Um die besprochene Verfrachtung zu begreifen ist es zentral zu verstehen, wie die Schneeoberfläche auf die durch den Wind induzierten Kräfte reagiert. Literatur zur Schneeverfrachtung beschränkte sich bisher auf den Partikeltransport in der atmosphärischen Grenzschicht, durchaus mit guter zeitlicher Auflösung. Wenig Beachtung wurde der Quantifizierung der Schneeoberflächen-Änderung geschenkt. Diese Arbeit nimmt einen neuen Ansatz die Änderungen der Schneeoberfläche in Anhängigkeit des horizontalen Massenflusses durch Schneeverfrachtung zu quantifizieren. Der Anspruch ist diese Änderungen in einer hohen räumlichen und zeitlichen Auflösung aufzuzeichnen. Um diesen Anspruch zu realisieren wurde mit dem Kinect ein neuer Sensor eingeführt.

Diese Dissertation ist in vier Teile aufgeteilt. In Kapitel 1 werden die Grundlagen und Konzepte zur Schneeverfrachtung erläutert und die folgenden Kapitel kurz erläutert. In den folgenden Kapitel (2 - 4) werden die Resultate präsentiert wie sie in wissenschaftlichen Artikeln präsentiert werden.

In Kapitel 2 vergleichen wir zwei der üblichsten Methoden zur Quantifizierung des Massenfluss, der Anzahl und Grössenverteilung der Partikel während der Schneeverfrachtung. Die erste Methode basiert auf einem Schnee-Partikel-Zähler (SPC), welche einem Laser-Dioden Detektor zur Zählung der Partikel nutzt. Die zweite Methode nennt sich Particle-Tracking-Velocimetry basierend auf digitalen Schattenbildern. Es wurde die Korrelation bezüglich Massenfluss und Anzahl Partikel untersucht. Ein Kalibrations-Experiment mit künstlich gesiebten

## Acknowledgements

---

Sandpartikeln und Glaskügelchen lieferte erste Resultate für die optimalen Einstellungen der Bildanalyse der Schattenbilder. Nach den Kalibrations-Experimenten wurden Experimente mit Verfrachtung von natürlichem Schnee im Windkanal durchgeführt. Die Resultate zeigen eine hohe Korrelation für den Massenfluss in den Kalibrationsexperimenten ( $r \geq 0.93$ ) und eine gute Korrelation für die Experimente mit natürlichem Schnee ( $r \geq 0.81$ ). Ziel dieser Studie war es optimale Einstellungen für Erfassung und Nachbearbeitung der digitalen Schattenbilder zu finden. Die Resultate suggerieren dass diese Einstellungen allgemeine Gültigkeit besitzen und somit auch auf ähnliche Bildgebungsmethoden zur Quantifizierung von Sedimentverfrachtung angewendet werden können. Ausserdem diene diese Studie im Rahmen der Dissertation dazu, den Windkanal besser kennenzulernen und Vertrauen und Erfahrung im Umgang und der Interpretation der Resultate des SPC zu erhalten, denn dieses Instrument wurde auch in allen folgenden Studien verwendet.

Kapitel 3 präsentiert die Einführung eines neuen Instruments in den Windkanal. Bis anhin wurde die Quantifizierung der Schneeverfrachtung sowohl im Windkanal als auch im Feld durch Zählung der Partikel gemacht. Methoden für diese Partikel-Zählung sind üblicherweise an eine fixe Höhe und ein kleines Kontrollvolumen gebunden. Ausserdem messen diese Methoden einzig Partikel in der Saltation ohne Erosion und Deposition an der Oberfläche zu betrachten. Um die Änderungen an der Schneeoberfläche während der Schneeverfrachtung zu quantifizieren wurde der Kinect Sensor als ein neues, kostengünstiges Instrument eingeführt. Dieses Instrument ermöglicht zum ersten Mal eine Quantifizierung der Änderungen in hoher zeitlicher und räumlicher Auflösung, unerreicht durch andere Methoden. Basierend auf den Eigenschaften des Windkanals fanden wir dass sich die Schneeverfrachtung bei wenig Wind im Gleichgewicht zwischen Erosion und Ablagerung befindet während bei höheren Windgeschwindigkeiten die Erosion überwiegt. Die Spektralanalyse zeigt signifikante Unterschiede in der spektralen Leistungsdichte zwischen dem Oberflächen-Massenfluss und dem horizontalen Partikel-Massenfluss. Wir zeigen auf, dass für einen Saltationslängen-Parameter von  $\lambda = 1$ , der integrierte Partikel-Massenfluss zur Abschätzung des Oberflächen-Massenfluss im Windkanal genutzt werden kann ( $r = 0.93$ ). Die Resultate dieser Studie dienen als wichtiger erster Schritt für die Interpretation künftiger Experimente zur Schneeverfrachtung im Feld.

In Kapitel 4 untersuchen und quantifizieren wir Entwicklung der Schneeoberfläche auf einem Versuchsfeld in den Alpen während einem Schneesturm Ereignis. Dabei nutzen wir ein Microsoft Kinect Gerät um zeitlich und räumlich hochaufgelösten Messungen einer kleinen Oberfläche der Schneedecke aufzunehmen. Diese Resultate werden mit Messungen von Niederschlag und Schneeverfrachtung auf einer Fläche von einigen hundert Metern in der Antarktis verglichen. Räumlich betrachtet zeigt sich, dass die Dynamik der Schneehöhenänderung hauptsächlich in Strömungsrichtung variiert. Zeitlich betrachtet reduziert sich die Amplitude der Änderungen nach einigen Stunden andauernder Schneeverfrachtung von einer Skala Zentimeter/Minute zu Millimeter/Minute. Dies zeigt auf, dass das Potenzial zur Schneehöhenänderung stark von der Dauer der Schneeverfrachtung abhängt. Ausserdem suggerieren unsere Resultate das die Modellierung des Massenfluss-Profils anhand einer Exponentialfunktion wie es in der Literatur vorgeschlagen zwar Gültigkeit hat für die Saltation in einem Windkanal, jedoch Einschränkungen für die Saltation im Feld bestehen, weshalb wir

eine Log-Normal Funktion als realistischere Methode vorschlagen.

**Schlüsselwörter.** Ablagerung und Erosion, Äolischer Transport, Aerodynamische Verfrachtung, Digitale Schattenbildanalyse, Grenzschichtströmung, Kinect, Massenfluss, Partikel Transport, Saltation, Schneeverfrachtung, Turbulente Grenzschicht, Windkanal.



# Contents

<b>Acknowledgements</b>	<b>v</b>
<b>Abstract (English/Deutsch)</b>	<b>vii</b>
<b>List of figures</b>	<b>xiv</b>
<b>List of tables</b>	<b>xvi</b>
<b>1 Introduction</b>	<b>1</b>
1.1 Motivation . . . . .	1
1.2 Background . . . . .	3
1.2.1 Turbulent boundary layer and aeolian transport . . . . .	3
1.2.2 Particle counting methods . . . . .	4
1.2.3 Quantifying snow surface changes . . . . .	6
1.3 Purpose and outline . . . . .	7
<b>2 Quantifying Particle Numbers and Mass Flux in Drifting Snow</b>	<b>9</b>
2.1 Introduction . . . . .	9
2.2 Instrumentation and Methods . . . . .	10
2.2.1 Snow-particle counter . . . . .	10
2.2.2 Particle tracking velocimetry based on shadowgraphic images . . . . .	11
2.2.3 Experiments . . . . .	16
2.3 Results . . . . .	19
2.3.1 Calibration experiment . . . . .	19
2.3.2 Number of particles . . . . .	28
2.4 Discussion . . . . .	31
2.4.1 Particle recognition, particle property and particle filter . . . . .	31
2.4.2 Sensitivity of the field-of-view . . . . .	33
2.4.3 Mass flux, particle diameter and particle numbers . . . . .	33
2.4.4 Diameter interpretation and spherical assumption . . . . .	34
2.5 Conclusions . . . . .	35
<b>3 Space - time dynamics of erosion/deposition versus horizontal mass flux of snow</b>	<b>37</b>
3.1 Introduction . . . . .	37
3.2 Methods and Instrumentation . . . . .	38

## Contents

---

3.2.1 Experiments . . . . .	40
3.3 Results and Discussion . . . . .	46
3.3.1 Set-averaged and time-averaged mass-flux . . . . .	49
3.3.2 Spectral distribution . . . . .	51
3.4 Conclusions . . . . .	53
Appendices . . . . .	56
A Surface area reduction . . . . .	56
B Saltation length scale . . . . .	58
<b>4 Spatiotemporal dynamics of short term erosion/deposition in drifting and blowing snow</b>	<b>61</b>
4.1 Introduction . . . . .	61
4.2 Methods and Instrumentation . . . . .	63
4.2.1 Wind tunnel . . . . .	63
4.2.2 Field experiments . . . . .	64
4.2.3 Kinect mass-flux data . . . . .	67
4.2.4 SPC mass-flux computation . . . . .	67
4.3 Results and Discussion . . . . .	73
4.4 Conclusions . . . . .	83
<b>5 Overall summary and conclusions</b>	<b>87</b>
<b>6 Limitations and outlook</b>	<b>91</b>
<b>Glossary</b>	<b>97</b>
<b>Bibliography</b>	<b>107</b>
<b>Curriculum Vitae</b>	<b>109</b>

# List of Figures

1.1	Drifting snow . . . . .	2
1.2	Aeolian transport and boundary layer . . . . .	3
2.1	Sketch of the wind tunnel . . . . .	12
2.2	Detail of a raw image . . . . .	14
2.3	Particle velocity calculation . . . . .	15
2.4	Image after processing steps . . . . .	17
2.5	Image of the calibration study . . . . .	18
2.6	Particle-size distribution of the calibration experiment . . . . .	20
2.7	Results of experiment C1 . . . . .	22
2.8	Results for the calibration experiment - C1, C2, C3 . . . . .	23
2.9	Results for the calibration experiment - PR, PP, PF . . . . .	24
2.10	Results for the calibration experiment - FOV ratio . . . . .	26
2.11	Results of experiment D1 . . . . .	27
2.12	Results for the drift experiment - D1, D2, D3 . . . . .	29
2.13	Results for the drift experiment - FOV ratio . . . . .	30
2.14	Number-flux time series signal . . . . .	32
3.1	Sketch of the wind tunnel . . . . .	39
3.2	Kinect calibration setup . . . . .	42
3.3	Kinect erosion depth . . . . .	43
3.4	Procedure to calculate the saltation footprint length . . . . .	45
3.5	Low and high mass flux example . . . . .	47
3.6	Mass flux time series . . . . .	49
3.7	Correlation between $Q_S$ and $Q_P$ . . . . .	50
3.8	Power spectral density for reduction different factors . . . . .	52
3.9	Power spectral density for high, intermediate and low mass flux . . . . .	53
3.10	Unnormalized power spectral density . . . . .	54
4.1	Weather station in Antarctica . . . . .	66
4.2	Mass flux profile functions . . . . .	69
4.3	Integrated mass flux profile function . . . . .	70
4.4	Time series of particle mass flux on Weissfluhjoch . . . . .	73
4.5	Time series of meteorological data on Weissfluhjoch . . . . .	74

## List of Figures

---

4.6	Histogram of the average surface mass flux . . . . .	75
4.7	Surface mass flux on Weissfluhjoch . . . . .	75
4.8	Time series of the snow height . . . . .	76
4.9	Time series of the snow height for the sub grid . . . . .	76
4.10	Box plot for the the mass flux and the shear velocity . . . . .	78
4.11	Box plot for the surface mass flux histogram . . . . .	79
4.12	Box plot with the integral time scales . . . . .	80
4.13	Histogram of the surface height change in Antarctica . . . . .	81
4.14	Surface height change in Antarctica . . . . .	82
4.15	Time series of particle mass flux in Antarctica . . . . .	84
4.16	Time series of meteorological data in Antarctica . . . . .	84



## List of Tables

2.1	Parameter thresholds settings . . . . .	16
2.2	Conditions and settings of the drifting experiment . . . . .	19
3.1	Experiments in the winter season 2016 . . . . .	40
3.2	Statistics of the two sets displayed in Fig. 3.5. On test day 1, the threshold wind speed was $t$ 9.45 m/s. . . . .	46
3	Correlation of particle mass flux and set-averaged surface mass flux for different reduction factors. . . . .	56
4	Correlation of particle mass flux and time-averaged surface mass flux for different reduction factors. . . . .	57
5	Values for $\lambda$ given in literature and the resulting mean L-Value. . . . .	58
6	Linear regression coefficients for particle mass flux and set-averaged surface mass flux for different $\lambda$ . . . . .	59
7	Linear regression coefficients for particle mass flux and time-averaged surface mass flux for different $\lambda$ . . . . .	60
4.1	Wind-tunnel experiments in the winter season 2016 and 2017 . . . . .	64
4.2	Field experiments on WFJ in the winter season 2017. The average wind speed was calculated from the CSAT3B sensor. . . . .	65
4.3	Dates of the TLS scans in PEA together with the average height change compared to the previous scan. . . . .	66
4.4	Snow densities as recorded for experiments in PEA . . . . .	67
4.5	Correlation table for the results in the field . . . . .	77
4.6	Correlation table for the results in the wind tunnel . . . . .	79
4.7	Result from TLS scans volume change from PEA . . . . .	81



# 1 Introduction

## 1.1 Motivation

Drifting snow is a phenomena that occurs often and globally. Drifting snow and its accumulation have various effects. They may affect traffic, when drift accumulations block roads or when blowing snow leads to poor visibility. In mountainous terrain, snow drift increases the risk of avalanches. Drifting and blowing snow also has an impact on the mass balance in polar ice sheets and glaciers. Eisen et al. [2008] concluded that drifting snow together with sublimation are key variables for the surface mass balance in East Antarctica. Large areas have a close to zero mass balance. Since melting plays a minor role in this region [Vaughan, 2006], drifting snow and sublimation equal the net precipitation. The process of drifting snow is not only relevant for transporting snow, but it also shapes the remaining surface. Bedforms shaped by drifting snow influence the surface roughness and therefore the momentum transfer between atmosphere and sea ice [Castellani et al., 2014, Amory et al., 2017].

Various studies have studied the snow surface shapes resulting from drifting snow [Cornish, 1914, Kobayashi and Ishida, 1979, Filhol and Sturm, 2015]. Few studies have investigated the spatial and temporal variability of drifting fresh snow particularly including the changes at the surface. Research on saltating systems over the last years clearly shows that the variability of this process has to be understood before reliable models can be developed [Kok and Renno, 2009, Bernhardt et al., 2010, Mott et al., 2010, Schneiderbauer and Prokop, 2011]. Our research focused on the relation between the mass flux estimated by the particles in the saltation layer and the dynamics of erosion and deposition of the snow surface. At the same time, in the same wind tunnel, experiments investigating the relative role of turbulence on the variability of drifting snow mass flux were conducted [Paterna et al., 2016, 2017]. Details to this work are presented at the end of Chapter 5.

After the pioneering research of [Bagnold, 1935] many contributions have been made to the problem of particle drift induced by wind. Models have been developed and validated for controlled flows like those produced in wind tunnels. These models started with simple models considering an expression for the entrainment rate and the modification of the wind



Figure 1.1: Drifting and snowing snow in the mountains during a Föhnsturm.

velocity profile by saltating particles to express a steady state mass flux [Anderson and Haff, 1988]. The models were developed introducing Lagrangian stochastic models [Nemoto and Nishimura, 2004] or other approaches which claim to reproduce a wide variety of experimental data, including vertical and horizontal profiles of the particle mass flux [Kok and Renno, 2009]. This latter model has a large uncertainty since more than 10 parameters have to be taken from measurements which can have a sensitive impact on the model performance. Such models have been extended to atmospheric models. Such models are used to calculate the redistribution of snow [Bernhardt et al., 2010] and can reproduce the trends of the snow cover [Mott et al., 2010], however accurate quantitative modeling is still challenging.

Based on the implementation of new infrastructure such as a low cost three dimensional scanner, the evolution of the snow surfaces during drift events can be investigated. This implementation was combined with measurement techniques such as snow particle counting (SPC) and shadowgraphic particle tracking imagery, to characterize the spatial and temporal variability in the snow mass flux, both in the boundary layer above the snow surface based on the drifting particles as well as based on the resulting change of the surface.

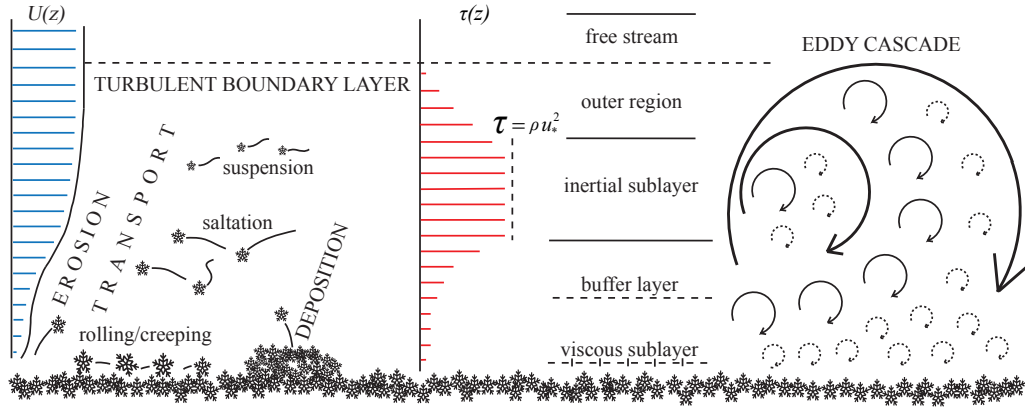


Figure 1.2: Drawing of the aeolian transport in a turbulent boundary layer.

## 1.2 Background

### 1.2.1 Turbulent boundary layer and aeolian transport

The atmospheric boundary layer is the lowest part of the atmosphere. It's defined as the layer between the earth's surface and the free atmosphere. Depending on time and location its height varies between less than 100 m to 3000 m. Daily living takes place within it. The conditions within the boundary layer are influenced by the earth's surface and its response to forcing such as frictional drag, heat transfer and many more [Stull, 2012]. In comparison to the predominantly laminar flow in the free atmosphere, the characteristic winds in the boundary layer consist of turbulent eddies. These eddies are formed by the forcing from the ground. The largest eddies scale with the depth of the boundary layer. Within the boundary layer the large eddies cascade to smaller and smaller eddies and within this process until the turbulent kinetic energy dissipates to viscosity at the Kolmogorov scales (ref. Fig.1.2).

The turbulent boundary layer is divided in different layer [Schlichting et al., 1955]. The layer closest to the wall is the viscous sublayer. Within this layer, the viscous forces dominate the turbulent forces. The shear stress in this layer is linear with the distance from the surface. Its size is depending on the surface roughness. Adjacent to the viscous sublayer is the buffer layer. This region builds the transition from the viscous sublayer to the next layer. The velocity and shear stress profile change from a linear relation with the distance from the wall to a more logarithmic profile. On top of the the buffer layer is the inertial sublayer. This layer is also named the 'constant shear stress layer' due to the fact that the shear stress in this layer remains

## Chapter 1. Introduction

---

constant ( $\tau = \rho u_*^2$ ,  $\rho$  = fluid density,  $u_* = \langle -u'v' \rangle^{1/2}$  the friction - or shear stress velocity). Within this layer, the mean velocity profile can be approximated by the 'law of the wall'

$$u(z) = \frac{u_*}{\kappa} \ln\left(\frac{z}{z_0}\right), \quad (1.1)$$

with  $\kappa$  the being the von Karman constant and  $z_0$  the aerodynamic roughness length.

In the outer layer, the shear stress decreases towards zero. Other characteristics in this layer are a low velocity gradient, and a mean velocity near the freestream velocity.

Aeolian transport is the process of unconsolidated sediments moving by the wind. Sediments include sand, dust, clay and snow. For the aeolian transport to be initiated, the surface shear stress has to exceed a certain threshold to entrain sediment particles into the flow.

The process has the power to shape the surface. For the case of snow we find on smaller scales deposition type forms such as surface ripples [Cornish, 1914, Kobayashi and Ishida, 1979, Kosugi et al., 1992] and erosion type forms as sastrugi [Cornish, 1914]. On larger scales we find deposition type forms like snow dunes [Frezzotti et al., 2002b,a, Dadic et al., 2013], barchans [Kobayashi and Ishida, 1979] and cornices [Mott et al., 2010]. Further there are forms like snow waves that represent a combination of erosion and deposition [Kobayashi and Ishida, 1979]. The process is divided into the three modes; suspension, saltation and creep which depend predominantly on particle size of the sediment and the power of the wind (refer to Kok et al. [2012]).

- In the suspension mode the particles are fully airborne for a long period of time. These particles are generally small ( $<70 \mu\text{m}$ ).
- In saltation mode the fluid drag exerts sufficient force on the sediments to allow them to hop along the surface in parabolic trajectories. This mode is confined between a few centimeters to a few meters from the snow surface, depending on the overall height of the boundary layer and the turbulent eddies. Saltation is triggered by two mechanisms of particle entrainment: Aerodynamic entrainment, when the wind has sufficient momentum to lift snow crystals from the surface and splash entrainment, when the saltation is initiated (or maintained) through impacting or rebounding particles [Kok et al., 2012, Paterna et al., 2017].
- In creep mode large particles predominantly roll and slide along the surface.

### 1.2.2 Particle counting methods

Within the history of this field of research, various methods for the quantification of particles and particles mass-fluxes have been developed. There are two main categories, optical meth-

ods and mechanical methods. Within this chapter, we present two optical methods: particle tracking based on shadowgraphic imaginary and laser diode based particle counters. The mechanical devices presented subsequently include an acoustic sensor (FlowCapt), as well as particle traps.

Particle tracking method makes use of a light source and a high speed camera on the opposite side. The shadow created by particles flying through the line of sight of the camera and the light source enables to recorded and evaluated particles based on their size and velocity, assuming the speed to record the particles is high enough and the resolution to characterize the particles is sufficient. Different manufacturers distribute commercial systems and solution which can be tailored for such applications. In the SLF wind tunnel, a Swiss National Foundation (SNF) grant allowed the installation of shadow graphic measurement technique from LaVision GmbH in 2013. Based on this installation, several studies were published making use of this technique [Gromke et al., 2014, Pokorny and Horender, 2014, Crivelli et al., 2016, Paterna et al., 2016, 2017].

The laser diode based particle counter was first introduced by Schmidt [1977]. Similar to the shadowgraphic imaginary, the system makes use of a light source (laser in this case) and a phototransistor. Based on the voltage change in the phototransistor the instrument can estimate the size of the particles that are causing this voltage change. This device was further developed mainly by Japanese researchers [Kimura, 1993] and widely used in several studies, both in wind tunnel [Nishimura et al., 1998, Sugiura et al., 1998, Clifton et al., 2006, Guala et al., 2008] as well as in field studies [Nishimura and Nemoto, 2005, Gordon and Taylor, 2009, Gordon et al., 2009]. For our research, we had a SPC-S7 version installed in the wind tunnel and a SPC-95 version was used in the field studies.

The first mechanical system discussed is the FlowCapt device [Chritin et al., 1999]. This device consists of a acoustic enclosure containing microphones. The device measures the wind velocity and particle mass flux based on the induced acoustical pressure, either trough the shocks of the particles or the wind. The summation of all signals over the height of the enclosure delivers a quantification of the particle mass flux. The advantage of this device is that it has a larger measurement volume within the saltation layer at a decent temporal resolution. But this device also lacks vertical resolution and cannot determine the particle size distribution. One large disadvantage is that the calibration is not reliable and absolute mass fluxes are therefore difficult to obtain [Lehning et al., 2002, Naaim-Bouvet et al., 2010].

Another commonly used particle flow measurement tool are flow compartment traps [Mellor, 1960, Budd et al., 1966, Takeuchi, 1980, Lehning et al., 2002, Ni et al., 2003]. The device is build as a stack of compartments vertically aligned. It is placed in a wind tunnel or in to the field. The sediments in the saltation layer are trapped within the compartments. After the event or the test, the contents of the compartments can be weighted and analyzed. This device allows defining vertical profiles and a extended particle size distribution, but it lacks of a temporal resolution as well as it needs much effort to retain and analyze the particles. This excludes the

method from long-term saltation monitoring.

Within the scope of this thesis, only the two optical devices were analyzed in detail. More details about these two systems are published in Chapter 2. The presented methods may not represent all available methods, but they give an overview over the most commonly used.

### 1.2.3 Quantifying snow surface changes

Quantification of the snow surface changes are performed by calculating the differences between consecutive measurements of the snow surface. The measurements can either be single-point measurements or based on a defined area.

Within this chapter an overview over commonly used methods is given. The oldest and most simple method is manual probing. It has the advantage of being applicable in almost all conditions and easy to perform by anyone. The disadvantages are lack of spatial and temporal resolution. Furthermore probing is destructive since it alters the snow surface. Probing generally involves much physical (often dangerous) work.

The other methods can be summarized by remote sensing or non-contact applications. These methods include measurements using radar, laser, structured light, ultrasonic or infrared signals. Another technique is the surface reconstruction using photogrammetry.

Three methods will be discussed subsequently; the terrestrial laser scanning, photogrammetry and a particular method using infrared light.

Terrestrial laser scanning (TLS) has become a popular method for terrain surveying measurements [Lemmens, 2011]. The principle of TLS is to actively emit a laser beam on a geometrical raster to measure the distance to an object or a scene at each position of the raster. The distance measuring with a laser sensor is based on different principles that vary based on the manufacturer of the TLS device. They include phase shift, pulse measurements, optical triangulation and interferometry [Colombo and Marana, 2010]. Applications of TLS are widespread and reach from city modeling to the observation of deformations of relevant constructions or mountainsides. In the context of snow surfaces measurements an example of an application can be found in Grünwald et al. [2010] where they measured the variability of the snow depth. Within this manuscript we will also provide an example of the use of TLS in chapter 4.

The American society for photogrammetry and remote sensing defines photogrammetry as the art, science and technology of obtaining reliable information [...] by interpreting photographic images [...]. For the 3-dimensional reconstruction of the snow surface, more specifically stereophotogrammetry can be applied. This method involves the reconstruction of the geometry by two or more photographic images. In the images, common points are identified and the geometry is reconstructed from the camera location. Obviously for this process, the position of the camera and its orientation with respect to the objects in the image need to be known a priori to calibrate the measurements.



The last method presented are infrared (IR) distance measurement. This method uses triangulation based on two units, an infrared emitter and a infrared receiver (PSD - position-sensible photo detector). A reflected infrared signal generates a conductivity on the PSD, which is converted to a voltage signal. The signal is digitalized and can be converted in a distance between object and IR emitter. Microsoft created a device named *Kinect* which uses a pair of IR emitter and PSD to generate an infrared pattern. Similar to the TLS, the IR pattern is applied on raster. The Kinect works similarly to a 3D scanner using a IR distance measurement system. The application is much cheaper than a TLS but also has only a very limited range compared to a TLS. The work presented in chapters 3 and 4 uses such a Kinect device as a tool to quantify the surface change.

## 1.3 Purpose and outline

This study aims at investigating the dynamics of erosion and deposition on the snow surface in relation to the snow transported in the saltation layer. The work also aims at understanding the characteristics of snow mass transport in events of drifting and blowing snow and how they spatially and temporally interact with the snow surface, both in wind tunnel experiments as well as in the field. For that purpose new, innovative measurement techniques was introduced and compared to traditional, robust measurement systems.

The main objectives of this work can be outlined as follows:

1. Compare a traditional device to quantify particle numbers and mass flux in drifting snow with a new, image-based method for the saltation layer for wind tunnel studies.
2. Introduce a new, innovative device to record and quantify the dynamics of changes on the snow surface in comparison with particle measurements in the saltation layer.
3. Analyze data recorded on a alpine field site to wind tunnel measurements with respect to spatiotemporal dynamics of erosion and deposition as well as apply the results to an Antarctic measurements campaign using TLS scans.

The three objectives were treated in peer-reviewed journal articles. In this thesis, each publication is presented in a separate Chapter:

- Chapter 2: Quantifying Particle Numbers and Mass Flux in Drifting Snow

*P. Crivelli, E. Paterna, S. Horender, and M. Lehning. Quantifying particle numbers and mass flux in drifting snow. Boundary- Layer Meteorology, June 2016. doi: 10.1007/s10546-016-0170-9.*

In this chapter we focus on the quantification of the mass flux in the saltation layer. We compare the results of the snow particle counter to data of the image-based Shad-

## Chapter 1. Introduction

---

owgraphy method. We also give an overview how settings in the post-processing of the shadowgraphy influence the results of the mass-flux calculation.

- Chapter 3: Space - time dynamics of erosion/deposition versus horizontal mass flux of snow

*P. Crivelli, E. Paterna, and M. Lehning. Space - time dynamics of erosion/deposition versus horizontal mass flux of snow. Journal of Glaciology, December 2017. [in revision].*

Here we focus on the comparison between mass-flux in the saltation and the actual change of mass at the snow surface. We investigate differences and similarities between the two processes.

- Chapter 4: Spatiotemporal dynamics of short term erosion/deposition in drifting and blowing snow

*P. Crivelli, E. Paterna, N. Wever and M. Lehning. Spatiotemporal dynamics of short term erosion/deposition in drifting and blowing snow. tbd, December 2017. [submitted].*

Based on the results of the previous chapter, the snow surface erosion processes are recorded in the field. The results are discussed in relation to the wind tunnel results. This knowledge is then applied to records from Antarctica.

Each of the described chapter contains a introduction to the topic as well as detailed information to the methods. The results are discussed in detail in the corresponding chapters. An overall summary and conclusion are subsequently discussed in Chapter 5. Limitations of the presented studies as well as an outlook are presented in Chapter 6.

## 2 Quantifying Particle Numbers and Mass Flux in Drifting Snow

### 2.1 Introduction

Drifting and blowing snow are phenomena that occur often and globally; they have an effect on traffic, when drift accumulations block roads or parts of airports, or when blowing snow leads to poor visibility. Snow transport increases the risk of avalanches in mountainous terrain Schirmer et al. [2009] or has an impact on mass balances in polar ice sheets and glaciers Groot Zwaaftink et al. [2013]. The physical process behind the drifting of snow is called saltation (see the pioneering work of Bagnold [1935]). Much research has been published since then, most often on the saltation of sand. Several methods to quantify particle number flux and mass flux within the atmospheric boundary layer have been described, such as particle counters Nishimura et al. [1998], Sugiura et al. [1998], flow compartment traps Schmidt [1986] and methods based on shadowgraphic particle tracking velocimetry (PTV; Gromke et al. [2014]). Another approach uses numerical simulations Doorschot et al. [2004]. Generally, similar methods to quantify drifting snow can be applied to many materials, such as sand or other wind-entrained particles. The physical processes are similar for these materials, with differences generally caused by the material properties. The aim of the present study is to quantify drifting snow with two of the most common and most recently used methods, the snow-particle counter (SPC) and shadowgraphic PTV. To the authors knowledge, no comparison between SPC method and any other imaging technique has been published. Results of a preliminary study conducted by the authors revealed a very weak correlation between the SPC and the PTV methods. A major problem was that the parameters for the post-processing of the PTV images need appropriate tuning to obtain a reliable estimate of absolute mass flux values. We present a parameter set is appropriate for the PTV method for drifting snow and further explain how results of a pointwise measurement such as the SPC correlate to what can be seen in the images recorded with shadowgraphic PTV. The SPC, which provides total mass flux of snow and the particle-size distribution at a frequency of 1 Hz is taken as a reference for the mass flux. Based on this (arbitrary) reference, the PTV settings are optimized in order to achieve maximum correlation with the SPC signal. The term arbitrary is used because the SPC can only be calibrated using metal wires of a certain diameter, and not

with snow or other similar particles.

### 2.2 Instrumentation and Methods

The experiments were carried out in the wind tunnel of the WSL Institute for Snow and Avalanche Research, SLF in Davos. The wind tunnel is situated in an unheated concrete building in the Flüelatal, Davos, Switzerland at 1670 m a.s.l. This particular wind tunnel has been described in Clifton et al. [2006, 2008], Guala et al. [2008], Burri et al. [2011], Gromke et al. [2011], Walter et al. [2012c,a,b], Pokorný and Horender [2014], Gromke et al. [2014], Walter et al. [2014], Paterna et al. [2016]. The wind tunnel is 14 m long, with a  $1\text{ m} \times 1\text{ m}$  cross-section. At the inlet a honeycomb grid and a 4:1 contraction are placed upstream of the test section while spires mounted on the floor downstream of the contraction create large-scale turbulence. Downstream of the spires, a 6 m region of regular roughness elements is mounted on the floor. The wind tunnel operates in suction mode drawing air through the inlet (refer to Fig. 2.1a).

Natural snow is collected outside of the wind tunnel in trays during snowfall events. The trays are positioned on the wind-shaded and sun-shaded sides of the wind tunnel such that disturbances during the accumulation of natural snow are reduced. As soon as the depth of fresh snow on the trays reaches between 0.07 - 0.15 m, the trays are positioned into the wind tunnel with as little disturbance as possible. The floor in the wind tunnel can be vertically adjusted such that the depth of the snow cover matches the height of the floor and the roughness elements in the upwind end of the wind tunnel, as well as the light and the camera system in the measurement section at the downwind end of the tunnel. Previous experiments conducted in the same wind tunnel reported a boundary-layer depth of approximately 0.25 m Clifton et al. [2006].

#### 2.2.1 Snow-particle counter

The first snow-particle counter was introduced by Schmidt [1977] and the concept developed further by Kimura [1993] to the well-established version SPC - S7 (Niigata Denki Co.) Many studies using this technique were performed in the past (see e.g. Nishimura et al. [1998], Sugiura et al. [1998], Doorschot et al. [2004], Nishimura and Nemoto [2005], Clifton et al. [2006], Guala et al. [2008], Gordon and Taylor [2009], Gordon et al. [2009], Zwaafink et al. [2014]). The working principle is based on a focused light emitter and photodiode that detects the shadows of particles drifting through the control volume ( $2\text{ mm} \times 25\text{ mm} \times 0.5\text{ mm}$ ). Based on the amplitude of the photodiode's voltage signal it is possible to classify the snow-particle diameter as one of 32 particle diameter bin classes between 0.04 mm and 0.5 mm (assuming that the particles are spherical). Detected particles with a diameter larger than 0.5 mm are assigned to the largest diameter bin, while their exact diameter remains undetermined. The raw signal is sampled at 40 kHz. Particle numbers with the corresponding diameter class are used to calculate the mass flux. For the three parameters - particle number - particle diameter - mass flux, the 1-s averaged signal is delivered as an output based on the

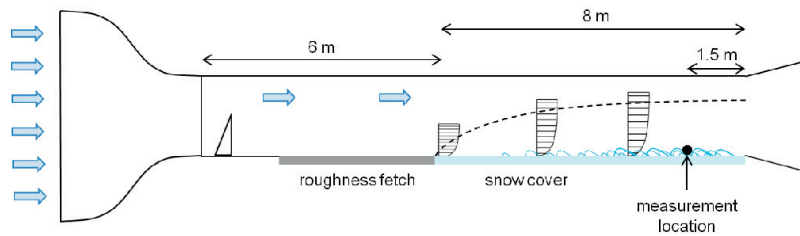
manufacturer's software. Before the experiments described herein the device was recalibrated by the manufacturer. For the experiments, the SPC was mounted on a traverse that allowed positioning in three dimensions in the wind tunnel test section.

### 2.2.2 Particle tracking velocimetry based on shadowgraphic images

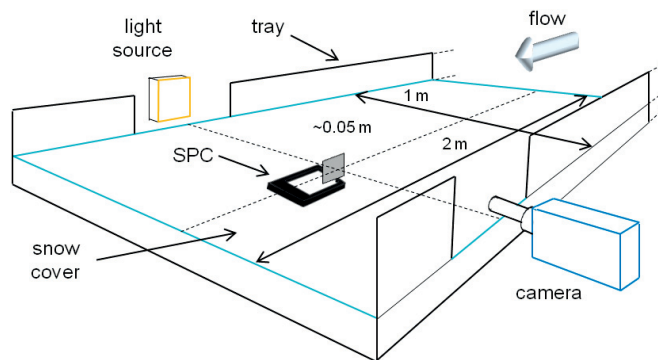
The second measurement technique employed to determine the mass flux of drifting snow (or sand) is PTV based on shadowgraphic imaging. The shadowgraphic system consists of a light source (standard 500 W halogen) and a high speed CMOS camera (1024 pixel  $\times$  1024 pixel) equipped with a telescopic lens (Nikon, focal length = 80 - 180 mm). Unlike the pointwise measurement of the SPC, the PTV method is able to record series of two-dimensional images of drifting snow particles. Alongside the information about particle numbers, size distribution and mass flux, the PTV image analysis allows visual inspection of the processes in the saltation layer. This facilitates the understanding of processes in the lowest part of the boundary layer and enables a deeper analysis of the saltation processes (for a schematic drawing of the set-up, refer to Fig. 2.1b).

Camera and light source are positioned outside of the wind tunnel's sidewalls, perpendicular to the flow direction such that they add no disturbance to the flow. To allow vertical adjustment of the field-of-view, the camera is mounted upon a translation stage. A translucent paper and a Fresnel lens with a focal length of 35 mm are mounted in front of the light source to diffuse the light and parallelize the light rays. Prior to every experiment, the camera has to be focused and calibrated by means of a transparent ruler placed into the field-of-view. The image calibration and acquisition was managed with LaVisions's Davis 8.2 software. For all the experiments performed, the pixel length corresponds to approximately 50  $\mu\text{m}$ , resulting in an approximate field-of-view of 50 mm  $\times$  50 mm. In order to obtain high speed images, the recorded images are initially saved on the RAM of the camera and afterwards stored onto the hard disk. The RAM allows recording up to 5456 images at the maximum resolution of 1024 pixels  $\times$  1024 pixels.

The PTV set-up acquires images along a two-dimensional domain parallel to the flow direction. The third dimension is the depth of the domain, also referred as depth-of-field, where the particles are detected. The depth-of-field can be quantified since increasing distance from the focal plane causes particles to become increasingly blurred. The size of the depth-of-field linearly decreases with decreasing particle size (for an illustration of this dependency, refer to Kim and Kim [1994], Fig. 7). The slope of this linear function depends on the depth of focus, which is limited by the camera settings (aperture, for all experiments on focal length  $f/8$ ) as well as by the parameters in the post-processing. For the calculation of mass flux and volume flux, the depth-of-field was accurately calibrated by means of a target image with a matrix of dots with diameters between 50  $\mu\text{m}$  and 1 mm. This target image was placed on a transparent plate in the middle of the field-of-view and translated towards the camera across the depth of focus with steps of 1 mm for a total of 60 mm centered on the depth of focus of the camera. Based on the recognition of the different particle sizes at different distances from the focal



(a)



(b)

Figure 2.1: Sketch of the wind tunnel (a), sketch of the PTV set-up in the wind tunnel (b) adapted after Paterna et al. [2016].

plane, the slope of the linear relation between particle diameter and depth-of-field could be calculated. The processing of the depth-of-field calibration was performed according the instructions in the software manual LaVision-GmbH [2011].

### Post-processing

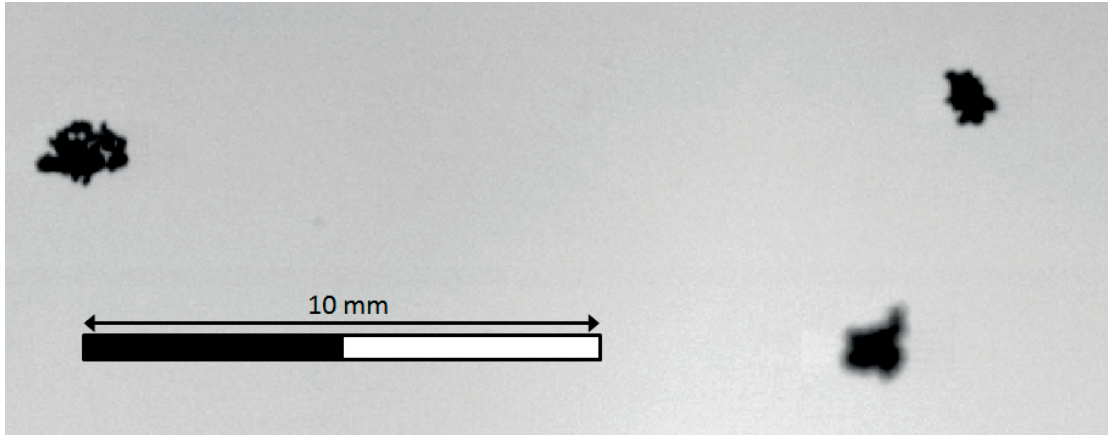
For the calculation of the velocity and the properties of the particles, a post-processing based on the recorded pictures was performed. The post-processing of the images identified the individual particles and their properties within each image (the settings of each parameter for the parametric study are explained in the following Sect. 2.2.3). The individual steps for the post-processing are as follows,

- Prior to the first segmentation, the raw images are inverted. For this purpose, the shadow images are subtracted from a reference image. The reference image is produced by a sliding maximum filter such that it represents the background image without particles. In the inverted image, the particles appear brighter than the background.

$$InvertedImage = ReferenceImage - ShadowImage$$

- Based on that inverted picture, a particle-recognition filter is applied. Applying this filter, a global threshold as a percentage between the maximum and the minimum light intensity within each image is defined. The algorithm attempts to find coherent areas above that threshold and defines them as particles (refer to Fig. 2.2a for the raw image and to Fig. 2.2b for the image after the particle-recognition filter).
- The second segmentation analyzes the previously recognized particle areas individually. Within this segmentation, two thresholds are defined for the particle-property filter. A high-level and a low-level threshold. All pixels intensities are compared to the maximum pixel intensity for the individual segment. The algorithm counts all pixels with intensities higher than the low-level threshold as one set, and all the pixels with intensity higher than the high-level threshold as another set. For each of the two sets, the area and the diameter are calculated. The diameter and centre of particle is then calculated as the average to the two sets (Fig. 2.2c). The calculated diameter is a measure of the particle size.
- The third filter that was applied is a particle filter. This filter sets a threshold for the maximal low-level area as a percentage of the high-level area. The filter is designed to exclude de-focused particles or structures that are recognized as particles, but do not represent suitable contributions because of their insufficiently clear detection.
- The next step in the post processing is the calculation of the particle velocity  $v_{p_i}$ , done by using a particle tracking algorithm. Before applying the velocity calculation, information about position and diameter are stored in two lists. To identify pairs of particles, a





(a)



(b)



(c)

Figure 2.2: Detail of a captured raw image (a), and the inverted image after the particle-recognition filter (b). The green highlighted areas are recognized particles. The inverted image after the particle-property filter (c). The long (low-level) and short (high-level) axes are drawn in red as well as the diameter ( $\mu\text{m}$ ) in orange.





Figure 2.3: The velocity calculation was performed based on the shift between two consecutive images. The green area represents the particle's initial position, the grey area is the final position.

shift and an interrogation window are defined for each particle in two consecutive images. Based on the cross-correlation between the interrogation window of the images, matching particle pairs can be defined. To avoid a misinterpretation of particle pairs, a maximal shift and a maximal deviation between the diameters are defined. The velocity calculation is based on the separation time between two consecutive images; refer to Figure 2.3 for an illustration of the particles velocity.

- An additional border correction is applied for the computing of the particle detection area. The first segmentation just recognizes particles that are entirely within the defined image area. Particles that are just partially within the field-of-view are not considered. Therefore, the image border corresponding to half of the particle diameter  $d_i$  does not contribute to the image detection area. The field-of-view (FOV) for the volume calculation was cropped for each particle individually based on its diameter:

$$FOV_{x,i} = FOV_x - d_i, \quad (2.1a)$$

$$FOV_{y,i} = FOV_y - d_i \quad (2.1b)$$

- According to the previously described slope of the depth-of-field (DOF)  $m_{DOF}$ , the depth-of-field for each particle could be calculated based on its diameter,

$$DOF_i = m_{DOF} \cdot d_i. \quad (2.2)$$

Together with the density of the snow particles  $\rho_{snow}$ , the particle velocity and the

PR	20	30	40	50	60	70
PP	25 - 75	30 - 70	35 - 65	40 - 60	45 - 55	50 - 50
PF	125	150	175	200	225	250
dFOV <sub>x</sub>	100	43	32	21	11	
dFOV <sub>y</sub>	100	36	27	18	9	

Table 2.1: Parameter thresholds settings for the parametric study in percentages (Particle recognition (PR), Particle property (PP: low-level - high-level), Particle filter (PF), Domain size of the field-of-view horizontally (dFOV<sub>x</sub>), Domain size of the field-of-view vertically (dFOV<sub>y</sub>).

field-of-view, the mass flux for each particle individually is then given by

$$q_i = \rho_{snow} \left( \frac{d_i^3}{FOV_{xi} \cdot FOV_{yi} \cdot DOF_i} \right) v_{pi}. \quad (2.3)$$

The mass flux for each time step is calculated as the sum of the mass flux of each particle within the image,

$$Q(t) = \sum_i q_i. \quad (2.4)$$

The particle tracking algorithm is part of the software package Davis provided by LaVision, GmbH. For this study, the Davis software was used for the particle recognition, property calculations, filtering and velocity calculations. The reference values to start the parametric study were taken from the software's manual LaVision-GmbH [2011]. The calculation of the mass flux including the border correction and the depth-of-field estimation was done with MATLAB software. For further details on the Davis software refer to the mentioned manual provided by LaVision-GmbH [2011].

### 2.2.3 Experiments

In order to correlate particle numbers, size distribution and mass flux measured by both techniques, two different tests were performed. The first test was designed as a calibration study in rather controlled conditions, the second test was a typical drifting snow test with the aim of testing the measurement techniques in more complex and realistic conditions. For both tests, the PTV and SPC techniques were compared for different parameter settings on the PTV image analysis side in order to determine the most suitable processing parameters for the shadowgraphic image processing. Parameters that were addressed for the processing of the PTV images were the thresholds for particle recognition, for the particle property (high-level - low-level), the particle filter and field-of-view. The percentages for the variation of the threshold as used in the parametric study can be found in Table 2.1. The theory to these parameters is explained in the previous Sect. 2.2.2.

The size of the field-of-view was cropped in both directions, horizontally and vertically. Crop-

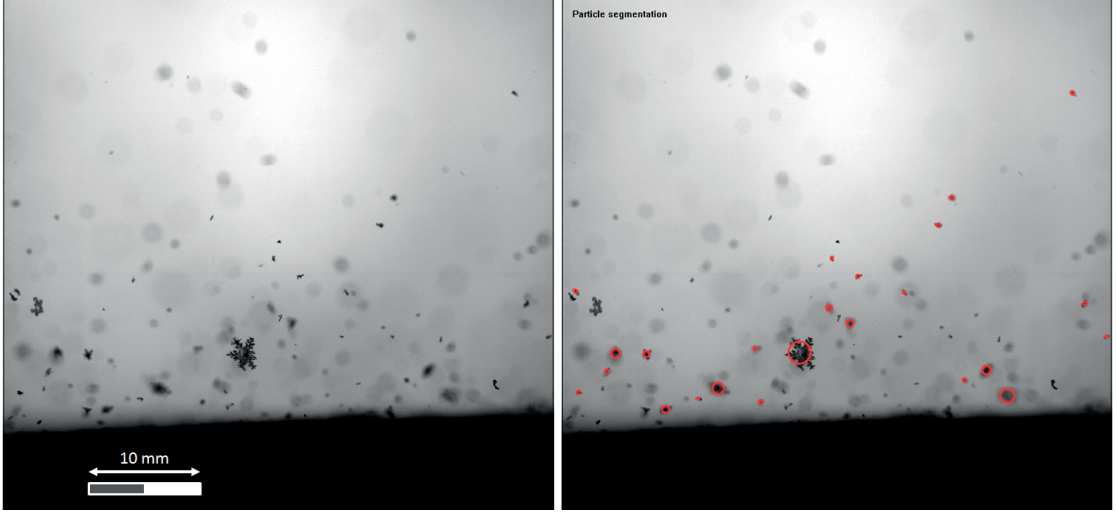


Figure 2.4: On the left, a raw shadowgraphic picture of snow in saltation, and on the right, the same picture after processing with particle-recognition, particle-property and particle-filter methods. The red circles in the right picture indicate the calculated particle diameter.

ping of the field-of-view was introduced to investigate the dependency of the result on the domain size. For the variation of the field-of-view, the values of the other parameters were set according to the previously determined best values.

### Calibration experiment

The first set of experiments was designed such that the SPC is visible in the PTV images and preferably measuring the same particles (Fig. 2.5). Snow particles were artificially scattered using a sieve. The driving force for particle movement was gravity only, resulting in relatively low particle velocities and a wide, homogeneous distribution of particles. The PTV recordings were conducted with an exposure time  $t_{exp}$  of  $0.33 \times 10^{-5}$  s. According to Bagnold [1941], the selection of the exposure time should be based on maximal expected velocity  $U_{max}$  of the minimal expected particle diameter  $d_{min}$ ,

$$t_{exp} = \frac{d_{min}}{U_{max}}. \quad (2.5)$$

In the case of the calibration experiment, the minimal diameter according the SPC bin was  $d_{min} = 0.04$  mm, the maximal velocity was  $U_{max} \approx 1$  m s<sup>-1</sup>. Resulting in a maximal  $t_{exp} = 0.4 \times 10^{-5}$  s. With  $0.33 \times 10^{-5}$  s, we ensured capturing sharp enough images. For each sample, a pair of images was taken, and based on the particle path from the first to the second image of this pair, the particle velocity could be calculated. The frequency to record this pair of images

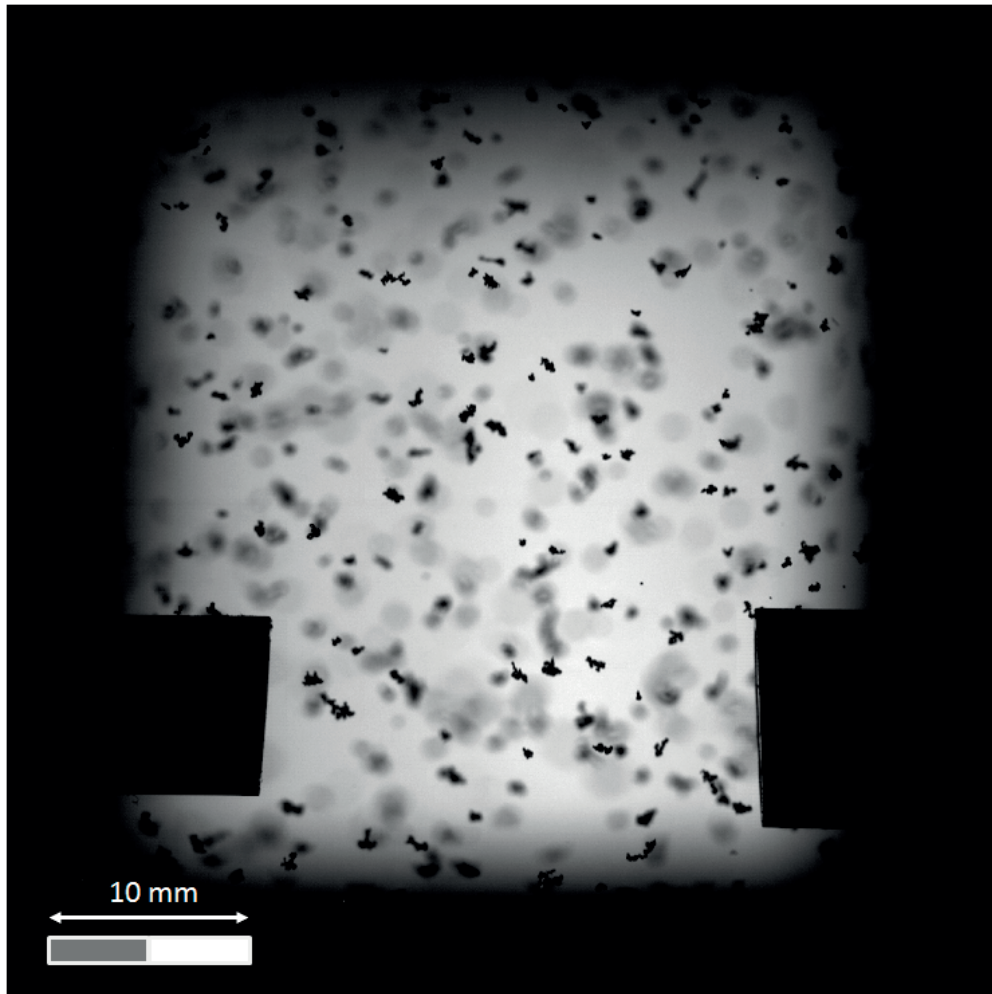


Figure 2.5: Images from the calibration study with artificially scattered snow particles and the SPC visible in the image.

is called the separation time. For the calibration experiment, the separation time was set to 0.001 s (frequency for the separation time 1 kHz). The sampling frequency was set to 50 Hz guaranteeing the detection of all particles falling through the sensor. In total, three different tests were processed (experiments C1 - C3), and during the calibration experiments, the air temperature varied between  $-2.6^{\circ}\text{C}$  and  $-3.4^{\circ}\text{C}$ .

Besides the calibration experiment with snow, an additional experiment with the same set-up and quartz sand particles was performed. The sand particles had a particle-size distribution given by the manufacturer from 0.1 - 0.6 mm in diameter. This test was performed in order to compare the complex-shaped snow particles to more mono-dispersed and round particles.

Table 2.2: Conditions and settings of the drifting experiment

	$U_{free}$ $\text{m s}^{-1}$	$T_{air}$ $^{\circ}\text{C}$	Number of images	Exposure time s	Separation time kHz	Sampling frequency Hz
D1	14	$-1.2 \pm 0.1$	2728	$1.22 \times 10^{-5}$	3.6	10
D2	10.7	$-1.3 \pm 0.1$	2728	$1.22 \times 10^{-5}$	3.6	20
D3	11.8	$-1.3 \pm 0.1$	2728	$1.22 \times 10^{-5}$	3.6	20

### Drifting experiment

The second experiment was a standard drifting test on a natural snow cover with the SPC placed a few millimeters downstream of the PTV system's field-of-view with the middle of the SPC's measurement volume aligned to the middle of the field-of-view. The wind speed was set high enough to allow sufficient saltation, with the wind speed in the freestream region measured with a propeller-type anemometer (MiniAir 20, Schiltknecht Messtechnik AG).

Previous publications report an exponential decrease of the horizontal mass flux with height Sugiura et al. [1998], Nishimura and Nemoto [2005], Guala et al. [2008]. As a result, the most significant portion of the mass is transported near the surface. Hence the field-of-view was focused for the detection of the inner saltation layer, where the peak of the mass flux occurs. Focusing on a small region of the saltation layer allows us to increase the spatial resolution of the acquired images in order to better detect the smallest particles. As with the calibration tests, three drifting tests were conducted (Table 2.2). The separation time between the two images of each pair was set to  $2.78 \times 10^{-4}$  s (3.6 kHz), the image pairs were sampled at 20 Hz, which resulted in an experiment duration of 136.4 s. Previous experience as well as Bagnold's relation for the exposure time (Eq. 2.5) suggested using an exposure time short enough in order to freeze the particle motions and thus avoid blurring. The calibration experiment proved that the smallest recognizable particles with the current set-up were  $d_{min} \approx 0.1$  mm. With the freestream velocity set at  $U_{free} < 11.8 \text{ m s}^{-1}$ ,  $t_{exp}$  should have been set to  $8.475 \times 10^{-6}$  s (118 kHz) (particles near the surface are generally slower), resulting in underexposed images. Therefore, for all the three experiments, the exposure time was set to  $1.22 \times 10^{-5}$  s (82 kHz) in order to have a good compromise between light intensity, contrast and exposure time.

One shortcoming of both methods is the assumption of spherical particles for the calculation of the mass flux. Especially for larger particles, when particles are shaped as dendrite (refer to Fig. 2.4), the error in the absolute values of the mass flux may be considerable. For the current study, this assumption should not weaken the correlation, since it is valid for both techniques.

## 2.3 Results

### 2.3.1 Calibration experiment

We first present a representative sand experiment (refer to Sect. 2.2.3), which we conducted in preparation for the more complex snow experiments. Mass calculations based on the

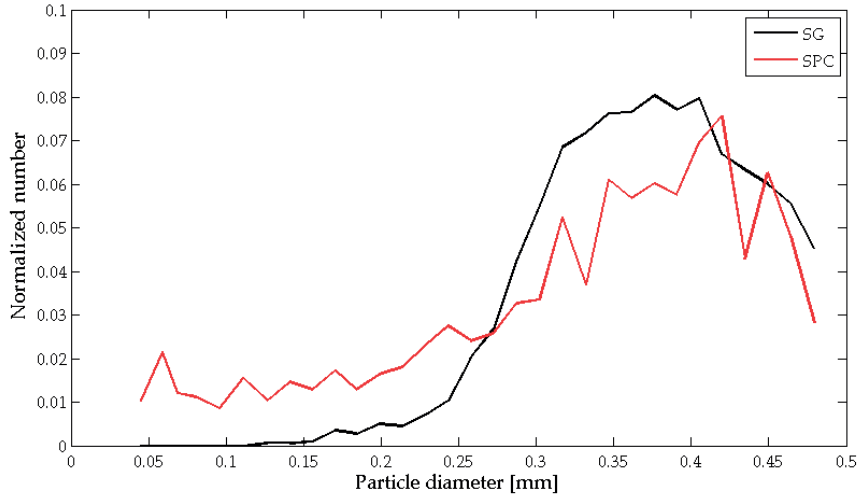


Figure 2.6: Particle-size distribution of the calibration experiment with sand particles. The vertical axis shows the normalized number of particles.

assumption of spherical grains are less uncertain than for the highly irregular snow-particle shapes. Figure 2.6 shows the particle-size distribution of this sand experiment, and confirming that both instruments interpret the particle size similarly. The particle numbers are normalized by dividing the numbers of the individual classes by the total number of particles detected by the corresponding technique. Since the sand could not be sieved homogeneously over the whole field-of-view, the requirements for a calculation of the mass flux with PTV image analysis were not fulfilled and therefore no mass-flux calculation is presented here.

### Mass flux and particle-size distribution

The two time series of the mass flux recorded by the SPC and the PTV method were correlated using MATLAB and the Spearman-correlation function. The time series from the shadow-graphic PTV were down-sampled to match the sampling frequency of the SPC. Since the range of the particle diameter on the SPC side is bounded between 0.04 mm to 0.5 mm (larger particles are assigned to the 0.5-mm-diameter class), particles on the PTV side with a diameter  $> 0.5$  mm are also counted as 0.5 mm. This restriction on the PTV side was intended to reduce potential errors and disagreement between the two methods. Figure 2.7a shows the mass-flux signal for experiment C1. The average particle speed recorded by the PTV system for the calibration experiments was between  $0.96 \text{ m s}^{-1}$  and  $1.13 \text{ m s}^{-1}$  (experiment C1  $1.11 \text{ m s}^{-1}$ , C2  $0.96 \text{ m s}^{-1}$  and C3  $1.13 \text{ m s}^{-1}$ ). Already here, a satisfying agreement between the signals of the mass flux for SPC and PTV is obtainable, except a slight discrepancy for the events with high mass flux. Figure 2.7b shows the normalized particle-size distribution for the same experiment.

It can be noted that for this experiment, the PTV records many more particles compared to the SPC, and can be explained by the larger measurement volume of the PTV images. Furthermore,

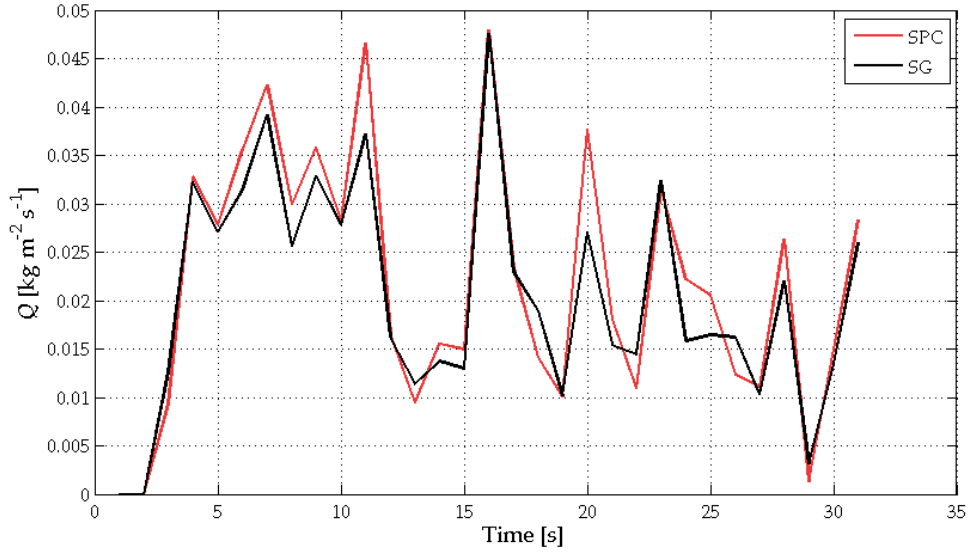


it is noticeable in the particle-size distribution in Figure 2.7b that the PTV method fails to detect particles in the range 0.04-0.15 mm.

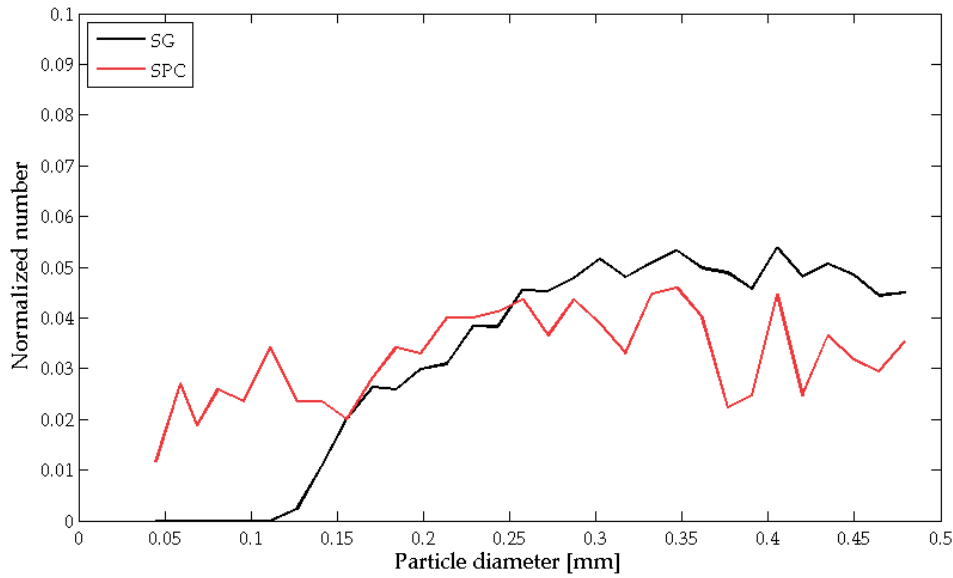
### PTV parameter sensitivity

Figure 2.8 shows the results of the parametric study of the PTV post-processing, with the ratio of the PTV and SPC mass flux and their correlation coefficient. On the horizontal axis of each panel, the thresholds in percentage for the three processing parameters PR, PP and PF (refer to Sect. 2.2.2) are listed. Overall the correlation as well as the ratio of the mass flux were very satisfying for all cases considered. As previously described, the filter for the particle recognition influences how many particles are recognized. For low particle-recognition thresholds, the ratio of the total mass flux increases (Fig. 2.8a). This can be explained by considering that with a low threshold for the particle recognition, more pixels in the image are interpreted as particles resulting in an increase of the mass flux. This effect seems to be linear, since it does not affect the correlation between the two signals significantly. For the particle-recognition filter, the correlation was always between 0.91 and 0.96, the ratio of the mass flux between 1.15 and 0.85. The highest correlation overall was found in the range of 40% – 50%. The ratio of the mass flux for a particle-recognition threshold of 50% is slightly closer to one than that for 40%. Except for the results for C3, the results for the tests on particle recognition are very similar to each other. Also the results for the three tests with different particle-property thresholds are very similar to each other, for both correlation and ratio of the mass flux. Small particle-property thresholds, resulting in a large difference between low-level and high-level intensity, reduce the ratio of the mass flux (Fig. 2.8c). This behaviour can be explained by the fact that a large difference between low-level and high-level intensity leads to an unfavourable ratio for the consecutive particle-filter threshold. Hence many particles are removed by the particle filter. Similar to the particle-recognition threshold, this effect seems to be linear as well and therefore is not weakening the correlation strongly. Compared to the particle-recognition threshold, the ratio of the mass flux shows a clearer optimum for all experiments, which is at a particle-property threshold for the low-level and high-level pixel intensity of 40% - 60%. Also the variation of the particle-filter threshold demonstrated good correlation, as well as similar effects on the mass flux ratio. As described previously, for low particle-filter thresholds, many particles do not satisfy the threshold and are therefore excluded from processing. This only affects the ratio of the mass flux and not the correlation between the two time series. The best correlation and mass flux ratio for the particle-filter threshold shows to be at 175% (Mean correlation coefficient 0.934, ratio of the mass flux 0.94).

In the parametric study discussed above, the ratio of the mass flux and the correlation coefficient resulted from varying only one parameter at a time, while the other parameters were kept constant. For the sake of completeness a parametric study was also conducted by varying two parameters at a time, validating that the results discussed for the individual parameters are not biased by the choice of the other parameters. The ratio of the mass flux and correlation coefficients for the variations of two different parameters at a time are shown in Figure 2.9.



(a)



(b)

Figure 2.7: Results of experiment C1 - mass flux signal presented as 1-s averages (a), particle-size distribution with the vertical axis showing the normalized number of particles (b). Correlation  $r = 0.954$ , total mass flux ratio  $Q_{PTV}/Q_{SPC} = 0.937$ , total number of particles PTV = 13265, total number of particles SPC = 1208. PTV settings were chosen according to the best case settings for the calibration experiment (PR = 50%, PP = 40% - 60%, PF = 175%, dFOV<sub>x</sub> = dFOV<sub>y</sub> = 100%).



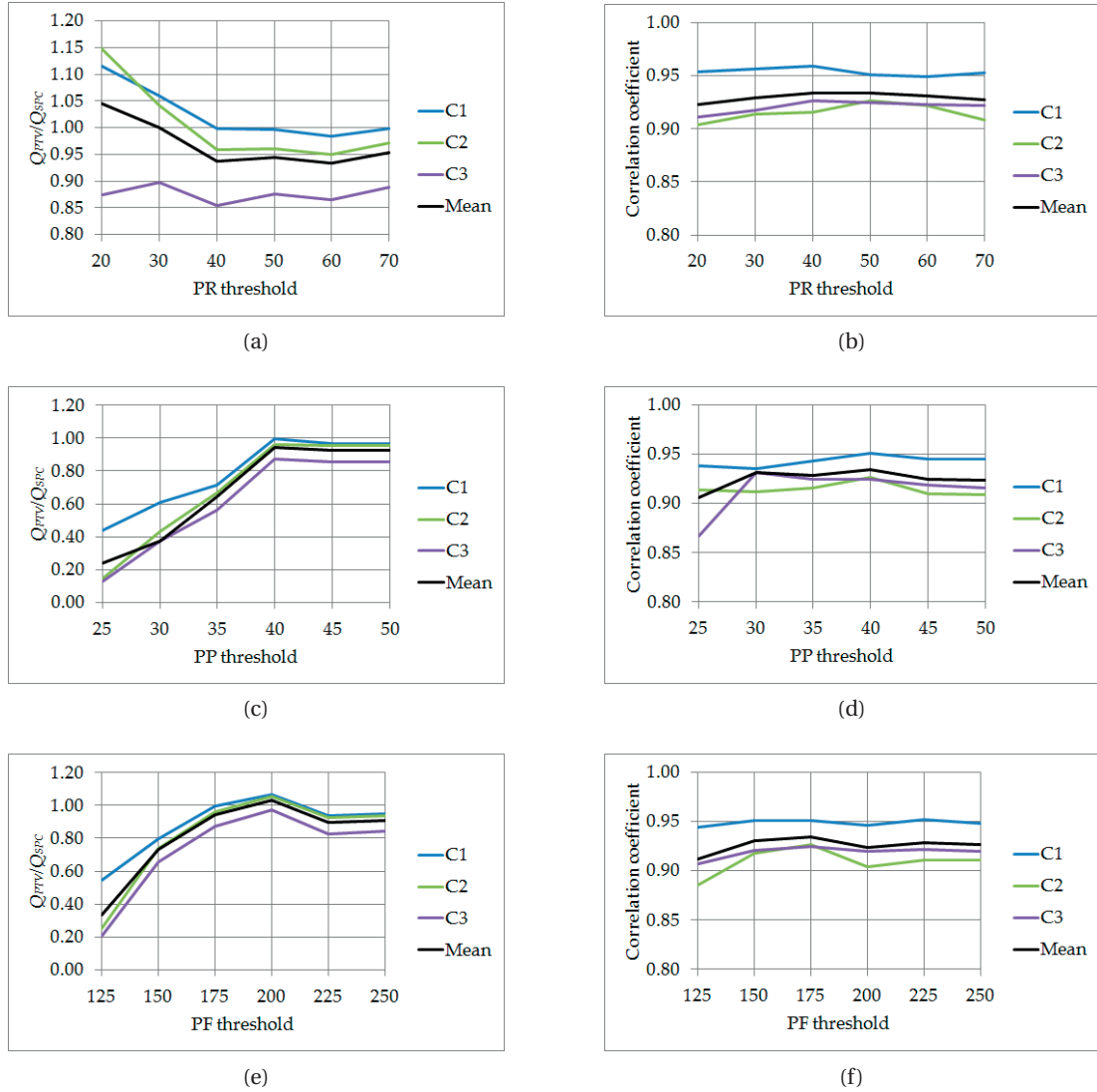


Figure 2.8: Results of the parametric study for the calibration experiment. On the left side, the results of the ratio of the PTV and the SPC mass flux ( $Q_{PTV}/Q_{SPC}$ ) is shown for the different thresholds: PR (a) , PP (c) , PF (e). On the right, the results of the correlation coefficient for the mass-flux time series are presented for the different thresholds: PR (b) , PP (d) , PF (f).

## Chapter 2. Quantifying Particle Numbers and Mass Flux in Drifting Snow

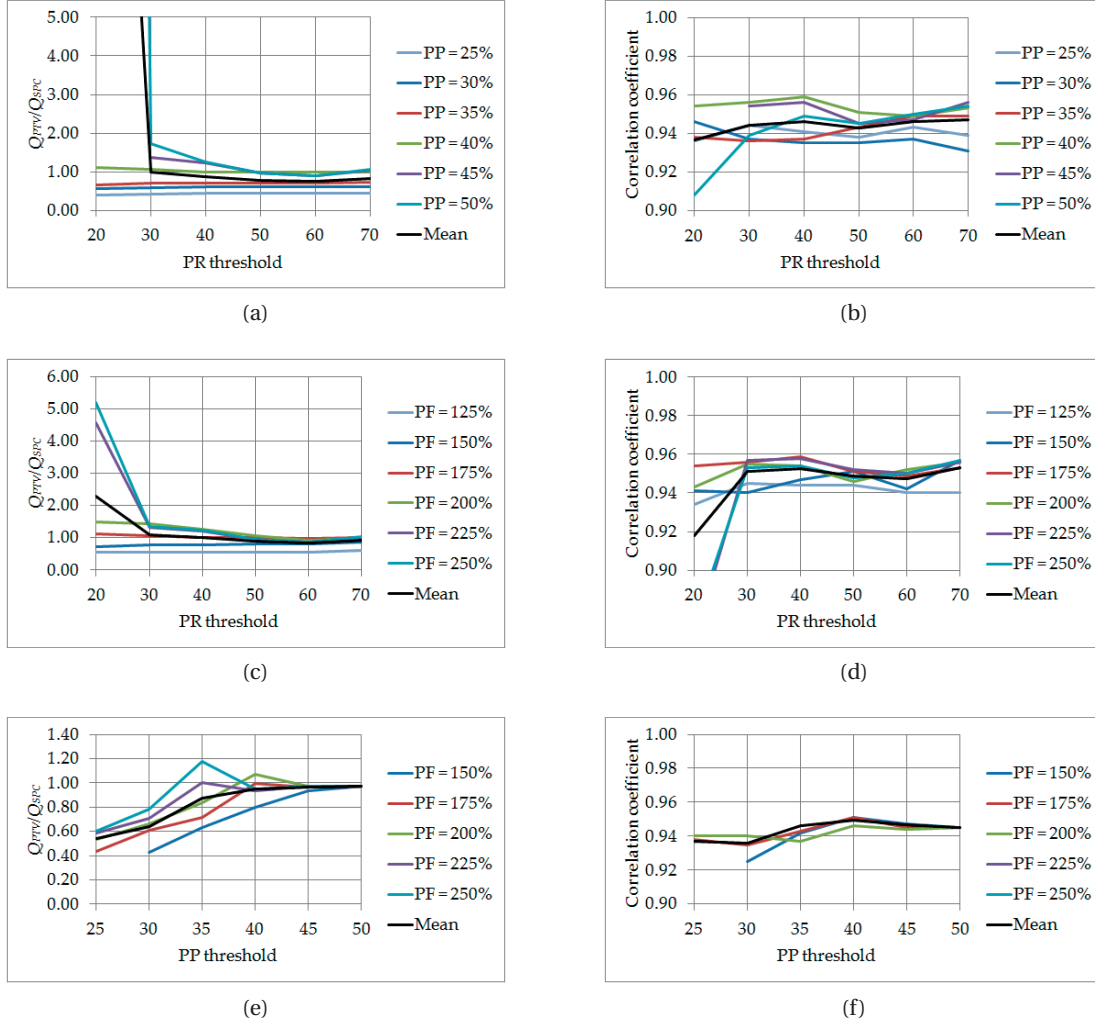


Figure 2.9: Results of the parametric study for the calibration experiment. The horizontal axis represents the first parameter, the different colored lines represent the choice of the second parameter. On the left side, the mass flux ratio ( $Q_{PTV}/Q_{SPC}$ ) is shown for the combination of two different thresholds: PR/PP (a) , PR/PF (c), PP/PF (e). On the right, the correlation coefficient for the mass-flux time series are presented as a function of different thresholds: PR/PP (b), PR/PF (d), PP/PF (f).

The two parameter study was conducted based on the data of C1. The best fit parameters from the results presented previously with the variation of one single parameter at a time could be confirmed. In case of the particle-recognition threshold, the ratio of the mass flux and the correlation coefficient are optimized for a particle recognition around 50% and ratio and correlation are minimally affected by the choice of the particle-property or particle-filter thresholds. Furthermore, the choice of the particle-property threshold was confirmed to be optimized at a low-level of 40% and a high-level of 60% even when varying the particle-filter threshold at the same time.

Figure 2.10 shows the results for the ratio of the mass flux and correlation coefficients due to the variation of the size of the field-of-view. For the evaluation of the dependency of the domain size, the height/width of the field-of-view was normalized with the path length of a particle within a time step in streamwise direction or with the height/width of the SPC in the direction perpendicular to the streamwise direction. The path of a particle  $p$  is calculated as the mean particle velocity  $u_{PTV}$  and the sampling frequency  $f_s$ ,

$$p = \frac{u_{PTV}}{f_s}. \quad (2.6)$$

Both, the ratio of the mass flux and the correlation reach a plateau as soon as the dimension of the field-of-view in the streamwise direction is approximately as long as the path of a particle between two consecutive images (i.e. the normalized length is equal to 1).

The analysis of the drifting snow tests followed the same scheme as seen for the calibration tests discussed above. In comparison to the calibration experiments, the length of the field-of-view was now varied along the streamwise direction and the resulting mass flux proved to be more intermittent than in the previous experiment. Figure 2.11a shows the mass flux time series for experiment D1, Figure 2.11b shows the diameter distribution for the same experiment. In contrast to the calibration test, where the SPC detected more than 10 times less particles than the PTV, in the drifting experiments, the numbers of detected particles by the SPC were in a similar range. This large difference is mainly explained by the fact that in the case of the calibration experiment, where the particles sizes are more uniform, the PTV measurement volume is much larger than the SPC's volume. In the case of the drifting experiment, due to the difference in detected particle sizes, the size of the measurement volume is compensated by the SPC's capability to record smaller particles. In the experiments D1 and D3, the SPC recorded even more particles than the PTV system. Also the average particle velocity in the field-of-view recorded by the PTV were much higher (experiment D1  $6.9 \text{ m s}^{-1}$ , D2  $5.1 \text{ m s}^{-1}$  and D3  $6.0 \text{ m s}^{-1}$ ). A more detailed discussion of the particles numbers and diameter distribution will be presented in the subsequent section.

The results for the correlation of the experiments with drifting snow are shown in Figure 2.12 b,d,f. Compared to the calibration experiments, the correlation between the two signals is slightly weaker. The results for optimal thresholds for particle recognition (50%), particle property (45% - 55%) and particle filter (200%) are close to the results from the calibration study. While the best choice of the particle-recognition threshold is identical, the particle-

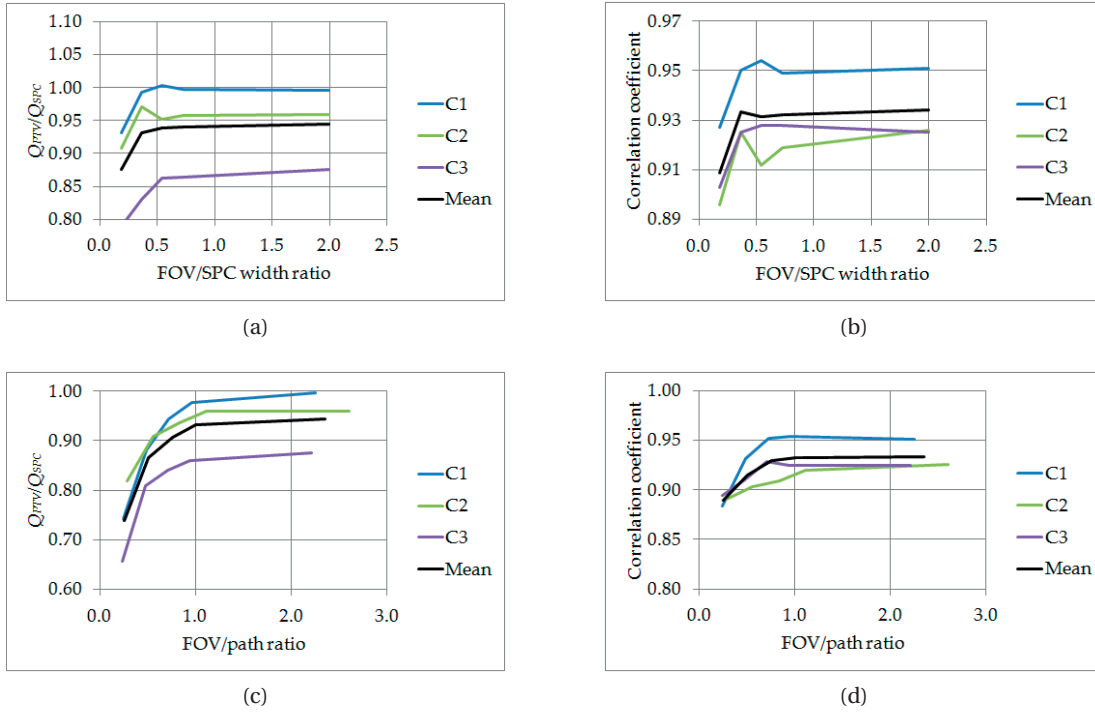
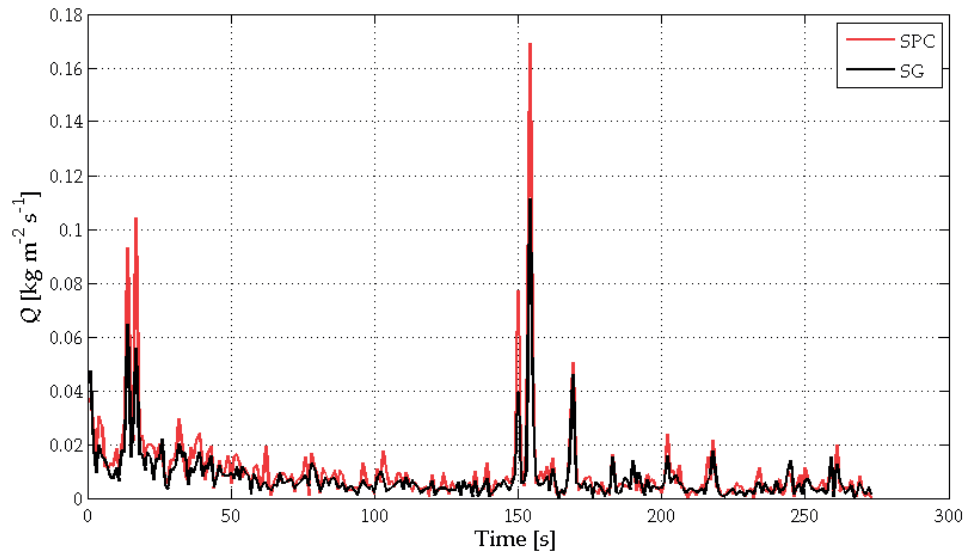
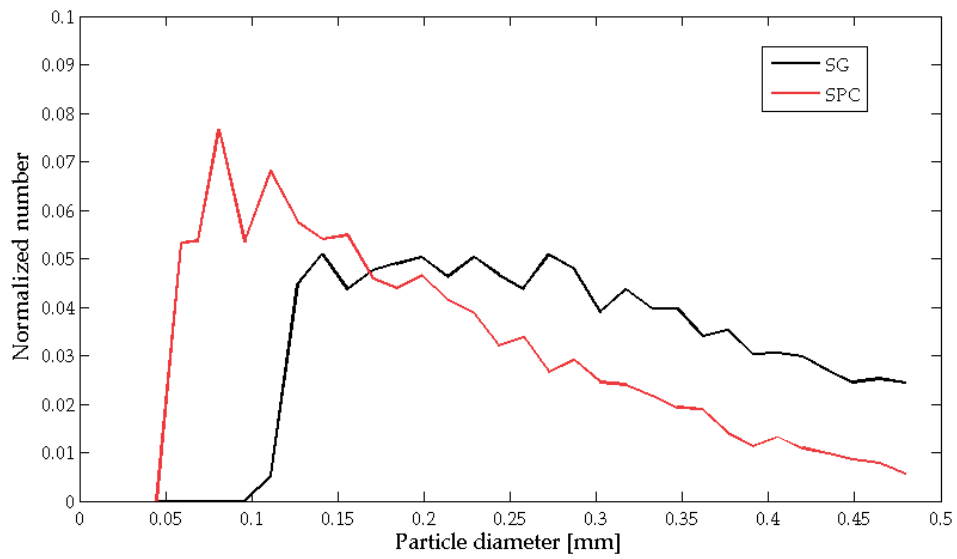


Figure 2.10: Results of the parametric study for the calibration experiment. On the left side, the mass flux ratio ( $Q_{PTV}/Q_{SPC}$ , FOV/SPC width ratio (a), FOV/path ratio (c)) is shown for the different dimensions of the field-of-view. On the right, the correlation coefficient for the mass-flux time series are presented (FOV/SPC width ratio (b), FOV/path ratio (d)).



(a)



(b)

Figure 2.11: Results of experiment D1 - mass flux signal presented as 1-s averages (a), particle-size distribution with the vertical axis showing the normalized number of particles (b).  $r = 0.83$ ,  $Q_{PTV}/Q_{SPC} = 1.016$ , Total number of particles PTV = 12953, total number of particles SPC = 15161, PTV settings: PR = 50%, PP = 45% - 55%, PF = 200%, dFOVx = dFOVy = 100%.

property and particle-filter thresholds are slightly higher compared to the calibration study. The parametric study for the drifting experiments reveal that the results from the particle-recognition threshold is the most difficult to judge as the range of optimal values is rather large. The results from the correlation and the ratio of the mass flux suggest 50% as the optimal choice, even though, a threshold set at 40% would not produce any significant difference in the results as well.

The results for the cropped image of the drifting snow experiment again show the sensitivity of the results to the field-of-view dimensions (refer to Fig. 2.13). For the streamwise direction, the correlation curve has a logarithmic shape. Compared to the calibration test, due to the faster velocity of the snow particles, as well as the trade off between sampling frequency and the length of the time series, the ratio between field-of-view and path length is smaller. In order to reach a similar ratio like in the calibration experiment, the sampling frequency should have been set 10 times larger. Due to the limited camera memory, this would have lead to a time series duration of less then 30 seconds. Considering the relevant time scales occurring in drifting snow events such an acquisition frequency would have limited the convergence of the statistics. As a consequence, the sampling frequency was reduced. Despite this reduction of the sampling frequency, the ratio of the mass flux recorded by the PTV and the SPC equals 1 at a ratio of the field-of-view to the particles path of approximately 0.05. The correlation at that point is already at more than 0.75 and tends to increase further with increasing horizontal length of the field-of-view, although the PTV is overestimating the mass flux compared to the SPC. Comparing this behavior to the analogous plot from the calibration experiment, it can be assumed that this increase continues up to a value of 0.5 on the x-axis. In the case of the vertical field-of-view, best correlation and ratio of the mass flux is obtained when the field-of-view is 10 times larger then the height of the SPC (i.e. approximately 20 mm). For the drifting experiment, no additional two parameter study was conducted.

### 2.3.2 Number of particles

Although the mass flux signals from the SPC and PTV show a strong correlation, the particle-size distribution are significantly different between the two measurement techniques. Since the calculation of the mass flux for both techniques is based on the number of particles detected and their corresponding diameter estimation, we also correlated the timeseries of the number of particles from the two techniques. Therefore the particle number fluxes resulting from the optimal choice of the three different particle thresholds (particle recognition, particle property, particle filter) were analyzed. Figure 2.14a shows the number flux presented as 1-s average for the calibration experiment, Figure 2.14b shows the number flux of the drifting snow experiment. The correlation for the particle numbers in the calibration experiment were slightly larger for all three experiments ( $r = 0.931 - 0.965$ ) compared to the correlation of the mass flux. Although for the calibration experiment, more than ten times less particles were recorded with the SPC than with the PTV (refer to Fig. 2.14a,  $np_{PTV}/np_{SPC} = 10.981$ ), the correlation was very high.

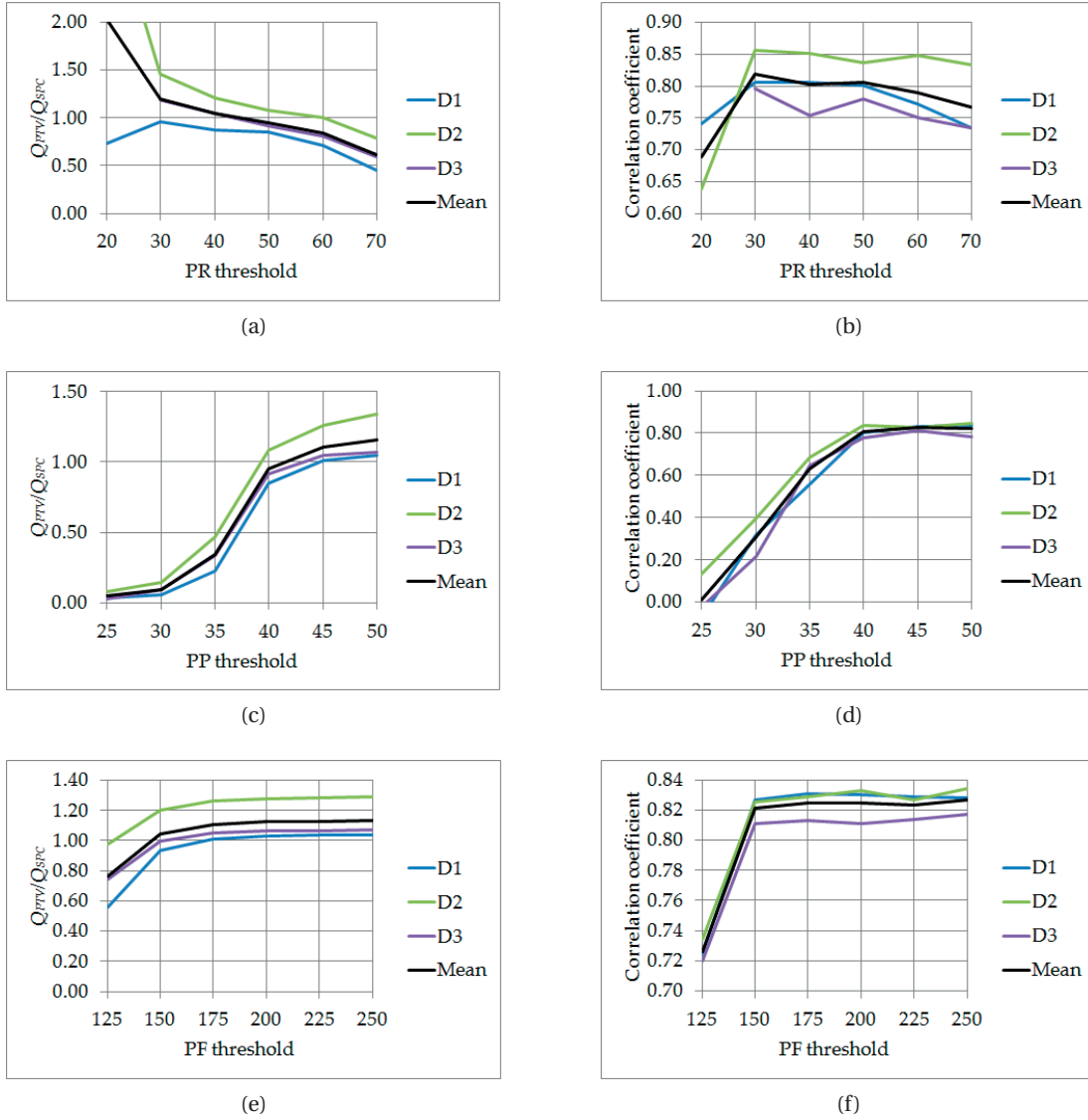


Figure 2.12: Results of the parametric study for the drift experiment. On the left side, the mass flux ratio  $Q_{PTV}/Q_{SPC}$  is shown for the different thresholds: PR (a) , PP (c) , PF (e). On the right, the correlation coefficient for the mass flux time series are presented: PR (b) , PP (d) , PF (f).

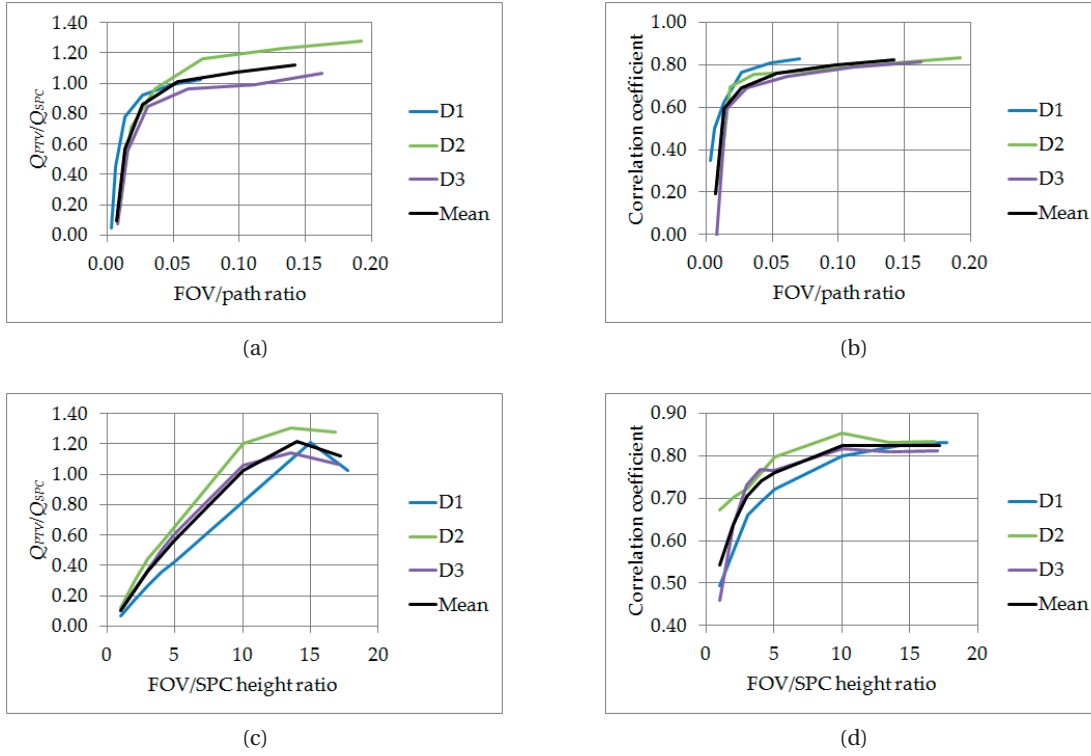


Figure 2.13: Results of the parametric study for the drift experiment. On the left side, the mass flux ratio  $Q_{PTV}/Q_{SPC}$  is shown for the different dimensions of the field-of-view (FOV/path ratio (a), FOV/SPC height ratio (c))). On the right, the correlation coefficient for the mass flux time series are presented FOV/path ratio (b), FOV/SPC height ratio (d)).



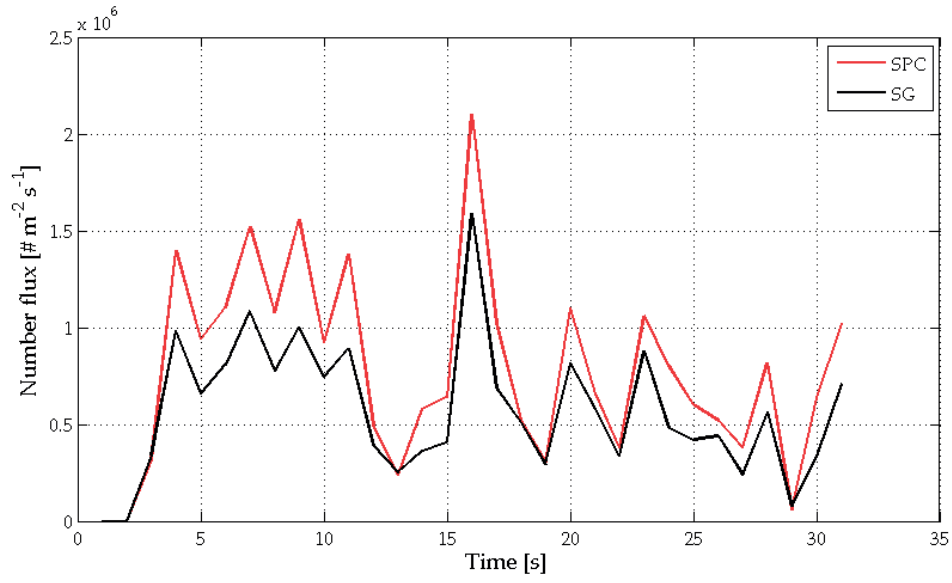
Similar results as for the calibration experiments were found for the experiments with drifting snow. The correlation for the numbers fluxes was stronger ( $r = 0.838 - 0.91$ ) compared to the correlation of the mass flux. Other than for the calibration experiment, the ratio of numbers of particles between PTV and SPC was much closer to one (refer to Fig. 2.14b,  $np_{PTV}/np_{SPC} = 0.854$ ).

## 2.4 Discussion

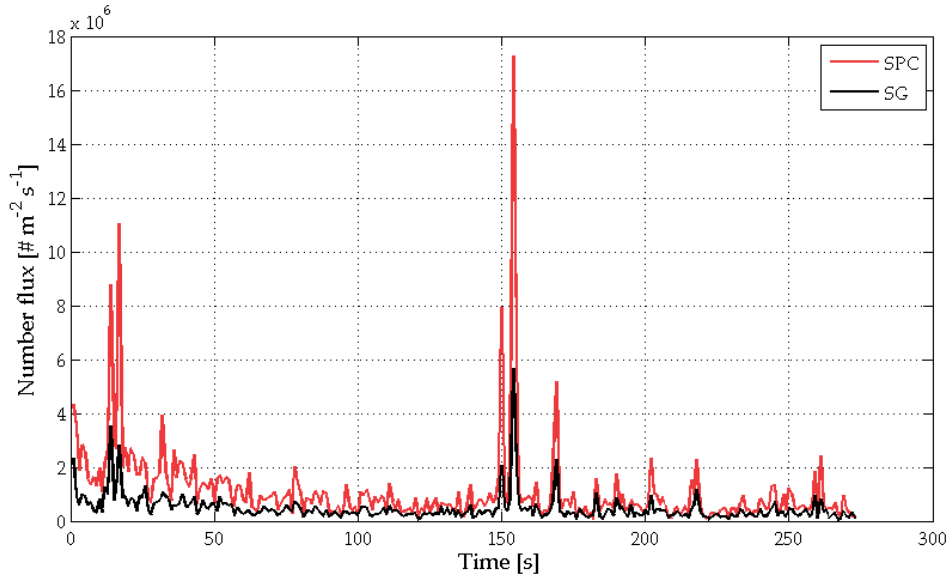
### 2.4.1 Particle recognition, particle property and particle filter

This study reveals good agreement for in terms of correlation and mass flux ratio for the two techniques for both, the calibration (Fig. 2.8) and the drifting snow experiments (Fig. 2.12). Among the different post-processing parameters that were tested, the particle-recognition threshold shows the largest impact on the results. The smaller this particular threshold is chosen, the more spots in the image are recognized as particles. Consequentially, a very small particle-recognition threshold leads to overestimation of the mass flux. As soon as the threshold is large enough, the correlation and the mass flux ratio are fairly constant. These results were confirmed by the drifting snow experiments as well. A much clearer picture is observed in the selection of the particle-property filter. As previously described, this filter introduces a low-level and a high-level threshold for the estimation of the particle's diameter. The closer together the high and the low level thresholds are, the smaller is the ratio between high-level and low-level areas. This affects the estimation of the diameter, and finally the assigned mass of the particle. Being the depth of field of a particle proportional to its diameter, this threshold also affects the size of the depth-of-field. More directly, the size of the depth-of-field together due to the amount of accepted blurring is further controlled with the third parameter particle filter.

In the previous section, the optimal threshold for the particle recognition was found to be at 50%, for both, the calibration as well as the drift experiment. This closely matches with the settings used by Gromke et al. [2014]. For the low-level and high-level particle-property thresholds, we found the optimal thresholds at 40% - 60% (calibration) and 45% - 55% (drift) respectively (Gromke et al. [2014] used 40% - 60%). Similarly, the results for the particle-filter threshold were slightly higher in the snow drifting experiment (200%) compared to the calibration experiment (175%). The effect of having a higher particle-property and particle-filter threshold for the drifting experiments when compared to the calibration study is not very significant. For both thresholds the ratio of the mass flux as well as the correlation coefficient reach a plateau, where the results are minimally affected by the choice of these thresholds (Fig. 2.12 e - f). An explanation for such behaviour is that for larger thresholds, the depth-of-field is deeper. Setting the particle-property threshold at 45% - 55%, the median depth-of-field results to be 27.82 mm, whereas for 40% - 60%, the median depth-of-field is 18.51 mm in the drift experiment. The corresponding dimension of the SPC is 25 mm. Having such a large low-level particle-property threshold, the particle-filter threshold is only slightly influencing the correlation and the ratio of the mass flux. Only a very small particle filter does reduce the



(a)



(b)

Figure 2.14: Number-flux time series signal presented as a 1-s average of the calibration experiment C1 (a) ( $r = 0.965$ ), and for the drifting experiment D1 (b) ( $r = 0.838$ ).

depth-of-field and excludes many particles from fulfilling the criterion.

### 2.4.2 Sensitivity of the field-of-view

Analyzing the influence of the dimensions of the field-of-view, suggests that a minimum spatial extent of the field-of-view exists, below which the results are affected due to excessive undersampling. In the case of the calibration experiment, in which the speed of the particles was relatively slow, a large field-of-view did not reduce the correlation or the ratio between the PTV and SPC signals. This behaviour was observed for both, the streamwise direction as well as the direction perpendicular to the flow (Fig. 2.10). For the drifting snow experiment, where the average particle speeds were between  $5.1 \text{ m s}^{-1}$  and  $6.9 \text{ m s}^{-1}$ , the ratio between field-of-view in streamwise direction and the path length particles travel between two consecutive images became much smaller. To obtain the same ratio between particle trajectory and field-of-view, either the field-of-view in the streamwise direction or the sampling frequency have to be increased. In our set-up, both of them are limited, the field-of-view due to the finite camera resolution and the sampling frequency due to the limited camera memory. In order to have a long enough experiment, the sampling frequency was chosen rather low. Although the ratio of field-of-view and particle path as small, the results are similar to what was found in the calibration tests. Figure 2.13b, FOV/path ratio - Correlation coefficient, reveals a logarithmic dependence between the dimension of the field-of-view and the correlation between the PTV and SPC mass flux. While the correlation is improving with increasing length of the streamwise field-of-view, the results of the mass flux ratio suggest that a very large field-of-view tends to slightly overestimate the mass flux of the PTV (Fig. 2.13a) which was not the case in the calibration experiment. This might be an artifact of the too low sampling frequency. On the other hand, the height field-of-view should be at least chosen to be 10 times larger than the height of the SPC, which leads to a vertical field-of-view of at least about 20 mm. Similarly, an overestimation occurs as an effect of increasing the vertical dimension of the field-of-view, even though the correlation remains constant. The size of the field-of-view, together with the sampling frequency, controls the number of particles that can be detected.

### 2.4.3 Mass flux, particle diameter and particle numbers

The two signals from the two devices in Figure 2.7a (calibration experiment C1) are very well correlated. Differences can be due to a bias in the particle size distribution between the two (Fig. 2.7b). The SPC, although acquiring at high frequency (40 kHz), detects significantly less particles than the PTV due to the much smaller control volume (Fig. 2.5) of the SPC. In the calibration experiment, where the snow particles are artificially sieved such that they move through the SPC's and the PTV's field-of-view by gravity only, the particles are homogeneously distributed. Due to the larger control volume of the PTV (field-of-view  $50 \text{ mm} \times 50 \text{ mm} \times \text{approx. } 30 \text{ mm}$  (maximal depth-of-field)) than the SPC ( $25 \text{ mm} \times 2 \text{ mm} \times 0.5 \text{ mm}$ ), many more particle are detected with the PTV method. A second reason can be found in the particle-size distribution. The graphs show that the SPC detects more smaller particles compared to the

PTV method. As the particle-size distribution of the more mono-dispersed sand particles (Fig. 2.6) shows similar results for SPC and PTV, the lack of resolution at the smallest bin sizes might result in a minor discrepancy between the mass-flux signals determined with the two instruments. Being only the smallest particle diameters at the origin of this bias the implications for the mass-flux are little. This is supported by the result of the correlation of the particle-number flux (Fig. 2.14a). By not taking into account the particles diameter, the correlation between SPC and PTV method was shown to be stronger.

Looking at the results of the drifting experiments, we find a more distinguished difference in the particle-size distribution (Fig. 2.11b) compared to the results of the calibration experiment. We observe that in the drifting experiment, the particle spectrum as detected by the SPC is shifted towards smaller particles. The maximum of the particle diameters is found close to 0.1 mm for the SPC, while the maximum for the PTV is larger. As a consequence, in all the drifting experiments, the SPC also records many more small particles compared to the PTV method. In case of the drifting experiments additional causes might affect the results of the particle detection from the two instruments.

The profile of the mass flux in the boundary layer is reducing with increasing height above the snow surface, and a peak is observed near the surface. The profile above the peak is reported to be exponential Sugiura et al. [1998], Nishimura and Nemoto [2005], Guala et al. [2008]. Therefore, placing the SPC very close above the surface, where the gradient is high, might introduce a bias in the comparison of the signals of the two instruments. Another difference in the case of the drifting experiment is the previously discussed ratio between the streamwise length of the field-of-view and particle path that is smaller than one. This indicates an undersampling of the PTV method which will not capture all particles passing by the field-of-view during the experiment. Considering the high correlation of the particle numbers and the mass flux ratio between SPC and PTV, the chosen sampling frequency is still sufficiently high to capture the time-evolution of drifting particles. A reason causing the differences in the particle-size distribution between calibration and drifting experiments is that it can be assumed that drifting particles show a rapid fragmentation after the initiation of the saltation. The impact of such a behaviour was not investigated within this study.

Therefore, and because the PTV system fails detecting the smallest particles due to its bounded resolution, the differences in the particle-size distribution and the number of detected particles can be explained. Nevertheless, the effect on the mass flux calculation is smaller since most of the mass is carried by the larger particles. One additional reason that may influences the correlation between the two signals is the SPC's ability of recognizing very small particles. Guala et al. [2008] described that for the very small bins, also the SPC has more difficulties to resolve them compared to particles of the larger bins. Nevertheless this potential effect is hard to estimate.

### 2.4.4 Diameter interpretation and spherical assumption

A further assumption that needs clarification concerns the interpretation of the diameters by both systems. The SPC detects particles in a diameter range between 0.04 and 0.5 mm.

Larger particles are assigned to the 0.5 mm diameter class. For the comparison of the two instruments, the PTV was restricted to the same diameter range and classification. This bounded range may result in an underestimation of the mass flux. As mentioned earlier, both instruments assume the particles to be spherical. Our common experience, further confirmed by Figure 2.4, suggests that snow flakes that are not drifted and fragmented, generally are not spherical. Particularly larger snow particles are not well represented by a sphere. Sphericity is also assumed by the SPC. Therefore we assume that the diameter restriction will not lead to a severe underestimation of the mass flux in this study. Furthermore being the two techniques deployed for the study of drifting snow, which implies fragmentation of the snow crystals towards smaller, more spherical geometries, this assumption does not lead to significant errors in the mass flux estimation.

## 2.5 Conclusions

Wind-tunnel experiments in an ad-hoc calibration and typical drifting snow set-up revealed that the mass-flux signals obtained from the two systems are very well correlated. This study clarified the impact of the post-processing parameters such as particle-recognition, particle-property and the particle-filter thresholds on the PTV results. The study also demonstrates the need of a proper calibration of the PTV system with an established measurement technique such as the SPC to be able to correctly measure the drifting snow in a wind tunnel. Figures 2.8, 2.9 and 2.12 demonstrate that for all tests in both, calibration and drifting experiments, the mass-flux ratio and correlation converge. These results are obtained from tests conducted under different conditions, therefore the validity of the post-processing parameters extends to any drifting snow test in a wind tunnel. The procedure presented in this study can be applied to any other wind tunnel set-up. The impact of parameters such as sensor size, focal length or aperture was beyond the scope of this study. Based on the given equipment and conditions, these parameters were either given or set to fixed values which represented optimal conditions.

For the particle diameter distribution, Gromke et al. [2014] mention that diameters detected with a shadowgraphic PTV are generally larger than those reported in the literature from SPC measurements. This reflects the camera's spatial resolution, and confirms our findings that the SPC is more sensitive to smaller particles which may be the result of the fragmentation during drifting. Nevertheless, considering the 1-s averaged signals, the correlation is very strong for optimal settings and thresholds in the acquisition and post-processing (calibration:  $r \geq 0.93$ , drifting:  $r \geq 0.81$ ). Differences in particle numbers and diameter distribution originate from different sampling rates, different control volume sizes, the bounded resolution of the PTV camera compared to the SPC. Uncertainty however remains on differences in the interpretation by the two systems of the diameter of the same snow particle. The results from the test with sand particles, which shows good agreement between SPC and PTV diameter interpretation, suggests that this difference is not large. Due to the fact that very small particles contribute little to the mass flux, the shift in the particle-size distribution only weakly influences the signal of the mass flux. For the present study, the camera's spatial resolution was

## Chapter 2. Quantifying Particle Numbers and Mass Flux in Drifting Snow

---

approximately  $47.7\ \mu\text{m}$  per pixel, which corresponds approximately to the smallest particle bin size of the SPC. We expect that with a higher resolution, also smaller particles can be detected.

Our results suggest that the PTV technique can be a valid alternative to the more common SPC at least in a laboratory environment, and where both the vertical and streamwise components of the mass-flux are needed, as well as higher sampling frequency. The applicability of the set-up to field studies poses several technical issues and needs to be demonstrated. SPC limits are known, PTV's limits depend on the camera and a general conclusion on this is too restrictive.

### Acknowledgements

The authors wish to express their acknowledgment to the Swiss National Science Foundation (SNF) for funding this research (R grant number 200021\_147184) as well as to Christof Gromke and the SNF (R'Equip grant number 206021\_133786) for installing the PTV equipment. We further thank Prof. Kouichi Nishimura for his support in operating the SPC, Matthias Jaggi for his contribution concerning electronics issues, the SLF workshop team that helped to prepare all the hardware at the wind tunnel as well as the reviewers for their valuable and constructive input.

## **3 Space - time dynamics of erosion/deposition versus horizontal mass flux of snow**

### **3.1 Introduction**

Wind is the main contributor to the erosion of erodible surfaces such as sand or snow. This mechanism of erosion is called aeolian transport. In their work Kok et al. [2012] gave an overview of the three modes, creep, saltation and suspension of aeolian transport. Creep is the rolling and sliding of large particles along the surface, without becoming fully airborne [Bagnold, 1937]. Saltation is the movement of particles along ballistic trajectories following entrainment by the fluid drag or ejection by impacting particles [Bagnold, 1941]. Particles in the saltation mode are often referred to as drifting particles. Suspension is the process of particles that follow the turbulent motion of eddies and may remain a long time airborne. Suspension is often characterized by the time that the particle are in the air and by the size of the particles, which is generally very small [Gillette and Walker, 1977, Zender et al., 2003, Miller et al., 2006]. Aeolian transport starts whenever the force induced by the wind is above a threshold to entrain particles from their bed. The magnitude of the threshold is different for the modes and is largely influenced by the size of the particles, the properties of the material (cohesion between particles [Schmidt, 1982], geometry of the particles [Doorschot et al., 2004, Clifton et al., 2006] or surface structures [Filhol and Sturm, 2015]). The aeolian transport induces an evolution of the snow surface. Particles are entrained and transported along the surface. Due to their interaction with other particles they alter the surface such that structures like ripples, sastrugi, dunes or cornices can be formed. In many studies exploring the behavior of drifting particles sand was used. Models of drifting sand and snow often assume a steady flux in equilibrium with a certain (mean) wind speed [Bagnold, 1941, Kawamura, 1951, Owen, 1964, Dong et al., 2003]. Recent studies [Groot Zwaafink et al., 2013, Walter et al., 2014] show that this equilibrium is an approximation. Particularly for snow, studies report that the flux rates are highly unsteady and not coupled to constant wind speeds but rather to the fluctuations of the wind [Paterna et al., 2016]. Reasons for this dissimilar behavior are determined by the properties of the snow. Schmidt [1980] shows that cohesive forces are much larger than gravitational forces that lead to different results in the case of snow saltation compared to saltation of sand. A large number of studies looked at the numbers of particles



### **Chapter 3. Space - time dynamics of erosion/deposition versus horizontal mass flux of snow**

---

drifting in the saltation layer, either in field experiments in alpine regions [Schmidt et al., 1984, Meister, 1987, Gordon and Taylor, 2009, Gordon et al., 2009, Naaïm-Bouvet et al., 2010, 2011] or in polar regions [Nishimura and Nemoto, 2005]. Many experiments were performed in cold wind tunnels [Nishimura et al., 1998, Clifton et al., 2006] or used a modelling approach. The majority of these studies focused on the transport of snow in the saltation layer using snow particle counters therefore neglecting the contribution of creep and suspension modes. Studies observing the change of the snow surface were performed using terrestrial laser scanner [Trujillo et al., 2007, 2016, Grünewald et al., 2010] or by modeling the saltation and surface erosion [Meister, 1988, Pomeroy, 1991, Michaux et al., 2002, Doorschot et al., 2004, Vionnet et al., 2013, Comola and Lehning, 2017]. Particularly for experiments using terrestrial laser scans or aerial images, the temporal resolution generally is in the order of multiple hours or days (before and after a storm or snow fall event). This present study discusses the dynamics of the erosion and deposition of drifting snow at the snow surface in a high temporal resolution for experiments with drifting snow in a cold wind tunnel. In particular, we aim to investigate the relationship between the volume of the snow eroded from the surface and the number of particles in saltation mode recorded by the SPC. We also look at time scales of surface erosion versus mass flux maxima and draw conclusions on the space-time dynamics of the erosion process. The paper is structured as follows: Section 2 highlights the experiments and instruments used, in particular the newly introduced Kinect sensor as a low cost device to scan the snow surface during the experiments. In section 3 we introduce and discuss the results of this new approach with respect to the dynamics and quantity of the mass flux due to snow surface erosion. First with respect to the total set-averaged mass-flux, based on the difference of the surface height between the beginning of a set and the end. This represents the net amount of snow eroded/deposited during the time of the experiment. Secondly, we investigate the correlation between the integrated particle and surface mass fluxes. This is done with respect to size of the observed surface area (support area) as well as the saltation length scale used for the formulation of the saltation profile. The third focus is on the spectral distribution of the mass flux and the differences between particle and surface mass flux in respect to that. Based on these results we will discuss the dynamics of the surface erosion and how it effects the particle mass flux in the saltation layer.

## **3.2 Methods and Instrumentation**

The experiments were conducted in the SLF's cold wind tunnel situated in the Flüela valley near Davos, Switzerland at 1670 m a.s.l. The tunnel has a 6 meter long roughness fetch consisting of a row of spires and roughness elements and 8 meters of snow cover with the measurement section at its end. The inlet prior to the roughness fetch is made by a honeycomb grid followed by a 4:1 contraction. The wind tunnel is operated in suction mode such that the air is drawn through the inlet. The snow employed for the experiments was natural snow collected in metal trays outside the wind tunnel building. The tunnel was first introduced by Clifton et al. [2006]. For an experiment it was necessary to have a snow depth between 0.07 m and 0.15 m of fresh



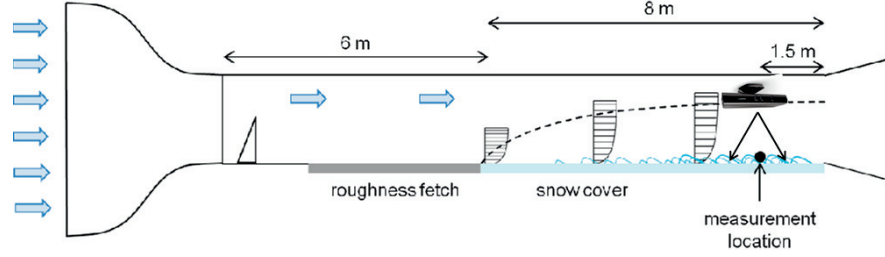


Figure 3.1: Schematic overview of the wind tunnel. The figure also show the location of the Kinect device. The device was attached to the ceiling of the wind tunnel enabling to observe the snow surface at the measurement location.

snow (Fig. 3.1).

For the recording of the freestream velocity ( $U_{free}$ ), the temperature and the relative humidity (RH) in the wind tunnel, a propeller-type anemometer with an integrated thermometer (Mini-Air 20, Schildknecht AG, Switzerland) was used. Particles in the saltation layer were recorded using the SPC sensor (SPC - S7, Niigata Denki Co.) as first introduced by Nishimura et al. [1998] and Sugiura et al. [1998]. The counting of the snow particles is based on the voltage change induced by snow particles passing the SPC's photodiode. Based on the amplitude of the voltage signal, a classification of the particle's diameter into 32 size classes between 0.04 mm and 0.5 mm is possible. We could accurately control the distance between the SPC and the snow surface and therefore ensure that the SPC sensor was close to the surface and at the same distance from the snow surface at all times. For the experiments presented in this work, the distance was set to 2 cm. At this place it must be noted that particles at the onset of saltation traveling below this height could not be detected even though on some test days they already had an influence on the snow surface change. Surface erosion (including creep) already starts at low wind speeds close to the threshold wind speed when the SPC measurements at 2 cm don't have sufficient particles recorded to allow reliable flux estimates.

To record the snow surface during the experiment, Microsoft's 'Kinect for windows'-device was used. The Kinect was first introduced in 2010 as a low-cost motion sensing input device for a video game console. It consists of an infra red (IR) emitter and sensor, a color camera, a microphone array and a tilt motor. The most important utility for this study was the IR emitter/sensor pair to record a three dimensional depth image of the snow surface. Besides the hardware, Microsoft also released a software platform to develop customized software for the Kinect devices.

Kinect devices are widely used in other fields like machine learning [Yavsan and Ucar, 2016], in medical studies (e.g. Prochazka et al. [2016]). Mankoff and Russo [2012] discussed possible

### Chapter 3. Space - time dynamics of erosion/deposition versus horizontal mass flux of snow

Table 3.1: Experiments in the winter season 2016

Test Day	Date	$U_{free,t}$ [ $\frac{m}{s}$ ]	$\rho$ [ $\frac{kg}{m^3}$ ]	T [ $^{\circ}C$ ]	RH %	# of sets
1	08.01	9.5	77	-1.5	92.3	17
2	12.01	8.0	63	-2.8	86.0	18
3	13.01	7.1	37.5	-4.6	76.6	16
4	18.01	6.7	68	-12.5	58.7	19
5	03.02	7.3	60	-2.1	76.3	16
6	04.02	7.1	50	-2.7	69.9	18
7	01.03	7.2	36	-1.1	72.8	11

applications of the Kinect sensor for geoscientific studies. A recent publication already showed an application of the Kinect device to measure glacial penitentes [Nicholson et al., 2016]. One advantage that the Kinect sensor has over traditional photogrammetric setups is that it comes precalibrated and does not need reference points (refer to subsection *Kinect mass-flux computation* for more details).

#### 3.2.1 Experiments

All experiments presented in this study were composed of steps with increasing wind speeds. The wind speeds started below the threshold wind speed for entrainment of particles of the snow and were increased to reach values that allowed strong erosion. In total we performed experiments on 7 days from the beginning of January 2016 to the beginning of March 2016. A total number of 115 steps were recorded. Each step lasted approximately 60 seconds. Prior to the first experiment of each test day, the snow density was measured. The snow density was later used for the calculation of the surface mass flux.

For the experiments in this study, the Kinect device was mounted on the roof of the wind tunnel pointing perpendicularly down on the snow surface. To record the color - and depth images, a software based on the Kinect Stream Saver application by Dolatabadi et al. [2014] was used. This allowed recording the Kinect's depth- and color image stream with a frequency of 30 Hz and a resolution of 640x480 pixel. The field of view (FOV) of the Kinect partly overlapped with the SPC. For the subsequent evaluation, the pixels containing this overlap were ignored in the analysis. Before recording at each step, the height of the SPC was adjusted such that it was 20 mm above the snow surface. Based on the erosion of the snow surface, this position was corrected after each step. The threshold freestream velocity  $U_{free,t}$  was chosen to be wind speed, at which the signal of the SPC record did show a first amount of few particle.

#### Kinect mass-flux computation

In the case of our studies, where the distance between sensor and snow was below 1 meter, the area that was covered and evaluated was approximately 0.90 x 0.68 m. The total area was reduced in the post processing in order avoid the pixel that covered the area overlapping

with the SPC. At this range, the nominal precision of the Kinect depth sensor is given as 1mm. Depending on the distance between sensor and target, the resolution of the FOV in the horizontal directions varies due to the fixed pixel numbers. In average, it resulted in a pixel area of approximately  $0.3 \text{ mm}^2$ .

Studies looking at the accuracy of the depth sensor [Essmaeel et al., 2014] denoted the need of filtering the data to avoid the signals noise. Essmaeel et al. [2012] describe a temporal denoiseing filter for that. In the present application, the filtering was not needed to be at real-time. It was sufficient to apply it in the post processing of the depth data. Therefore the temporal denoiseing did not improve the quality of the data compared to a common moving average filter. Given the noisy signal, the Kinects's depth time series were downsampled in time for each pixel from 30 Hz to 1 Hz by averaging and smoothing with a Savitzky-Golay moving average filter using MATLAB's *sgolayfilt* function. Besides the moving average temporal filter, we added a spatial 2D adaptive noise removal filter (MATLAB's *wiener2* function) to reduce the characteristic noise visible in the raw data that was introduced by the IR pattern of the Kinect device itself.

After smoothing the time series, the series were differentiated in order to calculate the change of the snow surface. This again was done by calculating the time-derivative of the depth of each pixel for the whole time series of the event. The Kinect device is able to calculate a three dimensional coordinate for each pixel using the skeletal stream framework provided in it's stream saver software. For the present study, this would have resulted in vast amount of data. Therefore we used a trigonometric approach to calculate the x- and y coordinates of each pixel in the post-processing.

$$x_{i,j} = 2 \tan(\beta \cdot (j - h/2 + X_o) \cdot z_{i,j}), \quad (3.1)$$

$$y_{i,j} = -2 \tan(\alpha \cdot (i - w/2 + Y_o) \cdot z_{i,j}) \quad (3.2)$$

with  $\beta$  the depth sensor's angle of the FOV along the x-direction,  $\alpha$  the angle along y-direction. The values for the angles  $\alpha$  and  $\beta$  were validated against the data of the skeletal stream.  $X_o$  and  $Y_o$  represent the offset to the centerline of the FOV in the respective direction.  $h$  is the total number of pixels in the x-direction,  $w$  the total number in y-direction.

In order to estimate the quality and precision of the Kinect device, we first conducted a calibration study. The geometrical calibration setup is shown in Figure 3.2. First a fresh snow surface was scanned with the Kinect. Afterwards, three wooden elements of 40x40x80 mm dimensions were placed and cautiously pressed in fresh snow and the setup was scanned. The last scan was after the elements were removed. The difference in snow surface height at the place where the elements were placed was measured and subtracted from the first scan. This

### Chapter 3. Space - time dynamics of erosion/deposition versus horizontal mass flux of snow

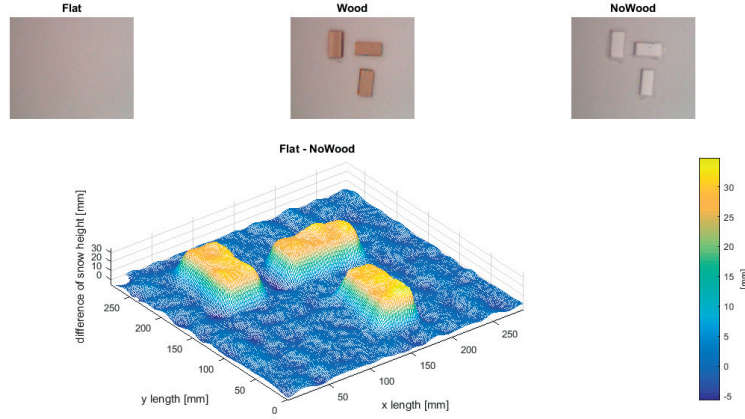


Figure 3.2: Kinect calibration setup. Kinect color view to the snow with and without wooden elements (upper row). Change of surface height between flat surface and surface after removing wooden elements.

way we could show that device measures the correct dimensions of the snow surface and needs no further calibration. From the tests we estimated that the absolute accuracy of the snow depth measurements is 1mm. But by performing the previously described post processing, the uncertainty within consecutive measurements is lower (since the 1mm precision is averaged to values below 1mm), just as described by Essmaeel et al. [2012].

The change of volume at each pixel  $dV_{i,j}$  was calculated based on the average pixel  $A_{i,j}$  area and the change in depth  $dz_{i,j}$

$$dV_{i,j} = A_{i,j} \cdot dz_{i,j}. \quad (3.3)$$

The mass loss/gain, represented with the term 'mass flux', at each pixel is then calculated as the sum of all volume changes multiplied by the snow density  $\rho_{snow}$  and the time between the time steps as the inverse sampling frequency  $f_s$  and the total measurement area  $A$

$$q_{i,j} = \frac{\rho_{snow}}{A} \cdot f_s dV_{i,j}. \quad (3.4)$$

Numerically integrating the mass flux at each pixel results in the mass flux time series by the snow surface erosion

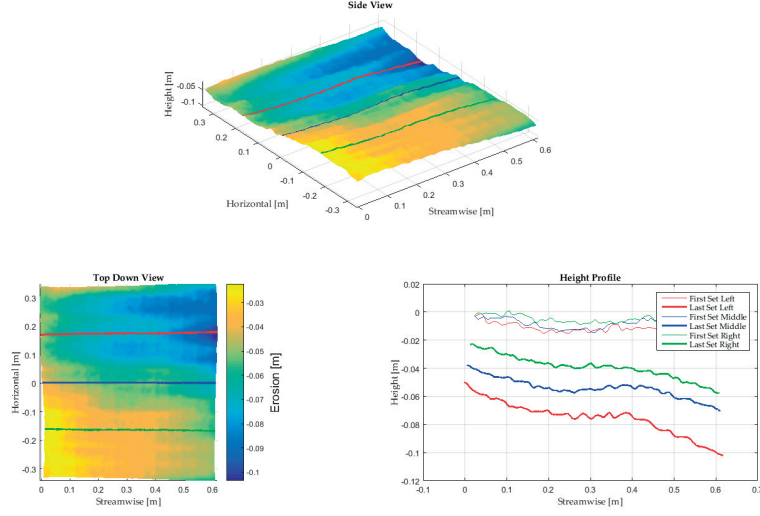


Figure 3.3: Kinect erosion depth in side view (top), in the horizontal plan (left) and the profile from before and after a test (right).

$$q_S(t) = \frac{1}{N} \sum_{i,j} q_{i,j}, \quad (3.5)$$

$$Q_S = \int_{t_0}^{t_{end}} q_S(t) dt \quad (3.6)$$

where  $N$  is the total number of pixels per frame. The numerical integration of the mass flux and mass flux time series by the total run time delivers the total, time-averaged mass-flux  $Q_S$ .

In addition to the mass fluxes we calculated the difference between the surface from the first to the last frame recorded in a set. This resulted in the total change of volume at the surface. Multiplied by the density of the snow and normalized by the total runtime of the set and surface area this resulted total, set-averaged mass-flux  $Q_{SB}$  and stands for a measure of the total set-averaged mass-flux balance. The main difference the calculation of the time-averaged surface mass flux is the sampling time.

In order to observe the influence of the size of the support area, we introduced a reduction factor  $RF$  with the values 1,2,4,8,16. The reduction factor acted as the approximate partition of the initial surface area (i.e.  $RF = 1$ , no reduction,  $RF = 2$ , half of side length and so on). Refer to the Appendix for more details.

### Chapter 3. Space - time dynamics of erosion/deposition versus horizontal mass flux of snow

---

#### SPC mass-flux computation

While the Kinect's depth sensor is able to measure the mass flux based on the change of the snow cover, the SPC measures the saltation mass flux on a small volume in the saltation layer above the snow cover. Following Kawamura [1948, 1951], Dong and Qian [2007] who express the mass-flux profile as a exponential decay, we used

$$q_P(z) = q_0 \cdot e^{-b \cdot (z - h_0)}, \quad (3.7)$$

with  $q_0$  equals the average SPC mass flux of the time series at the point measurement and  $h_0$  equals the height the SPC measurement location above the snow surface. Literature presenting this exponential decay function, e.g. Rassmusen [1985], Nalpanis et al. [1993], Dong and Qian [2007], reported large variability for the the parameter  $b$ . Our parameter  $b$  corresponds to the inverse of what is referred to as the length scale of the saltation system  $L = \frac{u_*^2}{\lambda g}$  [Guala et al., 2008].  $u_*$  is the friction velocity,  $\lambda$  is a constant parameter that defines  $L$  and  $g$  represents the gravitational constant. The value of  $\lambda$  varies in literature. We use for our calculations  $b$  based on the values by Clifton et al. [2006] and Guala et al. [2008] for their experiments in the same wind tunnel ( $L = 0.022$ ). In addition, we added a sensitivity analysis for values of  $\lambda$  between 0.18 and 1.17 (refer to appendix, table 5) to investigate how this value alters the relation between surface and particle mass flux. As described by [Guala et al., 2008], a small  $\lambda$  extends the height of the saltation layer, where a  $\lambda$  that approaches unity confines the saltation layer to close to the surface. The estimation of  $u_*$  was done according Gromke et al. [2011] following the law-of-the-wall using the averaged free stream wind velocity. The vertical expansion of the saltation layer was assumed to have a maximal height of  $z_{SL} = 0.12$  m. The exact number corresponded to an estimation based on visual inspections during the experiments. Since previous experiments in the same wind tunnel [Gromke et al., 2014] reported an exponential decay of the particle number with height, the chosen number seemed reasonable. The mass flux recorded by the SPC is integrated over the total height from  $z = 0$  to  $z = z_{SL}$ .

Assuming a linear increase of erosion along the streamwise direction the divergence of the vertically integrated mass flux profile  $Q_P$  was calculated. Based on the assumption of linear increase erosion, the divergence was calculated based on the division of the integrated mass flux by the length of the footprint of the erosion  $L_P$ .

$$Q_P = \frac{\int_0^{z_{SL}} q_P dz}{L_P} \quad (3.8)$$

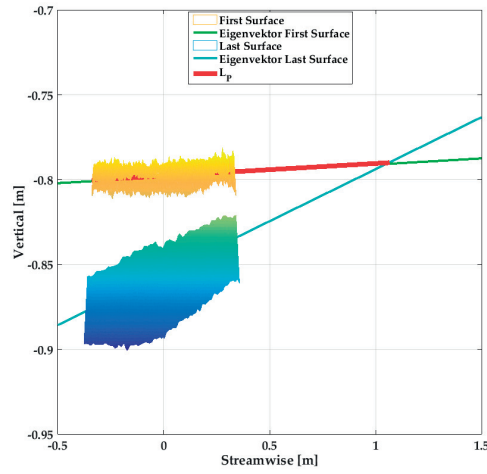


Figure 3.4: Procedure to calculate the saltation footprint length based on the values from Test Day 3. By means of the principal component analysis (PCA) the orthogonal eigenvalues for the snow surface before the experiment (First Surface) and the surface at the end of the experiment (Last Surface) were calculated. Using the two orthogonal, streamwise eigenvectors as well as the difference in height between the untouched surface before and the surface after the end of the experiment, a point of intersection between the two orthogonal vectors could be calculated. The length  $L_P$  was then given by the distance between the SPC and the point of intersection.

### Chapter 3. Space - time dynamics of erosion/deposition versus horizontal mass flux of snow

Table 3.2: Statistics of the two sets displayed in Fig. 3.5. On test day 1, the threshold wind speed was 9.45 m/s.

Test Day	Set	max. $U_{free,rel}$ [ $\frac{m}{s}$ ]	mean $q_S$ [ $\frac{kg}{m^2s}$ ]	Color
1	1	8.01	4.5e-4	—
1	16	15.04	2.8e-2	—

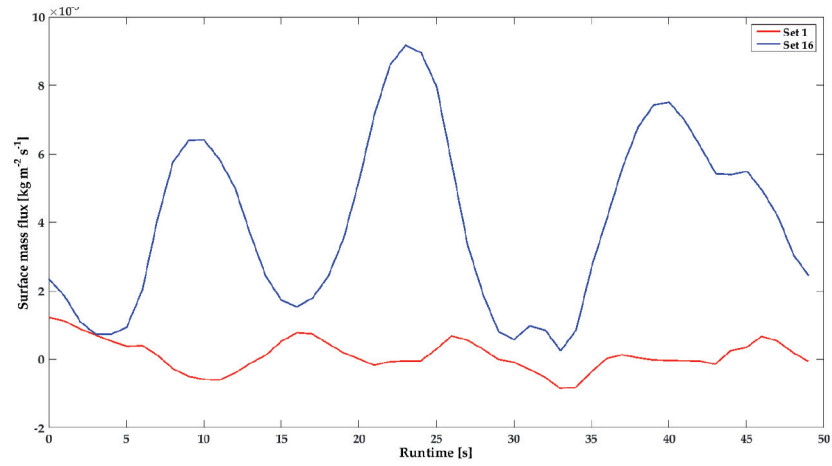
The footprint was estimated as the length before the particle counter at which the snow surface was eroded. In the case of the wind tunnel, where the saltation system develops after a rather short fetch length from zero, the first few meters of the snow surface looked very much unchanged after each experiment, independent of the snow properties. The calculation of the footprint length  $L_P$  is illustrated in Figure 3.4. The footprint length corresponds to the length, in which the snow surface is eroded assuming a linear increase of surface erosion with the length of the fetch. The calculated length was in good agreement with the approximate length that was observed by visual inspection.

### 3.3 Results and Discussion

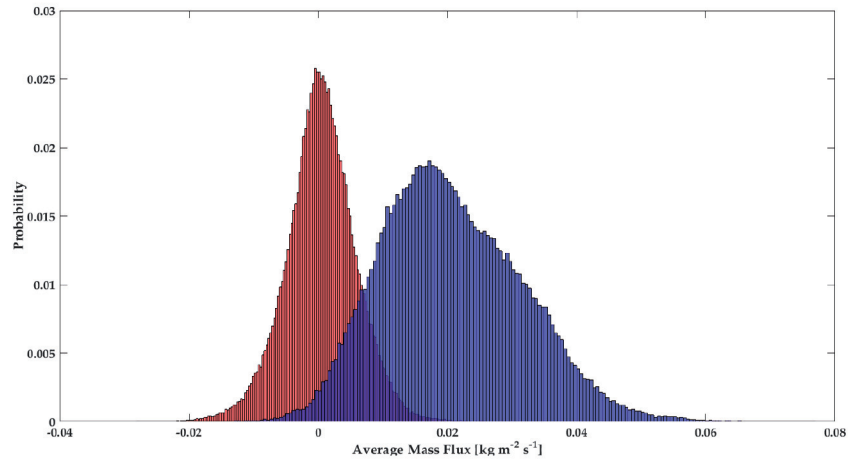
The conditions during the experiments conducted for this study are summarized in Table 3.1. Figure 3.5 displays a representative example of the results during a test day that should help to understand the dynamics of the surface erosion. Table 3.2 presents the mean free stream velocity and the net surface mass flux for the two sets in the example. The particle size distribution recorded with the SPC (not shown) for the two sets were very similar. We observed a reduction in the average particle diameter on the individual test days. One process leading to this reduction could be fragmentation of the snow during the tests [Vionnet et al., 2013]. But since we were constantly increasing the wind speed for each consecutive set, the slight decrease of the mean particle diameter may be explained by the fact that larger particles are easier entrained than smaller particles in the first sets at low wind speeds. With the given fetch length, the test routine, the duration of the tests and the conditions in the wind tunnel, we expected no significant change of the snow conditions during a test. Particularly from intermediate mass flux strength to high mass flux strengths, the diameter generally reduced very little or not at all. Density changes during erosion have been shown to be small [Sommer et al., 2018] and therefore we assume constant snow density for the surface flux calculation. This is of particular interest for the comparison of the mass flux from surface erosion with the horizontal particle mass flux.

Two time series of the surface mass flux signal recorded with the Kinect device are shown in Fig.3.5a. The red line represents a set with low mass flux, the blue line represents a set with high mass flux (see Tab.3.2). The negative values of the mass flux correspond to accumulation of snow mass, positive mass flux corresponds to erosion. These values in the time series represent the mass flux averaged over the FOV. Higher intermittency in the signal at lower

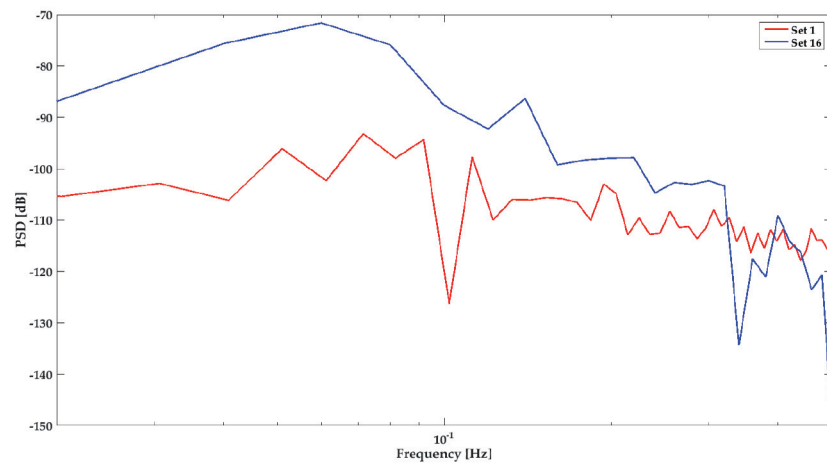




(a)



(b)



(c)

Figure 3.5: (a) Example of time series for two sets with different surface mass flux according Eq.3.5. Low mass flux (red) and high mass flux (blue). (b) Histogram of the mass flux for the same two sets. The histogram represents all surface mass flux values for each pixel and time step according Eq.3.4. (c) Power spectral density for the two time series (for the whole frame again).

### Chapter 3. Space - time dynamics of erosion/deposition versus horizontal mass flux of snow

---

mass fluxes originates from smaller mass flux activity. The red line in Fig.3.5a shows a time series of mass flux close to zero. This represents an equilibrium between overall accumulation and erosion in the Kinect's FOV. Although the time series of the SPC and the Kinect devices could be resampled to the same frequency, the processed time series themselves are not correlated very well since the temporal dynamics of the snow surface erosion recorded by the Kinect does not well describe the temporal dynamics in the saltation layer that is recorded with the SPC (refer to Fig. 3.6). We attribute this to the fact that we averaged the surface mass flux recorded with the Kinect over the whole area of the FOV. Therefore fluctuations in the temporal dynamics of the surface mass-flux were smoothed in comparison to the mass flux of the particles in the saltation layer recorded as a point measurement. At the surface, there is not only homogeneous erosion but constant erosion and deposition at different locations such that the mass flux is smoothed. In case of the horizontal particle mass flux, each particle contributes to the mass flux signal, independent of the specific type of surface changes it will produce upon impacting on the snow surface. Nevertheless, regarding the averaged mass flux from these time series, the two processes are correlating very well (refer to Fig.3.7).

Figure 3.5a also shows that with increasing free-stream velocity the individual peaks of the time series became not only larger in amplitude but also wider. This means that during events when strong erosion occurred, the peaks of the mass flux lasted longer compared to the peaks of smaller erosion at lower wind speeds. Paterna et al. [2016] revealed that in the wind tunnel strong saltation developed own saltation length scales independent of the of the turbulent forcing. These events of strong saltation have their highest power at low frequencies leading to longer lasting bursts of snow particles. Also in their subsequent study [Paterna et al., 2017], the authors show that in strong saltation peaks of high mass flux persist over a longer time and therefore lead to wider peaks.

Figure 3.5b displays histograms of the mass flux during the two time series from each pixel in the FOV. The results strongly support the previous argument that the equilibrium of erosion and deposition investigated at low mass flux is shifted towards predominantly erosion at high mass flux.

Figure 3.5c displays the power spectral density (PSD) of the two time series. The spectral analysis shows differences between equilibrium saltation at low mass flux and erosion dominated saltation as well as changes between surface mass flux and particle mass flux. At frequencies close to the sampling frequency, the PSD of high and low mass flux are similar. At low frequencies (below 0.1 Hz), particularly in the case of strong mass flux, the signal contains the most power while the power for the low mass flux case is more evenly distributed through the frequencies. This corresponds to what we expected from the observation of wider and longer lasting mass flux peaks of the time series and is in agreement with the results of Paterna et al. [2017].

Figure 3.6 shows the time series of set 16 (corresponding to the blue lines in the previous figure) observed before (i.e. RF 1) together with the time series of the high mass flux at reduced

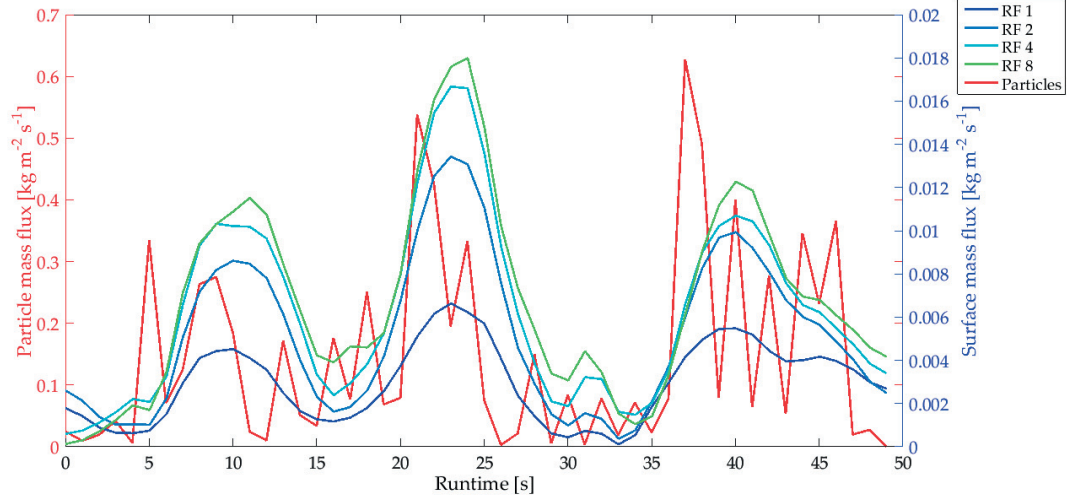


Figure 3.6: Mass flux time series of set 16 on test day 1. The particles mass flux on the left y-axis (red time series) and the surface mass flux on right y-axis (blue to green time series) for reduction factors (RF 1, 2, 4, 8) normalized by the corresponding surface area.

support areas (RF 2,4,8) as well as the particle mass flux of the SPC for the same set. The magnitude of the surface mass flux increases with decreasing surface area. This increase is based on the fact that the erosion is not uniformly in the crosswise direction. Reducing the FOV to the area in the middle of the wind tunnel, areas with less erosion close to the walls are dismissed. Therefore the magnitude increases. This pattern was consistent throughout sets with events of high mass flux on all test days. This time series further shows that the low frequency peaks of the surface mass flux correspond well with those of the particle mass flux for all RFs, which reflects once more results by Paterna et al. [2017] that strong saltation is characterized by longlasting, wide peaks and that the predominant mechanism of entrainment is by splash-entrainment leading to strong erosion.

### 3.3.1 Set-averaged and time-averaged mass-flux

As stated previously, we calculated the total, set-averaged surface mass flux  $Q_{SB}$  for each set based on the total mass that was eroded/deposited within the time of the recording by subtracting the first surface record of a set from the last record of the same set. This way, the temporal information is lost but it becomes possible to compare the integrated particle mass flux profile ( $Q_P$ ) (ref. Eq. 3.8) to the change of the surface. To compare  $Q_P$  to  $Q_{SB}$ , we calculated the correlation between the two of them for each set within one test day as well as the overall correlation for all sets in dependence of the reduced surface area (refer to the AppendixA, table 3). In the case of  $Q_{SB}$  for the unreduced surface (i.e. RF = 1), the correlations for the individual events vary largely. Certain events do not correlate (i.e. on test day 6) but some had a very good correlation. Considering all 115 events, the  $Q_{SB}$  does correlate with the averaged particle mass flux ( $r = 0.572$ ). Interestingly, for the case of the reduced support area

### Chapter 3. Space - time dynamics of erosion/deposition versus horizontal mass flux of snow

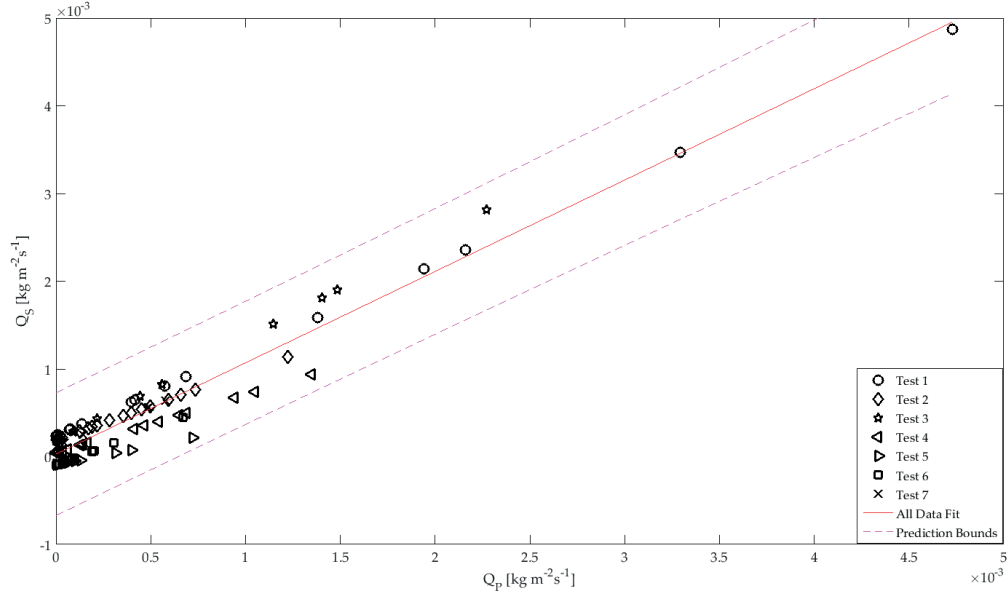


Figure 3.7: The red line represents the fit for total mass fluxes ( $Q_S$  vs  $Q_P$ ) of all 115 sets from 7 test days. The different marker represent different test days. The 95% confidence interval as the given by the dashed lines.

(RF 2,4 and 8) the correlation is significantly better (up to  $r = 0.935$  for RF 2 and 4).

Figure 3.7 shows the results of the correlation analysis between the time-averaged surface mass-flux  $Q_S$  and the integrated particle mass-flux profile  $Q_P$ . Compared to the previous results for the set-averaged surface mass-flux, the time-averaged surface mass-flux correlates significantly better ( $r = 0.930$ ) at the full surface area resolution. The results in the AppendixA, table 4 show again a higher correlation for the reduced support area (higher than  $r = 0.94$  for RF 2 and 4).

Considering both, the set-averaged and the time-averaged mass flux judged on the correlation values and more particularly on the significance values it shows that the time-averaged mass flux is more robust. This also suggests that the sampling frequency needs to be chosen high enough for a comparison of the two mass fluxes.

In both cases,  $Q_{SB}$  (Table 3) as well as  $Q_S$  (Table 4) the better correlation for the smaller support area (i.e. RF = 2 and RF = 4) is attributed to the fact that in the case of the reduced surface area, the focus is set on the surface just in front of the particle counter. Another result visible in Figure 3.7 is that in the case of time-averaged surface mass flux ( $Q_S$  on the y-axis), the mass flux is closely around zero for most sets with low and intermediate mass flux strength, suggesting that there is equilibrium between erosion and deposition similar to what was presented in Figure 3.5b. This equilibrium shifts towards erosion only ( $Q_S > 0$ ) in the case of stronger mass flux.

In the case of the parametric study on the saltation-length-scale parameter  $\lambda$ , the results were proportional and therefore the correlation was not influenced significantly. More interesting for that study were the results of linear regression for the particle mass flux and the surface erosion

$$Q_S = p1 \cdot Q_P + p2. \quad (3.9)$$

The overview over the results of the regression coefficients is displayed in the AppendixB, table 6 for the set-averaged mass flux and table 7 for the time-averaged mass flux. Looking at the regression coefficient over all events (*All p1*), we find that in the case of set-averaged mass flux,  $p1$  increases with increasing  $\lambda$  from 0.676 to 1.069. First, this means that the estimated mass change from the integrated particle mass-flux is slightly larger or closely the same as the set-averaged mass-flux at the surface. Second, that for a  $\lambda$  with  $p1$  close to one, the integrated particle mass-flux is a good estimator of the total change at the surface. Having the best fit at  $\lambda = 1$  means that for the set-averaged mass-flux, the mass flux profile is confined near the surface. Noteworthy is that in the case of  $Q_{SB}$ , the variability in the regression coefficient is relatively high for  $\lambda$  close to one and is becoming smaller with a smaller  $\lambda$ . When considering the time-averaged surface mass-flux  $Q_S$ , the relation is very similar ( $p1$  ranges between 0.612 to 0.970), meaning that the time-averaged surface mass-flux is slightly smaller than the integrated particle mass flux profile for all five values of  $\lambda$ . Again, the best fit is achieved with  $\lambda = 1$ . This means that by assuming the mass transport closely confined to the surface, the integrated particle mass-flux profile best represents the change of mass by erosion and deposition. By comparing the absolute numbers for integrated particle mass-flux for  $\lambda = 0.18$  and  $\lambda = 1.17$  we show that the latter is significantly smaller. This means in the case of our studies, assuming a high saltation layer overestimates the total integrated particle mass-flux.

#### 3.3.2 Spectral distribution

As stated at the beginning of this section, we use the mass-flux power spectra to characterize differences between surface and particle mass fluxes. We have already shown in the introductory example a difference in the spectrum between high and low mass flux. Figure 3.8 shows the spectra over all events for the different reduction factors. All spectra are scaled to their value at 0.01 Hz and averaged in frequency classes of 0.05 Hz. For the subsequent analysis and presentation the sets were separated in low, intermediate and high mass flux based on the time-averaged mass flux strength on the individual test day. Additionally to the spectrum of the surface mass-flux, the spectrum of the particle mass-flux was added. It is easily visible that in the case of the particle mass-flux, the power is evenly distributed through the spectra while the surface mass-flux has its largest power at low frequencies and it decreases rapidly towards higher frequencies. Another interesting result is that for the low mass flux, there seems to be

### Chapter 3. Space - time dynamics of erosion/deposition versus horizontal mass flux of snow

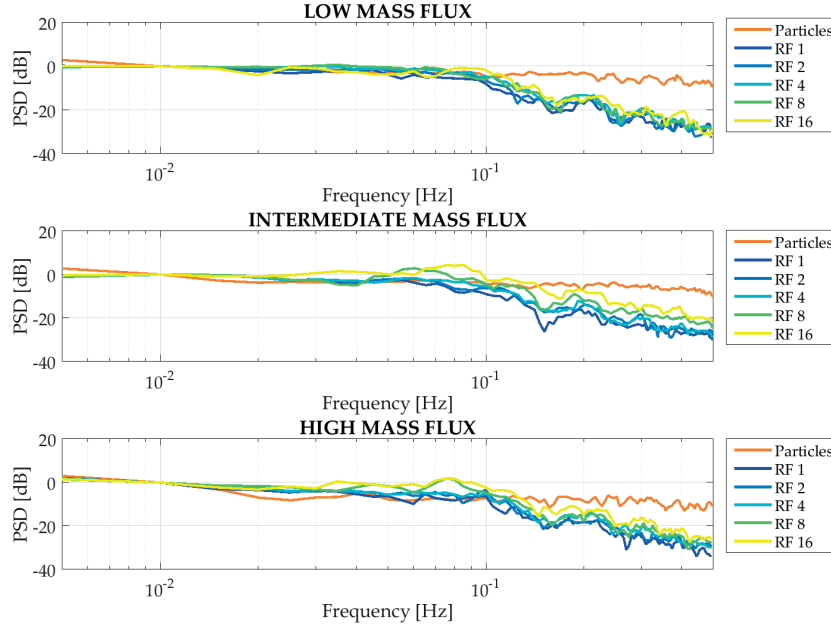


Figure 3.8: Power spectral density for different reduction factors.

no relevant difference in the spectra dependent on the reduction factor. For the intermediate mass flux and certainly for the high mass flux, in the region between  $3 \times 10^{-1}$  to  $10^{-1}$  Hz, the power increases with a decreasing support area. We explain this behavior based on the fact that for low mass fluxes, the differences between the individual test days are not as large as for the high mass fluxes. Also for low mass flux strengths, we experienced a more homogeneous surface change in crosswise direction. The higher the wind speeds became, the higher the variability became. Some extent of this variability may originate by the influence of the side walls, although a quantification of this influence was not possible. This crosswise variability is also reflected in the differences of the spectra at depending on the mass flux strength as well as for the support area.

Figure 3.9 displays the spectra based on the mass flux for the individual surface reduction factors as well as the particle mass-flux for all seven test days. As in the previous figure, the PSD for the particle flux is evenly distributed through all frequencies, independent of the mass flux strength. Observing the PSD as a function of the size of the support area, we find that with increasing surface area the power is more evenly distributed in the spectra. I.e. at RF 1, the gradient of the slope at a frequencies of approximately  $10^{-1}$  is relatively smooth and becomes sharper with increasing RF. We hypothesize the smoother change at larger observation areas (i.e. RF 1) to the fact that at larger areas, changes due to small-scale events are smoothed more compared to a much smaller area. Unlike the small-scale events at higher frequencies, the slow, larger-scale events of the erosion/deposition occur over the whole FOV and are less

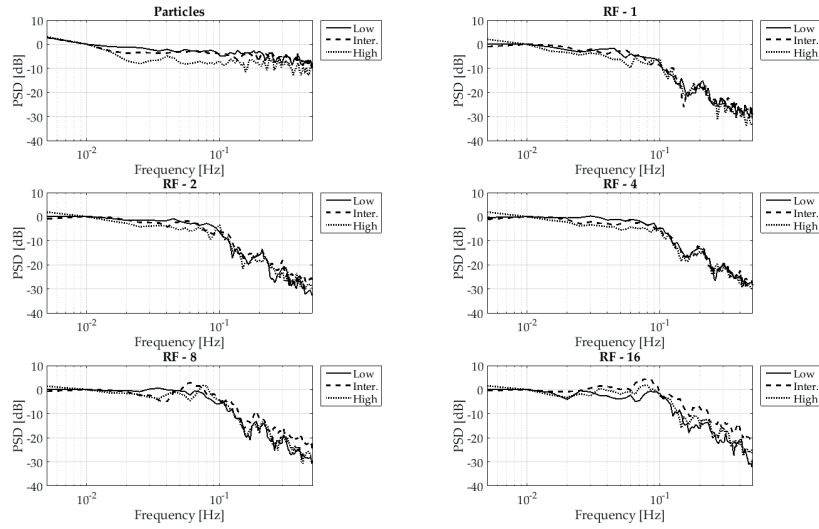


Figure 3.9: Power spectral density for high, intermediate and low mass flux.

dependent of the reduction factor. Therefore, the slow, large events of the erosion/deposition dynamics are more dominant in the spectra.

Figure 3.10 displays the unnormalized spectra for the two different test days. On Test day 1, we experienced the highest mass flux. On test day 4, the relative mass flux strength was much smaller. Again the spectra of the particle mass-flux look very much alike from their shape. But other than in Figure 3.8, the unnormalized PSD shows a significant separation of the power dependent on the mass flux strength. Interestingly, for both test days, the power spectra are much closer together in the case of the surface mass flux. Still the power is highest in the case of the high mass flux, but the gap between high and low mass flux cases is much smaller, particularly at higher frequencies. In the case of the two test days, reducing the support area by a factor two does not show a significant change in the shape of the PSD. Furthermore there is no significant separation of the spectra for the intermediate and low mass flux case. Only the shape for the high mass flux case looks different, particularly for test day 1 (which had the strongest mass flux in absolute numbers over all experiments) at low frequencies. This is again in line with the results of Paterna et al. [2017] which describe that the duration of events of strong erosion are longer compared to weaker erosion.

### 3.4 Conclusions

The present study establishes a link between the dynamics of the erosion and deposition of snow during an event of drifting and blowing snow at the surface and the snow particles recorded in the saltation layer. By means of a newly developed Kinect measurement system to the wind tunnel it was for the first time possible to observe and record the erosion and deposi-



### Chapter 3. Space - time dynamics of erosion/deposition versus horizontal mass flux of snow

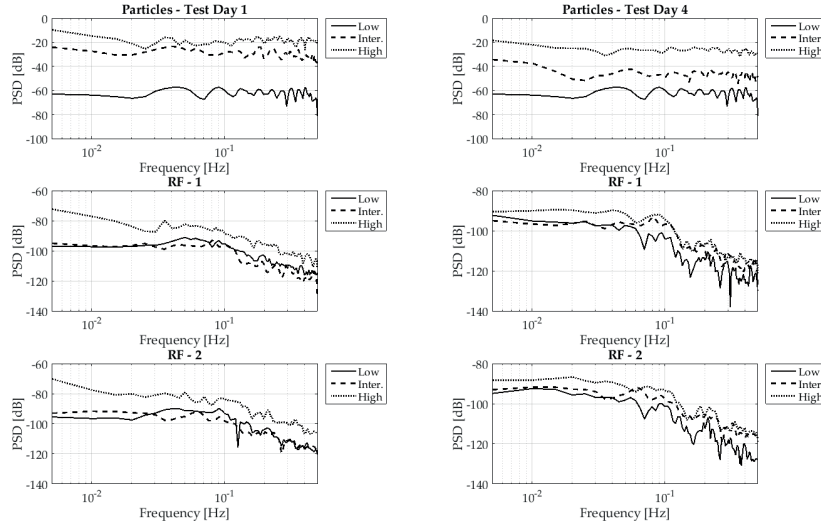


Figure 3.10: Unnormalized power spectral density for high, intermediate and low mass flux for test day 1 (left column) and test day 4 (right column).

tion with a relatively high temporal and spatial resolution as well as measure a quantitative set-averaged mass-flux of the total mass eroded.

A large proportion of the source of the snow transported in the saltation layer can be observed by recording the particle induced change of the snow surface due to erosion and deposition. Although the Kinect's accuracy is not sufficient to record individual particles, it is possible to record the contribution of the sum of all particle surface interaction such as deposition at the surface, aerodynamical entrainment or entrainment of particles on the surface due to 'splash-entrainment' from impacting particles.

During the different experiments a representative variety of snow- and environmental conditions were experienced. For the seven test days the threshold wind speed, maximum particle mass flux and snow density were different (see Tab.3.1). We observed an equilibrium between erosion and deposition at lower mass fluxes which shifts to predominantly erosion for higher mass fluxes. This study also shows that despite the fact that the temporal dynamics of the mass flux derived from the surface change was significantly different from the particle mass flux in the saltation layer, their average mass flux correlates very well, particularly in case of test day with strong erosion. The correlation can be improved further by reducing the observed snow surface and focusing to a smaller area in front of the SPC. The parametric study for the saltation length scale demonstrated that the best fit between surface mass flux and particle mass flux is achieved for a saltation-length-scale parameter  $\lambda$  close to 1, which translates to a saltation layer that is confined near the surface. The study highlights significant differences in the mass flux between particle saltation and snow surface erosion. The latter has the most power at low frequencies, particularly when considering smaller areas, while the power of the



particle mass flux is distributed more evenly through the spectra of the observed frequencies. Despite these differences in the characteristic of the temporal dynamics of the mass flux the high correlation suggests that changes of the snow surface are very well represented in the particles recorded by the SPC when we consider long averaging windows. We can therefore conclude that the integrated particles mass-flux signal in the saltation layer can be used to quantify the mass eroded on the surface, which would allow to estimate the total mass change from SPC measurements of the particle mass flux only.

Readers should consider that this study was performed in a wind tunnel with constant wind speed. This allowed us to control the erosion in the experiments. The limited snow fetch available for snow saltation, a inherent limitation of any wind tunnel experiment, implies that while equilibrium saltation is observed at low mass-flux, at higher mass-flux erosion tends to dominate. Performing a similar study in the field, would lead to test our results in case of saltation with a longer flux footprint and under variable wind speeds, a much more complex situation which would likewise be influenced by the formation of snow bedforms.

#### **Acknowledgements**

The authors wish to express their acknowledgment to the Swiss National Science Foundation (SNF) for funding this research (R grant No. 200021-147184) and the wind tunnel facility (R'Equip grant No. 2160-060998).

## **A Surface area reduction**

For each values reduction factor  $RF$ , both side lengths of the observation area were divided through the corresponding number. Therefore the value of  $RF$  represent the power of 2 used to reduced the observed surface area of the Kinect. I.e.  $RF = 2$  means  $\frac{1}{2}$  of the full side length in streamwise direction and  $\frac{1}{2}$  of the full side length in crosswise direction. This results in  $\frac{1}{2}$  of the full surface area used for the mass flux calculation.

Table 3: Correlation of particle mass flux and set-averaged surface mass flux for different reduction factors.

RF	Event	event $r^2$	event p	All $r^2$	All p
1	1	0.759	4.06E-04	0.572	2.99E-11
	2	0.887	9.42E-07		
	3	0.931	1.72E-07		
	4	0.469	4.27E-02		
	5	0.343	0.194		
	6	-0.061	0.818		
	7	0.740	0.009		
2	1	0.967	3.73E-10	0.935	2.60E-52
	2	0.900	3.61E-07		
	3	0.932	4.16E-07		
	4	0.935	4.29E-09		
	5	0.431	0.095		
	6	0.814	1.00E-04		
	7	0.582	0.060		
4	1	0.970	1.35E-10	0.935	1.17E-54
	2	0.885	1.03E-06		
	3	0.927	2.48E-07		
	4	0.934	5.20E-09		
	5	0.476	0.062		
	6	0.632	6.51E-03		
	7	0.710	0.014		
8	1	0.958	1.47E-09	0.920	2.56E-47
	2	0.761	2.47E-04		
	3	0.920	4.37E-07		
	4	0.879	7.51E-07		
	5	0.490	0.054		
	6	0.398	0.114		
	7	0.667	0.025		
16	1	0.928	7.87E-08	0.899	7.26E-42
	2	0.625	5.56E-03		
	3	0.898	2.40E-06		
	4	0.735	3.39E-04		
	5	0.686	0.003		
	6	0.477	0.053		
	7	0.662	0.027		

Table 4: Correlation of particle mass flux and time-averaged surface mass flux for different reduction factors.

RF	Event	event $r^2$	event p	All $r^2$	All p
1	1	0.959	1.36E-09	0.930	1.59E-50
	2	0.878	1.66E-06		
	3	0.931	1.61E-07		
	4	0.928	1.01E-08		
	5	0.609	0.012		
	6	0.801	5.00E-04		
	7	0.753	0.007		
2	1	0.965	3.90E-10	0.943	2.14E-55
	2	0.889	8.13E-06		
	3	0.935	1.16E-07		
	4	0.934	4.98E-09		
	5	0.587	0.017		
	6	0.734	0.001		
	7	0.699	0.017		
4	1	0.970	1.33E-10	0.942	9.65E-55
	2	0.879	1.60E-06		
	3	0.926	2.58E-07		
	4	0.932	6.82E-09		
	5	0.466	0.069		
	6	0.582	0.014		
	7	0.703	0.016		
8	1	0.959	1.38E-09	0.921	1.24E-47
	2	0.773	1.69E-04		
	3	0.920	4.72E-07		
	4	0.880	6.96E-07		
	5	0.480	0.060		
	6	0.419	0.094		
	7	0.628	0.038		
16	1	0.928	7.81E-9	0.899	4.52E-42
	2	0.629	0.005		
	3	0.898	2.28E-06		
	4	0.711	6.35E-04		
	5	0.689	0.003		
	6	0.700	0.002		
	7	0.669	0.024		

## **B Saltation length scale**

The saltation length scale  $L = \frac{u_*^2}{\lambda g}$  was introduced earlier in section 3.2.1 for the calculation of the particle mass flux profile in the saltation layer. The literature stated different values for the constant parameter  $\lambda$ . Therefore we performed a sensitivity analysis with based on some values given in the literature.

Table 5: Values for  $\lambda$  given in literature and the resulting mean L-Value.

$\lambda$	Mean L-Value	Source
1.17	0.158	Guala et al. [2008]
1	0.063	Guala et al. [2008]
0.8	0.036	Pomeroy and Gray [1990]
0.45	0.028	Nishimura and Hunt [2000]
0.18	0.024	Guala et al. [2008]

Table 6: Linear regression coefficients for particle mass flux and set-averaged surface mass flux for different  $\lambda$ .

$\lambda$	Event	event p1	event p2	All p1	All p2
1.17	1	1.012	-5.48E-04	1.069	-3.45E-04
	2	0.765	2.31E-04		
	3	1.226	2.23E-04		
	4	1.231	-5.71E-04		
	5	4.326	-0.002		
	6	-0.123	-1.38E-04		
	7	1.141	1.03E-04		
1	1	0.956	-5.47E-04	1.010	-3.40E-04
	2	0.729	2.33E-04		
	3	1.183	2.27E-04		
	4	1.162	-5.67E-04		
	5	4.161	-0.002		
	6	-0.117	-1.38E-04		
	7	1.117	1.04E-04		
0.8	1	0.886	-5.48E-04	0.935	-3.37E-04
	2	0.675	2.35E-04		
	3	1.106	2.30E-04		
	4	1.070	-5.64E-04		
	5	3.875	-0.002		
	6	-0.109	-1.38E-04		
	7	1.058	1.05E-04		
0.45	1	0.754	-5.53E-04	0.792	-3.45E-04
	2	0.554	2.35E-04		
	3	0.903	2.32E-04		
	4	0.888	-5.64E-04		
	5	3.155	-0.002		
	6	-0.092	-1.37E-04		
	7	0.868	1.06E-04		
0.18	1	0.648	-5.63E-04	0.676	-3.64E-04
	2	0.446	2.32E-04		
	3	0.704	2.27E-04		
	4	0.738	-5.70E-04		
	5	2.473	-0.002		
	6	-0.078	-1.37E-04		
	7	0.662	1.05E-04		

### Chapter 3. Space - time dynamics of erosion/deposition versus horizontal mass flux of snow

---

Table 7: Linear regression coefficients for particle mass flux and time-averaged surface mass flux for different  $\lambda$ .

$\lambda$	Event	event p1	event p2	All p1	All p2
1.17	1	0.772	1.88E-03	0.966	2.93E-05
	2	0.723	1.47E-03		
	3	1.139	1.16E-03		
	4	0.591	2.23E-04		
	5	0.411	-0.003		
	6	0.662	-0.002		
	7	0.914	1.13E-04		
1	1	0.730	2.62E-04	0.970	1.24E-05
	2	0.689	1.97E-04		
	3	1.100	1.82E-04		
	4	0.559	4.32E-05		
	5	0.392	-9.41E-05		
	6	0.626	-8.86E-04		
	7	0.895	1.14E-04		
0.8	1	0.677	2.61E-04	0.898	1.42E-05
	2	0.638	1.98E-04		
	3	1.029	1.85E-03		
	4	0.516	4.43E-05		
	5	0.363	-9.35E-05		
	6	0.578	-8.85E-05		
	7	0.848	1.15E-04		
0.45	1	0.577	2.55E-04	0.747	1.30E-05
	2	0.524	1.99E-04		
	3	0.840	1.87E-04		
	4	0.426	4.434E-05		
	5	0.295	-9.35E-05		
	6	0.488	-8.93E-05		
	7	0.696	1.15E-04		
	std	0.178	1.39E-04		
0.18	1	0.497	2.46E-04	0.612	7.52E-06
	2	0.421	1.99E-04		
	3	0.655	1.82E-04		
	4	0.350	4.51E-05		
	5	0.235	-9.38E-05		
	6	0.414	-9.13E-05		
	7	0.531	1.15E-04		

## 4 Spatiotemporal dynamics of short term erosion/deposition in drifting and blowing snow

### 4.1 Introduction

Changes of the snow surface happen always and everywhere. Obvious reasons are precipitation or melting. But changes also occur due to metamorphosis processes such as sintering and settlement. Even without precipitation, melting and sintering, one main contributor to the development of snow surface structures is the mechanical interaction between the wind-driven moving particles and the snow surface. Qualitative descriptions of surface structures, bedform and changes due to drifting and blowing snow have been initiated by Cornish [1914]. It has been shown that blowing and drifting snow are relevant for many processes such as the melt rate of sea ice [Petrich et al., 2012] or the increasing of the surface roughness and therefore momentum transfer from the atmosphere [Castellani et al., 2014, Amory et al., 2017]. An overview of the different bedforms based on size, shape and process of formation have been presented by Kobayashi and Ishida [1979] and Filhol and Sturm [2015]. Kobayashi and Ishida [1979] distinguished these bedforms in four types based on the dominant process for the formation:

- Deposition type (deposition dominant): dunes, ripples, barchans;
- Erosion type (erosion dominant): sastrugi, pits;
- Equilibrium type (deposition and erosion in equilibrium): ripples, small sastrugis;
- Deposition/erosion type (deposition and erosion alternating): snow-waves.

Not only the bedform types have a classification, but also the nature of the drifting particles is categorized. As initially described for sand [Bagnold, 1941], drifting and blowing snow particles have three modes of transport: suspension, saltation and creep. The decisive criterion to distinguish the modes is the time during which particles are airborne. The transport mode depends on the particle size, the shear stress applied by the turbulent flow and on the interaction between neighboring particles. The transport modes that are most relevant to the

#### **Chapter 4. Spatiotemporal dynamics of short term erosion/deposition in drifting and blowing snow**

---

erosion and deposition and therefore to the formation of the bedform are creep and saltation. According to Filhol and Sturm [2015] snow ripple marks require creep for their formation. A common device to quantify particle mass flux is the snow particle counter (SPC), which measures the saltation flux at one height.

Changes of the snow surface have a spatial and temporal variability in the order of meters and seconds. Studies on the changes of the snow surface have been performed using remote sensing tools, employing laser scans, satellites or aerial imagery. Trujillo et al. [2016] used a terrestrial laser scanner to record an area of 100 m x 100 m before and after a storm on the antarctic sea ice. They characterized changes in the surface topography with a high spatial resolution. Based on the TLS scans they estimated the snow mass balance for the storm event. Nevertheless this study lacked a sufficient temporal resolution and could not resolve the process at time scales in the order of minutes or finer, which is required to understand the temporal dynamics of these surface changes. A promising study was presented by Picard et al. [2016], they developed a new device consisting of a laser meter able to scan a area of 100-200 m<sup>2</sup> in 4 hours. The device was tested over several months in Antarctica and the Alps. The study mainly addressed the instruments accuracy. Nevertheless, the technology could close the gap between TLS and location bounded snow height measurements of weather stations. An interesting study with respect to the snow surface changes was published recently by Groot Zwaafink et al. [2013]. The authors reported that for many events, snow was deposited on a table situated 1 m above the snow surface, but not the snow surface, leading to the conclusion that although drifting snow occurs, it often won't lead to changes on the snow surface or affect its height.

An other branch of field studies focused on the temporal quantification and description of mass flux of particles. A study from Paterna et al. [2016] reported that the snow saltation in events of high saltation intensity in a wind tunnel decouples from the turbulence motion. Aksamit and Pomeroy [2016] installed an outdoor application of particle tracking velocimetry to observe near-surface particles during drifting snow. In their results they highlight the importance of creep to the initiation of blowing snow transport and that low-energy (in terms of kinetic energy) grains considerably contribute to the saltation. They also found that this process is significantly dependent on the hardness of the snow bed. In contrast to the results from the wind tunnel setup, Aksamit and Pomeroy [2016] reported that near-surface particle velocities reflected instantaneous wind speed fluctuations and did not achieve equilibrium.

So far, studies evaluating drifting snow have only considered particle transport above the snow surface focusing on the saltation layer or analyzed changes on the snow surface mostly relying on TLS scans. The scans were able to provide precise spatial information but lacked temporal resolution. On the other hand, in a recent study Crivelli et al. [2017] introduced the Kinect device which enables to record surface changes at a high temporal variability but lacks spatial coverage in comparison to the TLS scans. The scope of the paper is to combine the spatial and temporal information at high resolution to better understand the dynamics of erosion and deposition during and due to drifting. Based on field measurements using a



Kinect device we investigate changes of the snow surface as a result of drifting and blowing snow on a small scale. These measurements are compared and discussed with results from wind tunnel measurements. These findings are compared to SPC measurements in Antarctica as well as data from repeated laser scans that cover the area around the SPC measurement locations.

## **4.2 Methods and Instrumentation**

### **4.2.1 Wind tunnel**

The wind tunnel experiments were conducted in the SLF's cold wind tunnel situated in the Flüela valley near Davos, Switzerland at 1670 m asl. The tunnel has a six meter long roughness fetch consisting of a row of spires and roughness elements followed by eight meters of snow cover. The measurement section is located at the last few meters of the snow cover prior to the outlet. A more detailed description of the wind tunnel set-up is available from Crivelli et al. [2016] and Paterna et al. [2017]. The natural snow for the experiments is collected in metal trays in front of the wind tunnel and carefully deployed into the wind tunnel as soon as the accumulated snow reaches a depth between 0.07 m and 0.15 m.

Recording snow particles in the saltation layer is done by means of a SPC sensor (SPC - S7, Niigata Denki Co.). In contrast to the version used in the field, the SPC is fixed in streamwise direction. Based on the number of particles and the corresponding diameter, the particle mass flux can be calculated. Prior to each new measurement series, the distance between the SPC and the snow surface was set to a fixed distance of 0.02 m above the snow surface.

### **Experiments**

All wind-tunnel experiments presented in this study are composed of steps of increasing wind speeds. The wind speeds started below the threshold wind speed for entrainment of particles from the snow and were increased for every new step to reach values that allowed strong erosion. In total we performed experiments on 12 days over two winter seasons 2016 and 2017 between beginning of January to the beginning of March. A total number of 176 steps were recorded, which should be sufficient to represent the typical range of conditions. Each step lasted approximately 60 seconds. Prior to the first experiment of each test day, the snow density was measured.

The field of view (FOV) of the Kinect partly overlapped with the SPC. For the subsequent evaluation, the pixels containing this overlap were ignored in the analysis. Prior to the recording, at each step the height of the SPC was adjusted such that it was 20 mm above the snow surface. The threshold freestream velocity  $U_{\text{free,th}}$  is defined as the wind speed, at which a sufficient amount of mass flux was recorded in the SPC time series.

## Chapter 4. Spatiotemporal dynamics of short term erosion/deposition in drifting and blowing snow

Table 4.1: Wind-tunnel experiments in the winter season 2016 and 2017

Test Day	Date	$U_{\text{free,th}} [\frac{m}{s}]$	$\rho [\frac{kg}{m^3}]$	T [ $^{\circ}C$ ]	RH %	# of sets
1	08.01.2016	9.5	77	-1.5	92.3	17
2	12.01.2016	8.0	63	-2.8	86.0	18
3	13.01.2016	7.1	37.5	-4.6	76.6	16
4	18.01.2016	6.7	68	-12.5	58.7	19
5	03.02.2016	7.3	60	-2.1	76.3	16
6	04.02.2016	7.1	50	-2.7	69.9	18
7	01.03.2016	7.2	36	-1.1	72.8	11
8	10.01.2017	6.5	55	-7.4	79.4	11
9	13.01.2017	6.2	77	-6.6	70.8	16
10	06.02.2017	8.1	49	-1.8	83.5	15
11	07.02.2017	9.5	63	-3.9	77.5	13
12	07.03.2017	7.7	43	-0.2	60.4	6

### 4.2.2 Field experiments

#### Weissfluhjoch

The field experiments were carried out a few tens of meters south of the SLF field site on Weissfluhjoch (WFJ) on an elevation of 2540 m asl (coordinates WGS 84 N 46° 49', E 9° 48') very close to the place of earlier drifting snow observations [Doorschot et al., 2004]. In the field, two masts were installed in late fall. One mast was carrying the setup of measurements instruments, the other carried the electronic control unit as well as the power supply. The station is equipped with two Young wind monitors (HD, Alpine Version, model 05108-45), a Campbell Scientific CSAT3B sonic anemometer, a CS SR50A ultrasonic snow depth sensor, a CS CS215 temperature and relative humidity probe, an Apogee Instruments SI-111 infrared radiometer to measure the snow surface temperature and a Niigata Electric Snow Particle Counter (SPC-95) measuring the number and size of saltating particles. The SPC-95 version is specifically designed for field use. It is mounted on bearings and has two vertical wings at its end, to allow alignment of the SPC with the flow. The device separates the fly-by particles into 64 bins based on their average particle diameter covering a range from 0.04 - 0.5 mm. The station was autonomously powered by a solar panel and a small wind turbine attached to a battery box (refer to Fig.4.1). In addition to the previously presented instruments, at WFJ we mounted a Microsoft 'Kinect for windows'-device to observe the snow surface changes in very high temporal resolution. The Kinect device was first introduced in 2010 as a low-cost motion sensing input device for a video game console. It consists of an infrared (IR) emitter and sensor which enables recording a depth image, a color camera, a microphone array and a tilt motor. Along with the hardware, Microsoft provides a software development platform to customize the software for the individual applications of the device. Prior to this study, the Kinect device proofed its capability to record surface changes in geophysical applications and

## 4.2. Methods and Instrumentation

Table 4.2: Field experiments on WFJ in the winter season 2017. The average wind speed was calculated from the CSAT3B sensor.

Test Number	Date	$U_{\text{free}}$ [ $\frac{m}{s}$ ]	$\rho$ [ $\frac{kg}{m^3}$ ]	# of sets	SPC Height [m]	Duration [min : sec]
1	12.01.2017	3.3	195	12	0.145	12:29
2	12.01.2017	3.6	195	11	0.145	16:36
3	12.01.2017	4.8	195	7	0.145	13:03
4	13.01.2017	3.4	85	10	0.135	13:27
5	13.01.2017	3.7	85	3	0.135	19:59

drifting snow events [Hämmerle et al., 2014, Nicholson et al., 2016, Crivelli et al., 2017].

Field experiments using the Kinect were performed on days, on which we expected drifting and blowing snow to occur based on the weather forecast. A pilot test showed that recording with the Kinect did not work in direct sunlight. Therefore each test was performed either after sunset in the evening or night or prior to the sunrise in early morning if sufficient wind and drifting snow did occur.

The two Young wind monitors were mounted 350 cm and 212 cm from the ground. The CSAT3B was mounted 126 cm from the ground in direction East-West. We experienced different issues in the data acquisition with the station. Therefore, SPC Data are only available for the tests 1 to 5. For these tests, the wind speed was calculated using the ultrasonic anemometer. The other tests do only contain Kinect data, no weather- or SPC data. The wind speed for these dates was taken from the operational measurements on the nearby test site.

### Experiments

For tests 1 to 5, the duration of the individual sets was dependent on the conditions. Whenever there was no drifting snow over a period of some tens of seconds, the recording was stopped and a new set was initiated. In contrast to the wind tunnel, the wind speed was not constant. Also the height of the SPC and CSAT3B could not be adjusted after each set. For the evaluation with respect to the SPC and the experiments in the wind tunnel, all sets were averaged over a thirty-second interval such that the integrated particle mass flux could be calculated based on the thirty-second averages (refer to Section 4.2.4). We also calculated the integral time scale for each variable of interest based on the auto correlation function. If the integral time scale was exceeding 30 s, the interval was adjusted to the integral time scale).

### Antarctica

Two weather and drifting-snow stations were constructed 350 m apart close to the Princess Elisabeth Station (PEA)), which is located about 220 km inland in Queen Maud Land at an elevation of 1392 m above sea level (asl) (S 71°57', E 23°21'). The two stations were similar to

## Chapter 4. Spatiotemporal dynamics of short term erosion/deposition in drifting and blowing snow

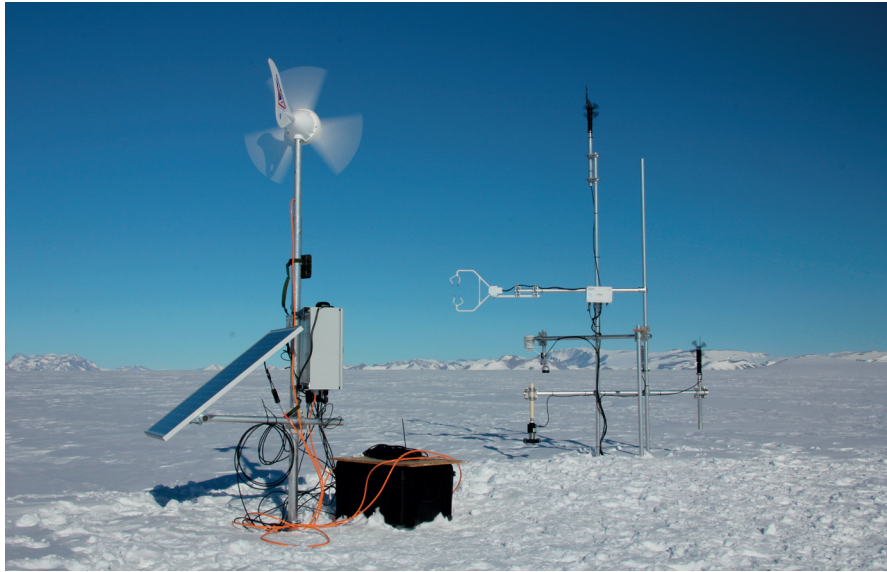


Figure 4.1: One station of two in Antarctica. Masts with electronics and power supply (left) and measurement devices (right) in Antarctica.

the one operated on the Weissfluhjoch. Each station is equipped with the same equipment as on the WFJ excluding the Kinect sensor. The data from PEA include records of drifting particles as well as meteorological data prior, during and after a major snow fall event that was followed by high winds that lead to an event of drifting and blowing snow. Within this period six laser scans were taken (see Tab.4.3). The digital surface models (DSM) of the terrain around the two Antarctic stations were acquired with a Riegl VZ-6000 Terrestrial Laser Scanner (TLS). The scanner was positioned on a tripod on top of a container to increase the field of view and the incidence angle between the laser beam and the terrain. On several occasions between the scans, snow density  $\rho_{snow}$  measurements using a snow penetrometer were performed (see Tab.4.4). The records of the meteorological data in Antarctica faced some issues with continuous recording. Therefore the data contains gaps up to several days in the time series of the different wind speed sensors.

Table 4.3: Dates of the TLS scans in PEA together with the average height change compared to the previous scan.

Scan Number	Date	Day Time	Ave. Snow Height Change [mm]
1	17.12.2016	19:48	
2	23.12.2016	10:16	82
3	25.12.2016	12:25	- 39
4	29.12.2016	11:57	< 1
5	31.12.2016	16:43	- 15
6	11.01.2017	17:21	- 26

Table 4.4: Snow densities as recorded for experiments in PEA

Date	$\rho_{snow} [\frac{kg}{m^3}]$	# of samples
22.12.2016 at 10:00	73	6
22.12.2016 at 17:00	96.8	5
23.12.2016 in the afternoon	113.4	5
27.12.2016	117.3	15
29.12.2016	132	5
31.12.2016	347	7

#### 4.2.3 Kinect mass-flux data

In the wind tunnel, the Kinect device was mounted on the roof of the wind tunnel pointing perpendicularly down to the snow surface. For the field measurements at WFJ, an arm holding the Kinect was mounted on the mast containing the other sensors. The depth images were recorded on a software based on the Kinect Stream Saver application by Dolatabadi et al. [2014]. This allowed recording the Kinect's binary depth images with a frequency of 30 Hz and a resolution of 640 x 480 pixel. At both tests side, wind tunnel and WFJ, the distance between the sensor and the snow was approximately 0.8 m. This led to an area that was covered and evaluated by the Kinect of approximately 0.90 x 0.68 m. At this range, the nominal precision of the Kinect depth sensor is given as 1 mm in the specifications of the instrument. Depending on the distance between the sensor and the snow surface, the resolution of the FOV in the horizontal directions varied due to the fixed pixel numbers. On average, it resulted in a pixel area of approximately 0.3 mm<sup>2</sup>.

As in Crivelli et al. [2017], the filtering of the raw Kinect data was done in post-processing. The Kinects's depth time series were downsampled in time for each pixel from 30 Hz to 1 Hz using a Savitzky-Golay moving average filter (MATLAB's *sgolayfilt* function). Besides the moving average temporal filter, we added a spatial 2D adaptive noise removal filter (MATLAB's *wiener2* function) to address the characteristic noise visible in the raw data that was introduced by the IR pattern of the Kinect device itself. The depth data were further processed based on the procedure already adopted by Crivelli et al. [2017] to receive the surface mass flux time series for each pixel. Based on that, average surface mass flux over a specific area could be calculated.

For the spatial analysis, the FOV was divided in subgrids (SG). We defined a sub grid size of 15x4 sub grid cells, which averaged approx. 0.0105 m<sup>2</sup> per grid cell.

#### 4.2.4 SPC mass-flux computation

The SPC measures the saltation mass flux on a small volume at a single location in the saltation layer based on the particles that pass through the control volume. The computation of the SPC's mass flux is performed by summing up all the particles for each bin, multiplying this

## Chapter 4. Spatiotemporal dynamics of short term erosion/deposition in drifting and blowing snow

---

number with the estimated particle diameter of the particular bin and divide this value by the area of the control volume perpendicular to the streamwise direction as well as the sampling time.

In order to estimate the total saltation mass flux we integrated the mass flux over the height of the saltation layer in the same way as it was presented in Crivelli et al. [2017]. In contrast to the wind tunnel measurements, in the field, using the profile function by Kawamura [1948, 1951] and Dong and Qian [2007] proofed to be not very robust. Using this function resulted in unrealistically high mass fluxes near the surface high for cases with very low friction velocities. Therefore we investigated alternative formulations to represent the mass flux profile.

### Exponential profile function

Following Crivelli et al. [2017] the particle mass flux profile is expressed as an exponential decay:

$$q_P(z) = q_0 \cdot e^{-\frac{\lambda g}{u_*^2} (z-h_0)}, \quad (4.1)$$

with  $q_0$  equals the average SPC mass flux of the time series at the point measurement and  $h_0$  equals the height the SPC measurement location above the snow surface. For the field studies,  $q_0$  was taken as the mean mass flux value for the averaged set. As discussed in the previous section, for experiments conducted at the WFJ a set corresponds to 30 second averages.

The term in the exponent is referred to literature as length scale of the saltation system  $L = \frac{u_*^2}{\lambda g}$  [m] [Guala et al., 2008] with  $u_*$  representing the friction velocity,  $\lambda$  a constant parameter that defines  $L$  and  $g$  the gravitational constant. For the wind tunnel, Crivelli et al. [2017] revealed that for the comparison with the surface mass flux,  $\lambda = 1$  best represented the particle mass flux.

To calculate  $u_*$  we used the law-of-the-wall

$$u_* = \frac{\kappa u(z)}{\ln(z/z_0)}, \quad (4.2)$$

with  $\kappa = 0.4$ ,  $u(z)$  the freestream velocity at the sensor height and  $z_0 = 2.4 \cdot 10^{-4}$  m in the wind tunnel [Gromke et al., 2011],  $z_0 = 0.01$  m at WFJ [Doorschot et al., 2004] and  $z_0 = 3.5 \cdot 10^{-3}$  m in PEA [Amory et al., 2017].

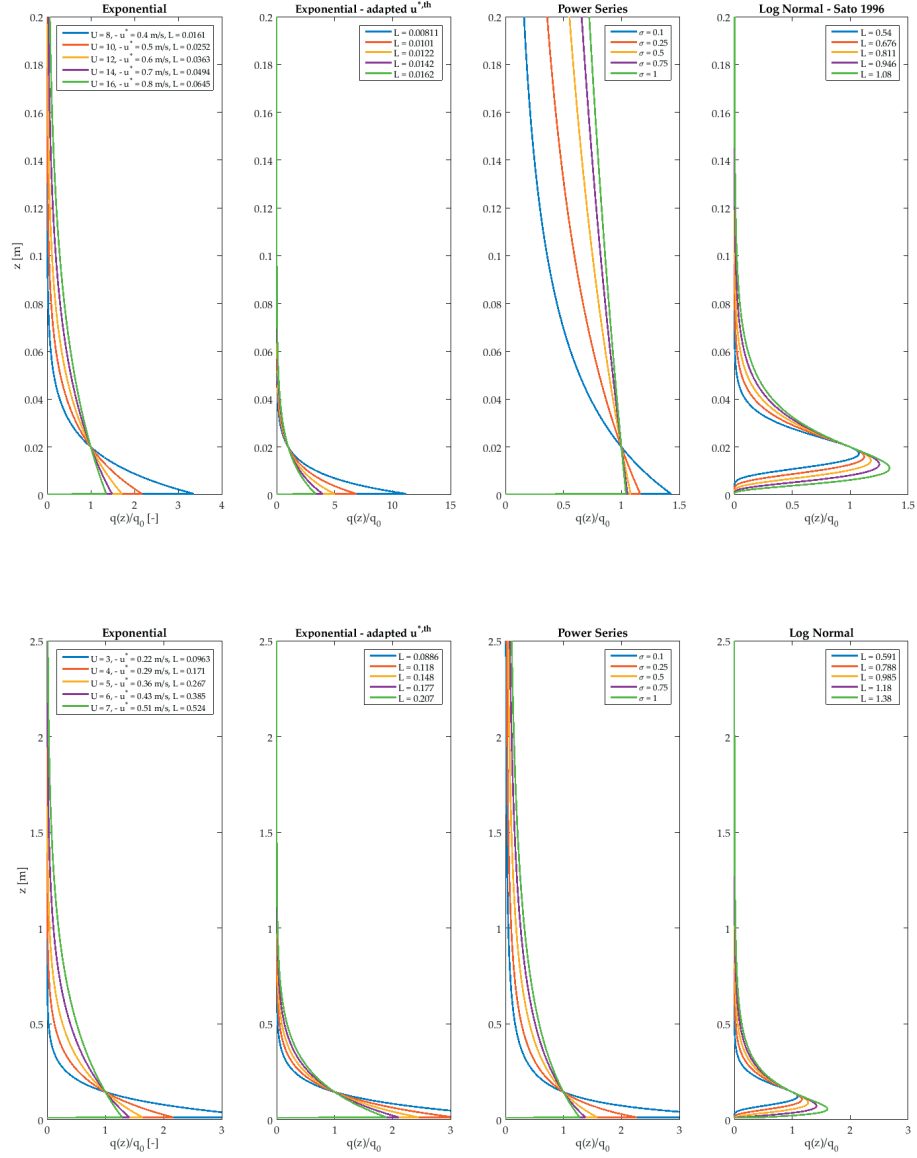


Figure 4.2: The four profile functions for typical mass flux conditions in the wind tunnel on top and at the drift station in the field at the bottom. The threshold friction velocity was set to be 0.2 m/s.

### Exponential profile function using threshold friction velocity

The first alternative was a slight adaptation in the representation of the length scale of the saltation system. Instead of using the friction velocity in square, we used the threshold

## Chapter 4. Spatiotemporal dynamics of short term erosion/deposition in drifting and blowing snow

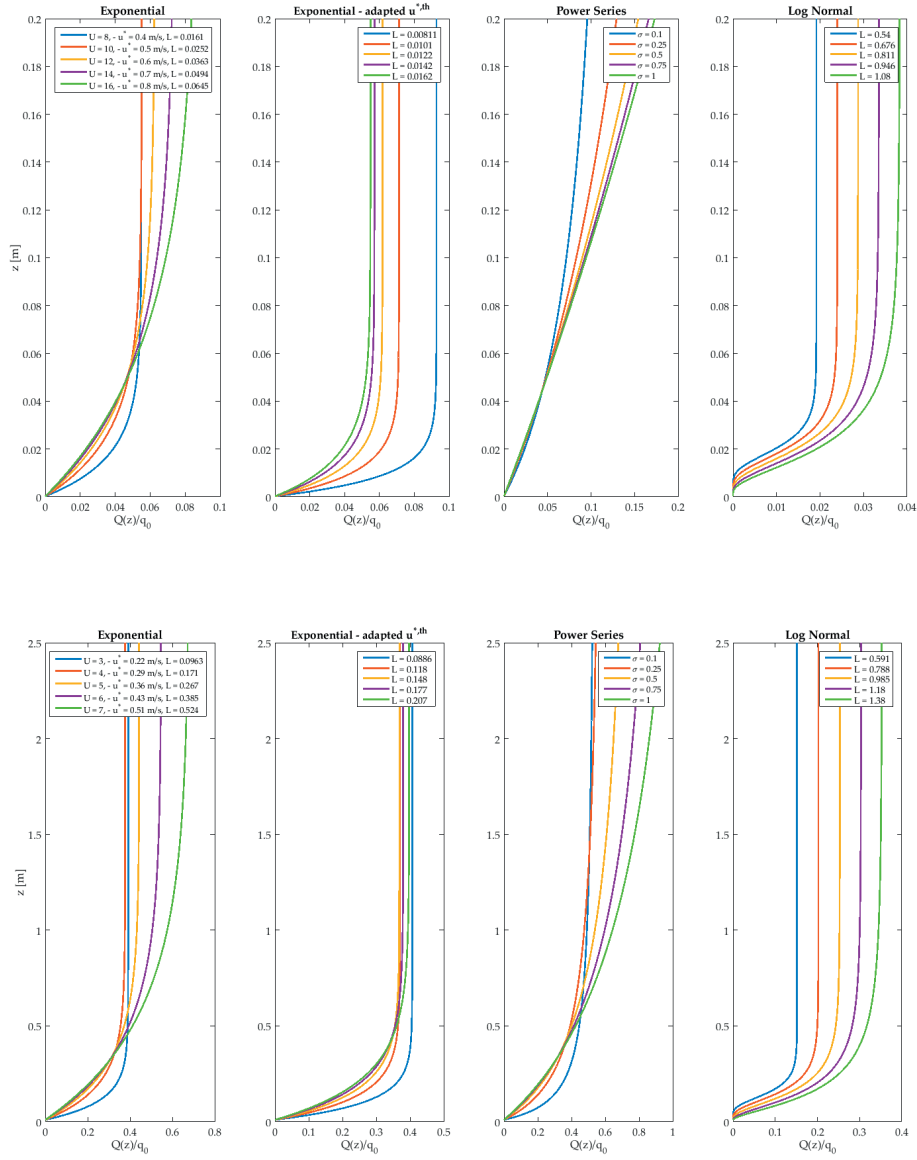


Figure 4.3: The integrated total particle mass flux as a function of the boundary layer height for typical mass flux conditions in the wind tunnel on top and at the drift station in the field at the bottom. The threshold friction velocity was set to be 0.2 m/s.

friction velocity multiplied by the friction velocity resulting in

$$q_P(z) = q_0 \cdot e^{-\frac{\lambda g}{u_* u_{*,th}} (z-h_0)}. \quad (4.3)$$



Using the threshold friction velocity was intended to improve the robustness of the profile function towards low friction velocities by limiting the cases between starting drift and drift at high friction velocity.

### Profile function using a power series

The second alternative was adapted after Stout and Zobeck [1997] resulting in

$$q_P(z) = a \cdot \left(1 + \frac{z}{\sigma}\right)^{-2}, \quad (4.4)$$

with  $a = q_0(1 + \frac{h_0}{\sigma})^2$  and  $\sigma$  a constant parameter. This representation resembled a power series that did not include the friction velocity of similar physical variables. The advantage of this profile function is that it is easy applicable and does not need additional measurements.

### Profile function using a log-normal distribution

For the third alternative we adapted a log normal function. In literature, log-normal functions were traditionally used for the description of the particle diameters [Budd, 1966]. Looking at the profile function, the log-normal distribution together with the threshold friction velocity resulting in

$$q_P(z) = \frac{a}{z} \cdot e^{-\left[\frac{\lambda g}{u_{*s}^2 / u_{*s,th}} (\log z - \log h_0)\right]^2}, \quad (4.5)$$

with  $a = q_0 h_0$ . The advantage of the log-normal distribution is that it accounts for lower wind speeds close to the surface. For a rough surface, it is clear that the flux must decrease when approaching the ground. In between the roughness elements, the horizontal flux will be reduced and must go back to zero at a certain level. This argument supports the form of a log-normal flux density profile. Furthermore, the log-normal distribution accounted for increased wind speeds by flattening the distribution at heights above  $h_0$ . This leads to a more realistic distribution in the upper saltation layer at high wind speeds.

In order to evaluate a potential 'best-practice' profile function, we show the four functions for wind tunnel conditions as well as for field conditions (see Fig.4.2) for different wind speeds resulting in different friction velocities (see values reported in the figures legend).

For the comparison to the surface mass flux, the particle mass flux had to be considered as a total mass in the boundary layer. The vertical expansion of the saltation layer was assumed to have a maximal height of  $z_{SL} = 2.5$  m in the field (PEA and WFJ) and 0.2 m in the wind tunnel. In the wind tunnel, the height was determined by experiments (particularly [Gromke et al., 2014]).

In the field, using a profile function as presented in Equation 4.5 revealed that the differences

## Chapter 4. Spatiotemporal dynamics of short term erosion/deposition in drifting and blowing snow

---

at heights larger than 2.5 m were just marginal. For numerical modeling of saltation, Shao and Li [1999] used a saltation layer height of 2 m.

For the estimation of the total particle mass flux  $q_P$  is integrated over the total height from  $z = z_0$  to  $z = z_{SL}$ ,

$$Q_P = \int_{z_0}^{z_{SL}} q_P(z) dz. \quad (4.6)$$

In the same way as for the profile functions, Fig.4.3 shows the total particle mass flux integrated for different heights of the boundary layer. As previously mentioned, the differences become marginal with increasing height of the boundary layer, except for the case of the power series. The results in Fig.4.3 show that this profile function seems not to be reasonable.

Since we did not have the possibility to record a second SPC mass flux signal at a different height, we can compare the function only to visual inspections of drifting and blowing snow. Considering the four profile functions, the log-normal distribution arguably presents the most realistic mass flux. From all the functions, only the log-normal function does not over estimate the mass flux towards the snow surface. Also the function is becoming flatter in the upper part of the saltation layer with increasing friction velocities, meaning that for high wind speeds, the mass flux is more distributed through the saltation layer and more confined to the surface at lower wind speeds which is qualitatively correct.

The shape of the profile function is defined by the term in the exponent which is referred as the length scale of the saltation  $L = \frac{u_*^2 / u_{*,th}}{\lambda g}$ . Together with the law of the wall (Eq.4.2),  $\lambda$  is the only term to tune the profile function. Since the shape of the profile function is supposed to have the same shape, independently of field or wind tunnel and therefore of the height of the saltation layer, we propose an expression for  $\lambda$  as a function of  $u_{*,th}$  and the SPC height. Based on the shape of the profile function, we suggest that at the threshold wind speed of the onset of saltation,  $L_{th} = 0.55$  m. Therefore the expression for the variable  $\lambda$  becomes

$$\lambda = \frac{u_{*,th}}{L_{th} \cdot g} \quad (4.7)$$

with  $u_{*,th}$  calculated based on Eq.4.2 at the wind speed at the onset of saltation. In comparison to Eq.4.1, the term  $u_*^2 / u_{*,th}$  was chosen such that in the case of a low  $u_{*,th}$ ,  $\lambda$  is still guaranteed to create a reasonable shape of the profile function.

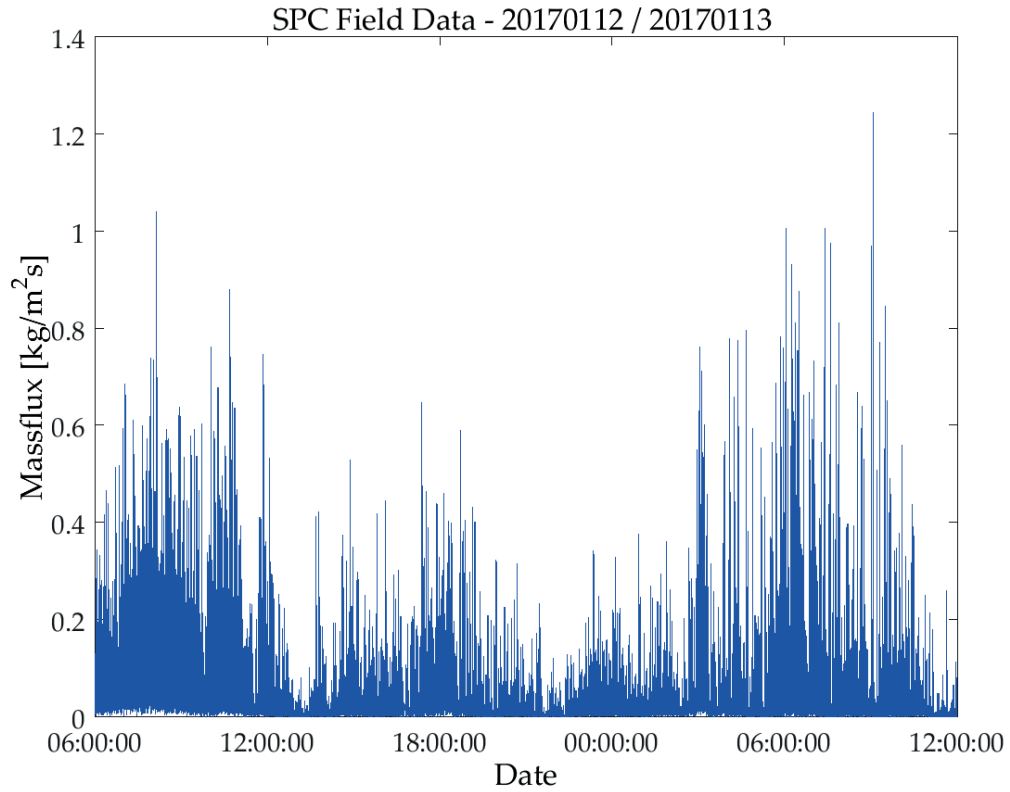


Figure 4.4: Record of the SPC Data on WFJ test site.

## 4.3 Results and Discussion

### Weissfluhjoch

Summarized in Table 4.2, the readers find the environmental conditions for the different tests. Figure 4.4 shows the time series of the particle mass flux. The SPC sensor was mounted on a height of 14 cm prior to each test day.

For the tests at WFJ, by using the Kinect sensor, a sufficient temporal resolution to characterize the erosion/deposition dynamics could be achieved. Figures 4.6 and 4.7 show histograms and the averaged surface mass flux for tests 1 to 5 (ref. Tab.4.2) during the storm occurring between 2017.01.12. and 2017.01.13. The histogram approximates a normal distribution. This may be due to the filtering in the post processing of the Kinect data or the small area investigated. The temporal dynamics of the snow surface height during the experiment is displayed in Figure 4.8. Test 1 had the most significant change in surface height. Except for a slight artifact in the beginning of the measurement, during test 1, the snow was overall mostly deposited. Test 2 (which was recorded one hour later at the same location) has more erosion than deposition. Inspection of the time series displays that a large deposition in the beginning was followed by more erosion. Later on the same day, in test 3, there was deposition again, albeit slightly

## Chapter 4. Spatiotemporal dynamics of short term erosion/deposition in drifting and blowing snow

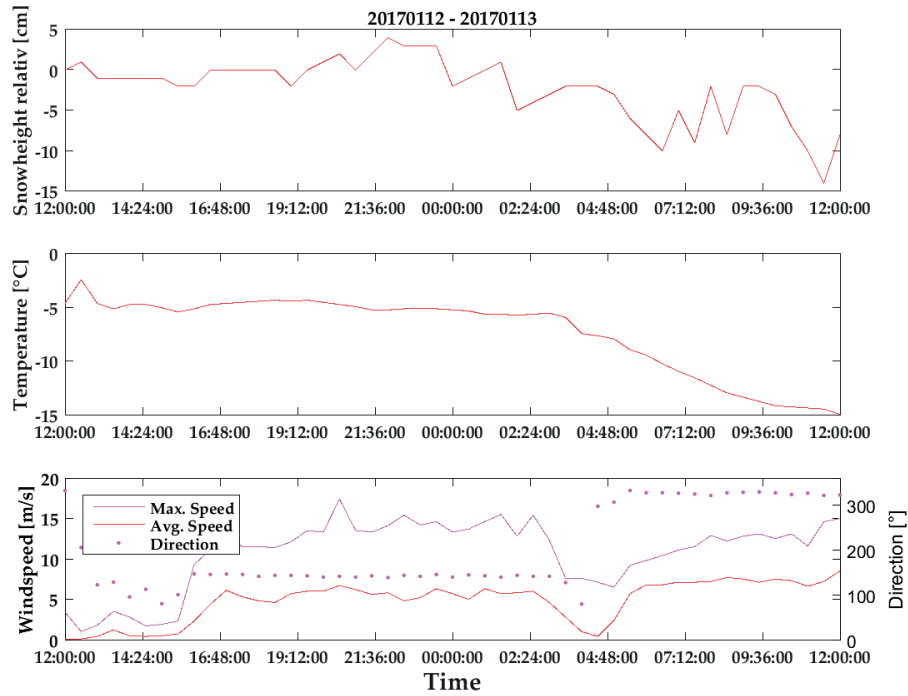


Figure 4.5: Time series for snow height, temperature and wind/direction on WFJ.

less than during test 1. The meteorological data (Fig.4.5) and the SPC record (Fig.4.4) show that during the night the wind direction changed without significantly decreasing particle saltation.

Unlike the particle mass flux which remained in the same range during the entire time, the surface mass flux did not vary much anymore from test day 3 on. Neither the absolute surface height change for the entire FOV (Fig.4.8) or for the subgrids (Fig.4.9) nor the mass flux as visible by the mesh in Figure 4.7 show large amplitudes of the surface change. In Figure 4.7 at Position X, the surface mass flux increases from left to right ( $X_2$  to  $X_{14} = 0.745$  m), at Position Y from bottom to the top ( $Y_1$  to  $Y_3 = 0.340$  m). In the case for tests 1 to 3, the wind was blowing from right to left. For all tests, the variability in Y direction is small, while it is larger in X direction, which corresponds to the streamwise direction. In test 1, the surface rises first on the luv-side, a few minutes later the middle of the area is rising and another few minutes later, the rise reaches the lee-ward side.

Since in our case, we have deposition only, according Kobayashi and Ishida [1979] one could speculate that this movement reveals the formation of a barchan structure. Later on in test 2, we find erosion on the luv-side and deposition in the lee-side. This again could be due to a barchan dune or since we are in a erosion/deposition scenario also to a snow dune. Compared to the data from PEA, the spatial coverage is too small to distinguish the exact case. Since the test were recorded in an event of high drifting and blowing snow during the night, no other

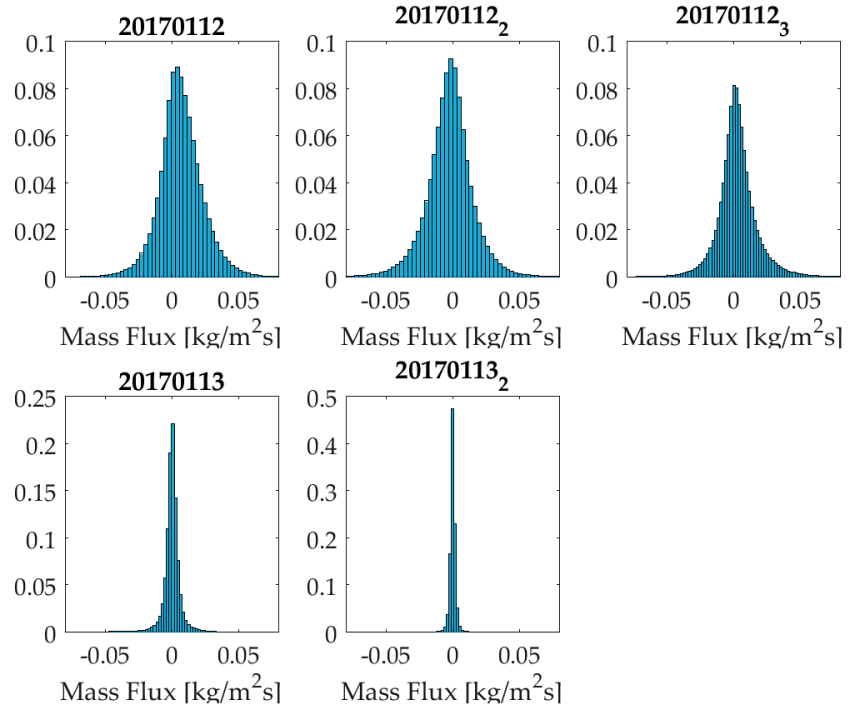


Figure 4.6: Histogram of the average surface mass flux from test 1 to 5 on WFJ.

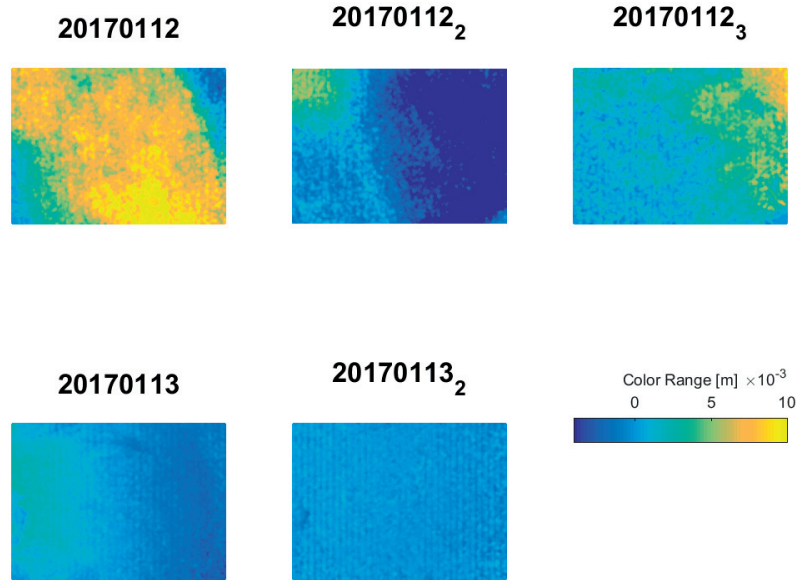


Figure 4.7: Plot of the average surface mass flux from test 1 to 5 on WFJ.

## Chapter 4. Spatiotemporal dynamics of short term erosion/deposition in drifting and blowing snow

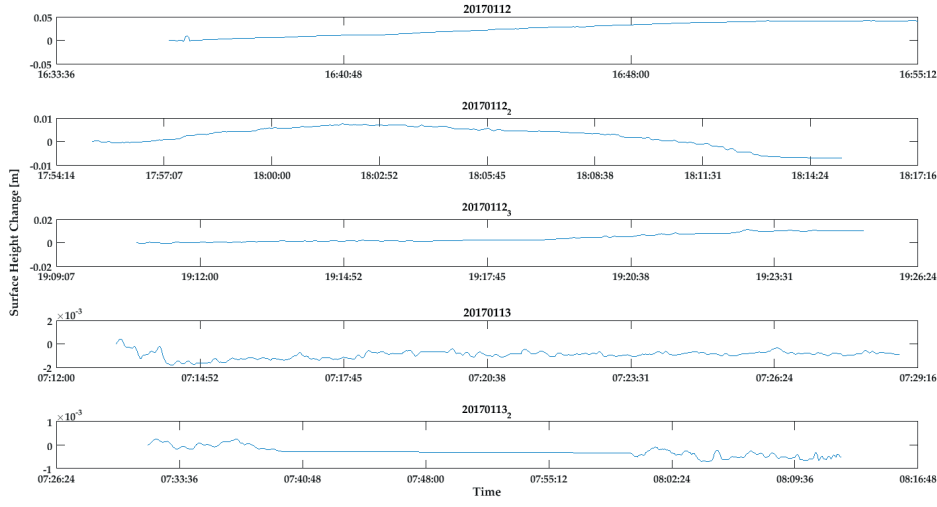


Figure 4.8: Time series for snow height for test 1 to 5 for the whole FOV of the Kinect.

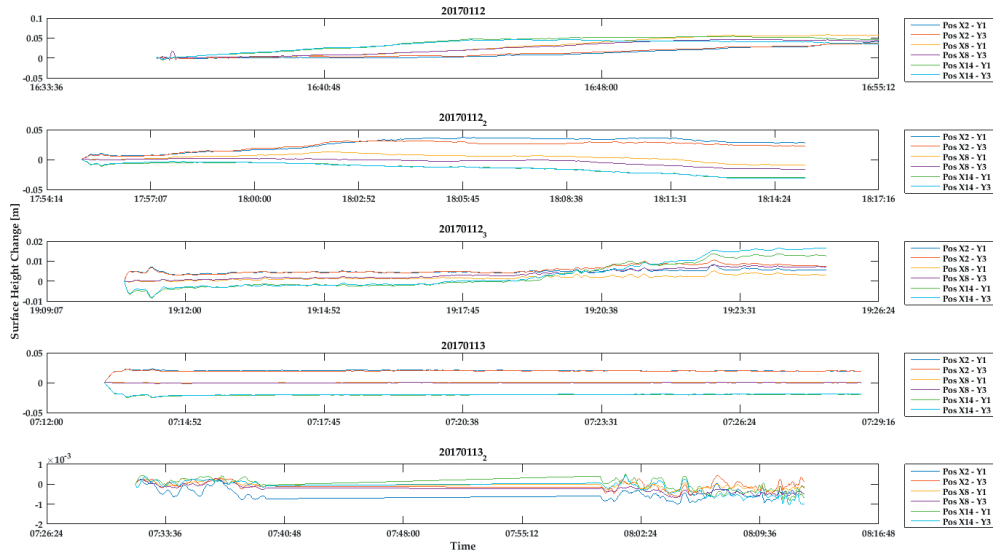


Figure 4.9: Time series for snow height for test 1 to 5 for different positions of the Kinect's sub grid.

Table 4.5: Table with all the correlation values between  $Q_S$  and  $Q_P$  for the test on WFJ over the entire FOV as well as for the 15x4 subgrid scale.

	1	2	3	4	5
All Correlation	0.301	0.210	0.157	0.072	0.031
SG Correlation	0.276	0.468*	0.445*	0.404*	0.221

evidence could be recorded to support this speculation.

### Comparison to Wind tunnel data

As mentioned, the surface change recorded for the WFJ measurements allowed a high temporal resolution. Applying the integration according Eq.4.6 was possible, although as opposed to the wind tunnel, a quantitative analysis of the boundary layer height and the approximate saltation length was not possible based on the given data, but since these parameters were considered constants in our calculations, they did not significantly influence the correlation between the  $Q_S$  and  $Q_P$ . For the comparison, we down-sampled the time series with a 30 second moving average. Unlike for the high correlation reported in Crivelli et al. [2017] a comparison of the particle mass-flux in Fig.4.4 and the total surface mass flux in Fig.4.7 reports a very low correlation ( $r = -0.301$ ). Even when considering the correlation on the sub grid scale, the overall correlation is never higher than  $r = -0.468^*$  (see Tab.4.5).

In the wind tunnel, results presented by Paterna et al. [2016] show a decoupling of the particle mass flux and the turbulence. Therefore we analyzed the data to see if the same decoupling may occur in the field as well. The SPC did not deliver the same details as the study mentioned above, nevertheless it was interesting to see how the scales in average and the variability of the mass flux did compare between the two. Figures 4.10, 4.11 and 4.12 show a comparison between data recorded in the wind tunnel and data from WFJ.

In Figure 4.10 a box plot for the surface mass flux recorded with the Kinect, the particle mass flux recorded with SPC and the shear stress velocity based on the ultrasonic anemometer is presented. For this comparison, we relied on the set average mass fluxes or the shear stress velocity for the wind tunnel and to the 30 seconds average for the field measurements. Most interestingly, the range of the surface mass fluxes as well as the particle mass flux, is very similar. Considering the wind-tunnel experiments, the mean values are slightly higher in measurements conducted with increasing wind speeds. In the case of the surface mass flux, the set averages for the wind tunnel are dominated by erosion. In the case of the 30 seconds averages for the drift station, there was slightly more deposition on average. The SPC ranges are very similar. This result is very interesting since in the case of the wind tunnel, the SPC sensor was always adjusted to be 2 cm above the snow surface before each set. At the drift station at the WFJ, the sensor was mounted between 13.5 cm and 14.5 cm above the snow surface prior to each experiment. This height strongly influenced the integration of the particle

## Chapter 4. Spatiotemporal dynamics of short term erosion/deposition in drifting and blowing snow

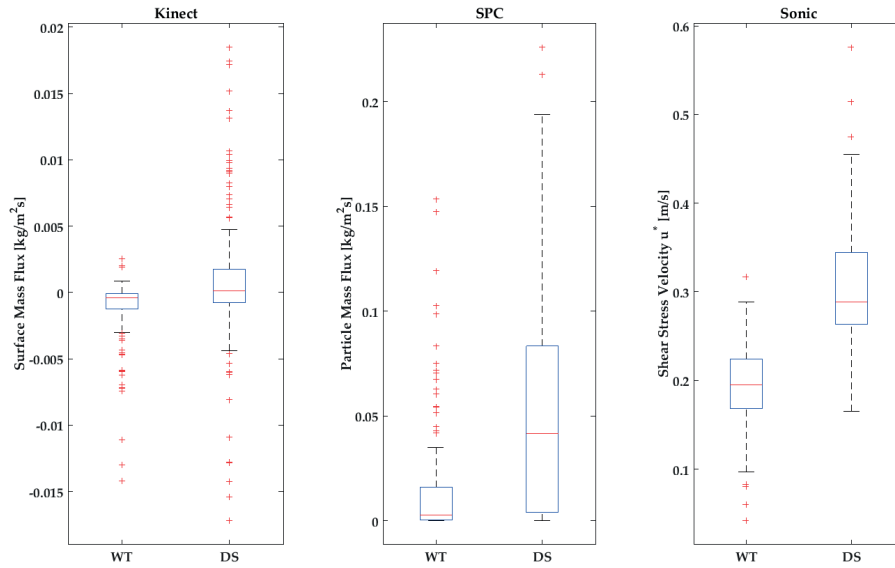


Figure 4.10: Box plot for the the mass flux and the shear velocity for the DS and WT.

mass flux according Crivelli et al. [2017] based on the theoretical saltation profile (refer to Kawamura [1948], Guala et al. [2008]). One main difference between the drift station and the wind tunnel is also the range of the shear stress velocity which is much larger in the field than in the wind tunnel, which does not surprise since the dimensions and conditions of the boundary layer are not well comparable. Nevertheless, they give an estimation about the mass entrained and transported in the saltation layer.

The boxplot in Fig.4.11 shows the statistics for all sets in the wind tunnel and the 30 s averages of WFJ. In contrast to the data in the previous plot (Fig.4.10), the data for this boxplot represents the time averaged mass flux at each pixel rather than over the entire FOV, therefore the distribution is much wider. The first difference is that the mean surface mass flux in the field is nearly symmetrically spread around zero, with an even distribution between erosion and deposition, suggesting that the surface mass flux is in equilibrium. The wind tunnel data, as discussed by Crivelli et al. [2017], reflect the prevalence of erosion over deposition. The uneven distribution around the mean is strongly influenced by the test routine of steps with increasing wind speeds. This behavior is also reflected by the resulting statistics. The field data has less variability compared to the data of the wind tunnel. Interestingly the skewness is distributed symmetrically around zero for both experimental setups.

The ranges for of the particle mass flux recorded with the SPC are a in a similar range, despite the fact that the height of the SPC is much higher in the field. Therefore one can follow the absolute mass flux at WFJ is larger than in the wind tunnel based. As for the SPC measurements, the surface mass flux values recorded in the field are in a similar range as for the records in the wind tunnel. Unlike the SPC measurements, where significant differences in the position



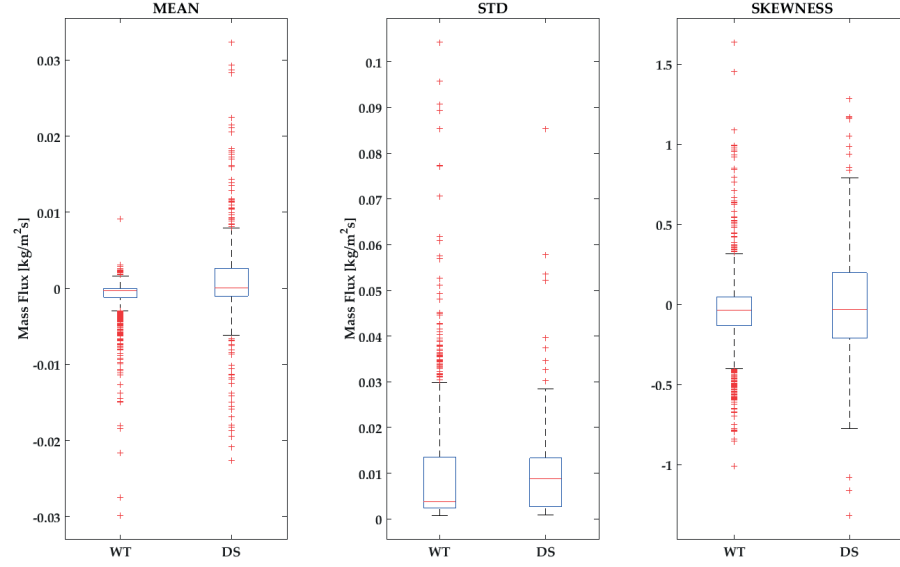


Figure 4.11: Comparison of the histograms for the Kinect mass flux between drift station (DS) and wind tunnel (WT).

Table 4.6: Table with all the correlation values between  $Q_S$  and  $Q_P$  for the test in the wind tunnel over the entire FOV.

	1	2	3	4	5	6	7	8	9	10	11	12
All Correlation	-0.961	-0.898	-0.933	-0.950	-0.581	-0.795	-0.752	-0.791	-0.681	-0.848	-0.819	-0.994

above the snow surface exist, the measurement routines in the wind tunnel are very much similar to the ones in the field. Differences in the relative partition between erosion and deposition are believed to be based on the design of the wind tunnel and on the measurement conditions (i.e. wind speed). As discussed above, the goal was to investigate how well wind tunnel measurements do represent the mass flux in the field and vice versa. Since particle mass flux and surface mass flux are within a similar range in terms of average values and variability, we were interested in the temporal variability. Figure 4.12 shows the differences for the integral time scales for all relevant measurement techniques (Kinect, SPC and Sonic). Looking at the time scales, one finds that Kinect and SPC measurements again fall within the same range. Only the integral time scale of the wind flow measurements shows a significant difference. For the flow in the wind tunnel, the integral time scale is near the sampling frequency. As observed for the differences in shear stress between drift station and wind tunnel (Fig 4.10) we find for the WFJ data, the integral time scale is much larger (median at approx. 4 seconds) and resembles much more the scales of the mass flux. For the field, this doesn't confirm the results in Paterna et al. [2016], that the mass flux is able to decouple itself from the turbulent structure of the flow.

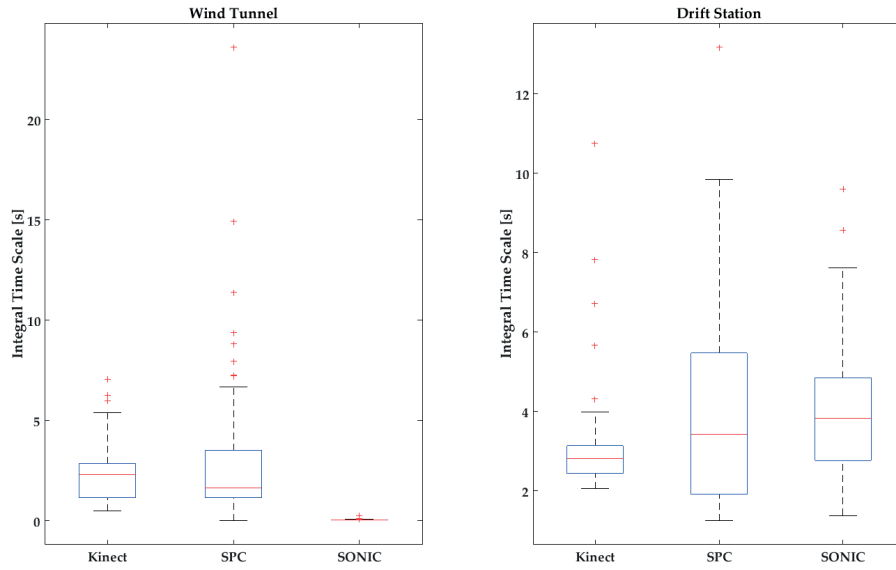


Figure 4.12: Box plot with the integral time scales for Kinect mass flux, SPC mass flux and Sonic, both at DS and WT.

### Antarctica

Measurements of wind tunnel erosion fluxes have shown that SPC flux measurements at one height can be used to estimate total horizontal flux based on an assumed vertical profile. The measurements from WFJ clearly show that horizontal mass flux is not strongly related to local changes in average snow deposition or erosion. In the same way, applying the integration according Eq.4.6 to the data from the two SPC in Antarctica revealed to be difficult to interpret with respect to the change of snow volume. Due to the long intervals between the scans, a distinction between how much snow was eroded (as for wind tunnel experiments [Crivelli et al., 2017]) and how much of the change in volume is due to settlement and sintering of the snow could not be addressed. Nevertheless the experiment serves as an estimation how much snow was transported during this storm event.

Table 4.7 summarizes the snow surface height changes as well as the integrated particle mass flux for both stations between consecutive scans. The date from these surface height changes is also also displayed with a histogram over the whole surface (Fig. 4.13) as well the height change on the grid of the laser scans (Fig. 4.14). For the interpretation of these changes, additional data for the particle mass flux respectively for snow height, temperature and wind are given in Figs. 4.15 and 4.16.

In the following, we interpret these events individually:

- **Scan 1 to scan 2:** We find three days with significant drifting events at relative low wind

### 4.3. Results and Discussion

Table 4.7: Result from TLS scans volume change from PEA. The parameter *VolumeGain* represents the positive values of histogram.  $Q_P SPC_i$  represents the integrated total particle mass flux from the two stations.

Scan: From - To	Duration [d]	Total Area [m <sup>2</sup> ]	Volume Change [m <sup>3</sup> ]	Mean dZ [m]	$\rho_{snow}$ [kg m <sup>-3</sup> ]	$U_{free,th}$ [m s <sup>-1</sup> ]	Mass Flux per Day [kg m <sup>-2</sup> d <sup>-1</sup> ]	Volume Gain [%]	$Q_P SPC_1$ [kg m <sup>-1</sup> d <sup>-1</sup> ]	$Q_P SPC_2$ [kg m <sup>-1</sup> d <sup>-1</sup> ]
1 - 2	5.6	86755	7150.8	0.082	73	0.6	1.074	92	1.890	3.0759
2 - 3	4.1	120809.5	-4662.3	-0.039	115	3.5	-1.082	0	0.003	0.013
3 - 4	2	111612.25	94.2	0.001	125	10	0.053	60	0	0.035
4 - 5	2.2	93734.25	-1406.3	-0.015	250	6	-1.705	23	10.624	5.110
5 - 6	12	96147.75	-2645.8	-0.028	347	2.25	-0.796	4	-	-

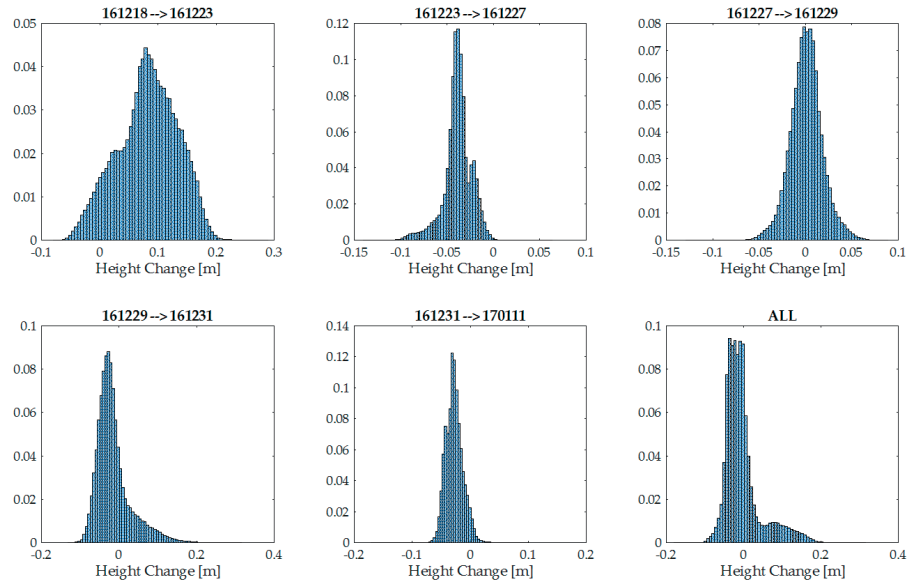


Figure 4.13: Histogram of the surface height change proportion between the scans.

## Chapter 4. Spatiotemporal dynamics of short term erosion/deposition in drifting and blowing snow

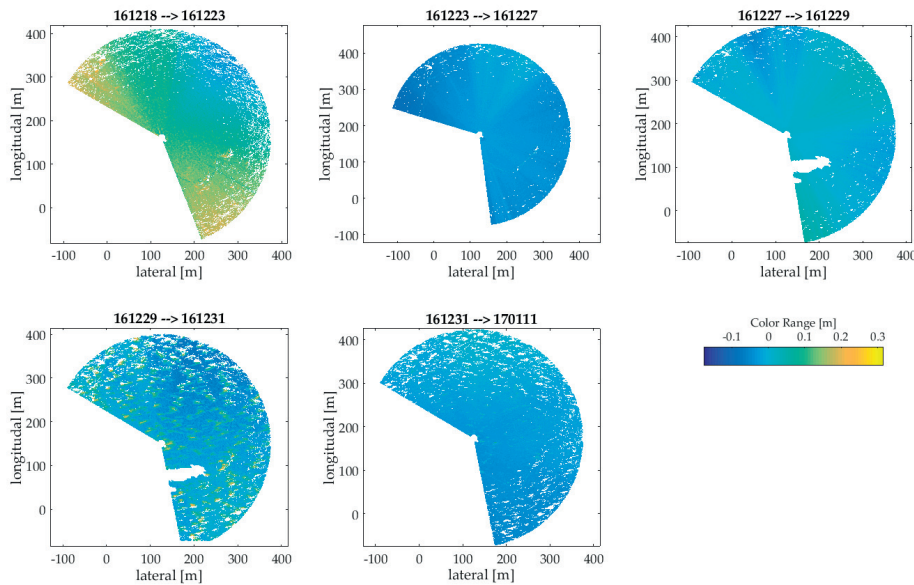


Figure 4.14: Plot of the surface height change between the scans.

speeds (see Fig.4.15). Based on the snow height measurement at the stations (Fig.4.16), during this time, the snow surface was just slightly eroding. At the end of the period, a significant snow fall event took place. This snow fall is accompanied/associated by/with a large increase in volume (see Tab. 4.7). The uneven texture visible in the plot of the surface change (Fig.4.14 - top left) reveals a change in the surface structure. The precedent surface roughness was smoothed by the snow fall. Looking at the integrated particle mass flux, both stations recorded a significant amount of drifting snow.

- **Scan 2 to scan 3:** Scan 3 is the first scan shortly after the snow fall. Between the snow fall and the scan, no significant drifting was visible in the SPC signals. The time series of the snow height shows a significant reduction of snow surface height after the snow fall event. Table 4.4 shows that the decrease in snow height is accompanied by an increase of snow density. The decrease in snow height is due to the settlement and sintering of the snow that leads to the observed increase of snow density. The volume reduces significantly and sintering is assumed to occur such that particles on the surface are less easily entrained by the wind due to stronger bonding with neighboring particles. In this period, few, small and short drifting events took place which didn't result in a significant particle mass flux. In this time, the changes in the snow surface structure based on the difference between the scans is not very pronounced (top-middle of Fig.4.14).
- **Scan 3 to scan 4:** This period has no significant change in neither volume nor mass. There are again a few short drifting events with winds from southern directions, resulting in little (or no) particle mass flux. The surface change was in equilibrium (Deposition 60%/ Erosion 40%). Also the snow surface did not see much more settlement.

- **Scan 4 to scan 5:** In this period a major storm hit the test site. This is well visible in the particle mass flux (see Fig.4.15) with high particle mass flux over a period of more than one day resulting in a considerable amount of particle mass transport, particularly at station 1. Table 4.7 shows a major decrease in snow height over a relative short period. Comparing to previous decreases in snow height which were assumed to be driven by sintering and settlement of the snow, this decrease is supposed to be dominated by erosion. Despite the dominating decrease in average snow height, a large amount of snow was deposited on both stations (refer to the snow height change at the stations (Fig.4.16, top)). Also the temperature record during the storm did not follow the mean daily pattern. The wind direction was relatively constant from south-east. The average wind speed exceeded 10 m/s. Table 4.7 shows a major change in snow volume during this short period. The percentage of erosion/deposition and even more the surface change plot (Fig.4.14 - lower left) show a major change in the snow surface structure. The plot reveals the formation of barchan dunes over the whole area. Very interesting is the shape of the histogram (Fig.4.13 - lower left). It shows a sharp decrease for the erosion and a much smoother decrease on the deposition side. We assume that the layer of snow which remained from the snow fall in the period between scan 1 and 2 was eroded down to the old, hard surface prior to the snow fall event. The deposition of the eroded snow on the other hand was much smoother. After the storm, the snow had a significantly higher density. This opens the question of how much of height change is based on erosion/deposition and how much of the change was due to the settlement.
- **Scan 5 to scan 6:** This is again a relatively long period. Fig.4.16 reveals a slight reduction of the snow surface height as well as some events with strong winds from various directions. These wind events were accompanied by snow drift events (Fig.4.15). Although the wind speed is quite high in certain events, the drift events are rather small. We assume that the surface reduction is based mostly on further settlement/sintering or sublimation processes, since the changes are quiet uniform throughout the entire area in the scans. Also the sum of events with drifting snow may have led to erosion of the barchans and smoothed the surface on a larger scale. This is represented to some extent in the last plot of Fig.4.14, where close to the former barchan dunes, spots with less erosion/settlement occur, suggesting that some snow was deposited at these places. Based on the small changes over the period of these two scans, it shows that the dunes did not move significantly into a certain direction. It is worth mentioning again that this is a relatively long period and a proper estimations of these changes is difficult.

## 4.4 Conclusions

The topic of this study was to compare the spatial and temporal variability of snow surface erosion and deposition recorded from field studies to controlled experiments in a wind tunnel. Analyzing the data in a spatial context shows that the surface mass flux is very variable in a small spatial domain. The data from Princess Elizabeth in Antarctica shows the formation

## Chapter 4. Spatiotemporal dynamics of short term erosion/deposition in drifting and blowing snow

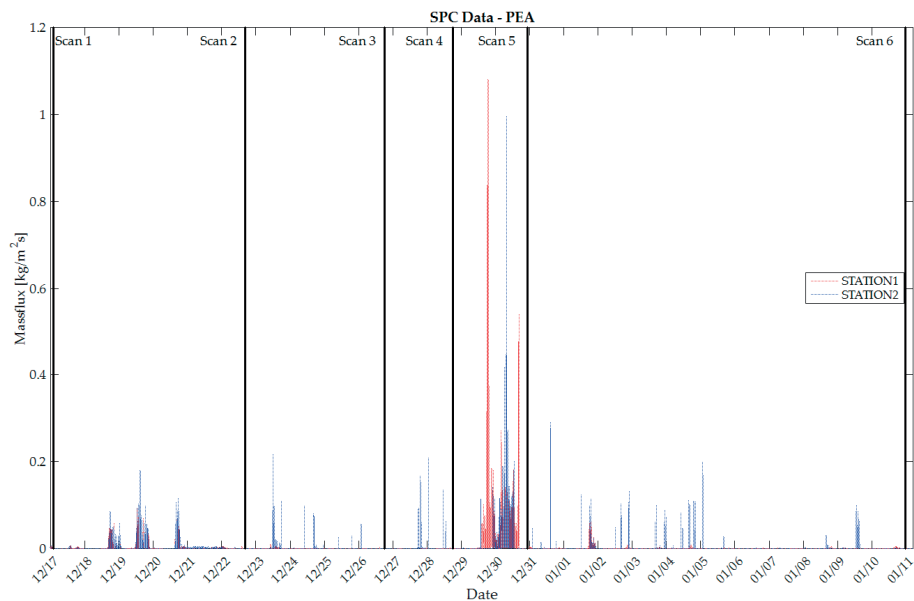


Figure 4.15: Time series of particle mass flux from two stations. The black lines show the time when the scans were done.

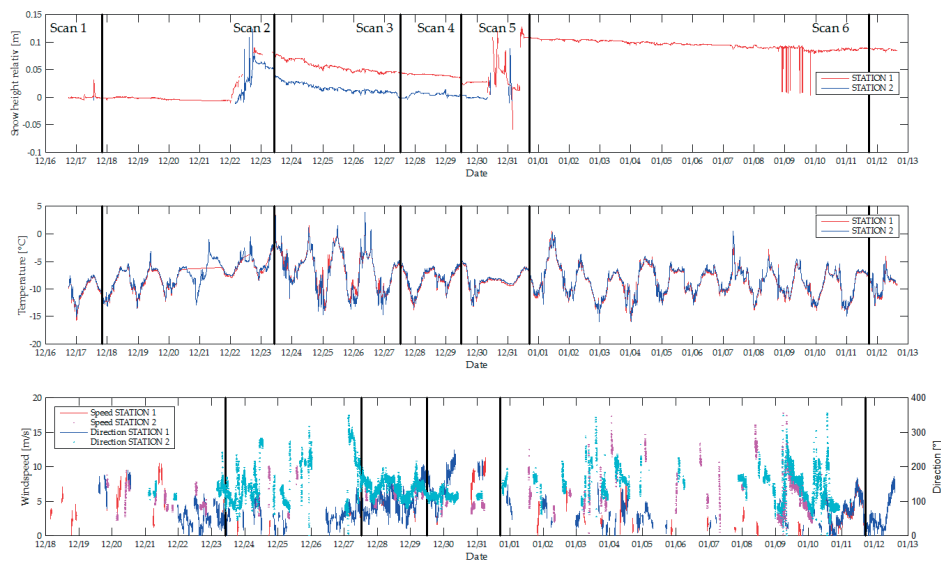


Figure 4.16: Time series of snow height, temperature and wind/direction for both stations.

of a homogeneous distributed pattern of barchan dunes during a storm, but due to the relatively long intervals between the TLS scans, they fail to reveal other small scale changes. Results of the snow surface change from an alpine test site suggests that the evolution of the snow surface has a strong variability in streamwise direction, possibly due to the formation and traversing of snow wave structures, while reduced variability is observed in cross-wise direction. Unfortunately the data lacks of a large enough area to capture entire snow-wave structures.

In terms of temporal dynamics, the data from Antarctica (PEA) suggests that settling and sintering of the snow has a main influence on the changes of the snow volume. These processes seem not affect the characteristics of the surface structure a lot on a small scale, but the total change in volume is significant. In our data from PEA, only the recorded storm event did significantly change the snow surface structure. Although there were events of drifting snow before and after the storm, either the scans were temporarily too distant from each other to reveal enough details, or the drifting was not strong enough to alter the snow surface. The lack of significant snow surface alteration after the storm may be explained by considering that the drifting event did alter the snow surface in such a way, that the structure withstands further changes even with continuing events of drifting particles. This may suggest that the snow exposed to significant drifting does not allow changes in the snow surface as easily anymore. Unfortunately there were no other storms afterwards to proof this hypothesis for the recorded surface in PEA. This hypothesis goes along with the results of Aksamit and Pomeroy [2016], who reported the mass transport to be much dependent on the snow surface hardness. This also agrees with the results of Groot Zwaafink et al. [2013], where they stated that drifting snow is not necessarily deposited on the surface but keeps moving. In our case we argue that the effect of drifting snow on the snow surface is inversely related to the exposition of the snow surface to drifting particles, meaning that the potential of the surface to be eroded decreases with time of continuing exposure to drifting particles independent of the saltation strength. The data recorded with the Kinect confirms this hypothesis. While in the first tests, the snow surface changes continuously, in the subsequent measurement, as the magnitude of the change decreases until the next morning (test 4 and 5), the changes are close to zero, although the records of the SPC show a constantly high amount of drifting particles.

Furthermore we could show that despite differences in environmental conditions between wind tunnel and field tests, the ranges of the mass flux, both based on the surface change and on the particles in the saltation layer are similar, although the shear stress in the field were larger than in the wind tunnel. Our results support what Paterna et al. [2016] reported, that the mass flux decouples from the flow at higher mass fluxes only for the wind tunnel, where the integral time scales of the flow significantly deviates from the one of the mass flux. In the field, the ranges of the integral time scales of the flow and the mass fluxes are similar.

Although particle and surface mass-flux are in the same range for wind tunnel and field measurements, the integration of the particle mass flux along the exponential function (Eq.4.1), which proofed to reflect well the total mass balance in the wind tunnel, did not reflect the

## **Chapter 4. Spatiotemporal dynamics of short term erosion/deposition in drifting and blowing snow**

---

mass in the field measurements. Representing the mass flux profile by a log-normal function did considerably improve the robustness of the integrated particle mass flux. Using a profile function based on the formulation in Eq.4.5 enabled to represent the saltation profile for various conditions wind speeds both in the wind tunnel as well as in the field.

### **Acknowledgements**

The authors wish to express their acknowledgment to Christian Sommer and Andreas Stoffel for their support processing the data from the laser scans. The authors are also thankful to Johnny Gaelens and the staff of the International Polar Foundation in Princess Elizabeth Station in Antarctica for their hospitality and the support acquiring the data in Antarctica. Prof. Kouichi Nishimura provided support and instrumentation for the field measurements. Also the help of the local workshop and electronics team at the SLF (Marco Collet and Andreas Moser) is greatly acknowledged. We further wish to express our gratitude to the Swiss National Science Foundation (SNF) for funding this research (R grant No. 200021-147184) and the wind tunnel facility (R'Equip grant No. 2160-060998).



## 5 Overall summary and conclusions

The main purpose of this work was to investigate spatial and temporal dynamics of surface erosion and deposition in response to snow particle saltation. Experience gained from experiments under controlled conditions in the wind tunnel was evaluated and applied to field experiments which helped to set the wind tunnel experiments in a relation to conditions in the field. The three chapters present address individual topics and objectives: (i) preliminary experiments for the saltation layer; (ii) development and implementation of new hardware to investigate changes on the surface with sufficient spatial and temporal resolution; (iii) application of the new hardware in the field as well as the transfer of knowledge from wind-tunnel measurements to the evaluation of field data, and comparison to wind tunnel results.

In Chapter 2 (Crivelli et al. [2016]) wind-tunnel experiments conducted under different conditions revealed that the mass-flux signals obtained from a snow particle counter (SPC) and shadowgraphic particle tracking velocimetry (PTV) correlate very well. In this work we clarified the impact of different post-processing parameters on the PTV results. Figures 2.8e, 2.8f and 2.12e demonstrate that the correlation and the mass-flux ratio between SPC and PTV converge for sufficiently high thresholds. With optimal settings in the post processing, we were able to have a correlation as high as  $r^2 \geq 0.93$  for calibration experiments and  $r^2 \geq 0.81$  for drifting snow experiments. Our results confirm previous studies that the SPC is more sensitive to smaller particles. Differences in particle numbers and diameter distribution between SPC and PTV are found to originate from different sampling rates, control volumes and the bounded resolution of the SPC. The results suggests that the PTV technique is a valid alternative to the more established SPC in laboratory environments.

In Chapter 3 (Crivelli et al. [2017]) we present a study to establish a link between the dynamics of the erosion and deposition of snow during an event of drifting and blowing snow at the surface and the snow particles in the saltation layer. The Kinect device was employed in wind tunnel experiments as a tool to observe the changes of the snow surface at a sufficient high spatial and temporal resolution. It's accuracy may not be sufficient enough to record individual particles, nevertheless it demonstrated to well quantify the contribution of events of drifting particles to the surface erosion. This study observes an equilibrium between

## Chapter 5. Overall summary and conclusions

---

erosion and deposition at low mass fluxes and a shift to a dominance of erosion at higher mass fluxes. For the comparison of the particle mass flux with the mass eroded we integrated the particle mass flux along an exponential function describing the boundary layer profile. For this function different values for the parameter describing the saltation-length-scale were used. The saltation-length-scale describes the saltation profile throughout the height of the boundary layer. We found a correlation between average surface mass flux consisting of erosion and deposition and particle mass flux over all sets to be  $r^2 = 0.93$ . The correlation could even be improved by focusing on a smaller area of the surface just in front of the SPC. Fitting the sum of the surface changes versus the integrated particle mass-flux showed to have the best fit when the saltation layer was confined near the surface.

Chapter 4 (Crivelli et al. [2018]) compares the spatial and temporal variability of snow surface erosion and deposition recorded from field studies to controlled experiments in a wind tunnel. The presented study analyses the data in a spatial context shows that the surface mass flux is very variable in a small spatial domain. The data recorded in Antarctica shows that formation of a homogeneous distributed pattern of barchan dunes during a storm. Results of the snow surface change from an alpine test site suggests that the evolution of the snow surface has a strong variability in streamwise direction, supposedly due to the formation and traversing of snow wave structures, while reduced variability is observed in cross-wise direction. In terms of temporal dynamics, the data from Antarctica suggests that settlement and sintering have a main influence on the changes of the snow volume. Settlement and sintering seem not to affect the characteristics of the surface structure a lot on a small scale, but the total change in volume is significant. The data shows that main changes in the snow surface structure did only occur after a major storm event with very strong saltation activity over a long period of time. Although there were events of drifting snow before and after the storm, either the scans were too distant from each other, or the drifting was not strong enough. The lack of significant snow surface alteration after the storm may be explained by considering that the drifting event did alter the snow surface in such a way, that the structure withstands further changes even with continuing events of drifting particles. Data at high temporal and spatial resolution from Kinect measurements at the Weissfluhjoch show a similar behavior. The magnitude of the snow surface changes decreased with time even though the magnitude of wind speed and saltation activity remained at a high level. Furthermore the study reveals that despite significant differences in terms of the flow conditions between the field and the wind tunnel exist the ranges of the surface mass flux and particle mass flux are similar. This does not conclusions by Paterna et al. [2016] that the mass flux decouples from the flow and has it's own dynamics. Similar to the the methods in Chapter 3 we integrated the particle mass-flux signal along the saltation profile in order to have an estimation of the total amount of particles in the saltation layer. The study revealed that for the field measurements the exponential profile function did not represent the saltation profile for all given conditions. Therefore a new representation of the profile function using a log-normal distribution was presented.

Limitations to the equipment and methods presented in Chapters 2 - 4 are discussed in the subsequent Chapter Limitations and Outlook.

---

Besides the the work presented within this thesis, the author contributed significantly to two other publications based on data recorded in the wind tunnel.

The first study was published as:

*E. Paterna, P. Crivelli, and M. Lehning. Decoupling of mass flux and turbulent wind fluctuations in drifting snow. Geophysical Research Letters, April 2016. doi: 10.1002/2016GL068171.*

This work investigates the question of what role turbulent eddies play to initiate and maintain drifting snow. Saltating particles are known to cause modification in the momentum flux of the wind [Owen, 1964, Kok et al., 2012]. Recent publications investigated and simulated the coupling between the sediment flux and the moment flux (Naaim-Bouvet et al. [2011], Zwaafink et al. [2014]). Using an ultrasonic anemometer and a digital shadowgraphic system the wind and the saltating particle were recorded in the wind tunnel. The measured time series were analyzed in the frequency domain by investigating the real part of the wavelet co-spectrum for the turbulent streamwise wind fluctuations as well as the horizontal and vertical mass flux. Analyzing these spectra revealed that energy-containing eddies have a more direct influence on the entrainment with weak saltation compared to strong saltation. From this follows that the streamwise turbulent velocity is coupled to the vertical snow transport at weak saltation. At high saltation, the saltation flux decouples from the momentum flux. The decoupling most likely corresponds to an increase in the entrainment of particles via collision of particles and the transfer from energy from the turbulence scales to the large saltation scales. This reveals a turbulent-dependent saltation regime at low saltation scales and a turbulent-independent saltation regime at strong saltation.

The second study was published as:

*E. Paterna, P. Crivelli, and M. Lehning. Wind tunnel observations of weak and strong snow saltation dynamics. Journal of Geophysical Research: Earth Surface, August 2016. doi: 10.1002/2016JF004111.*

Saltation of snow particles starts as soon as the sufficient momentum from the flow is transferred to the particles on the surface. This process is called aerodynamic entrainment. Saltation can also be maintained by the momentum generated due to impacting and rebounding particles [Bagnold, 1941]. The latter process is called splash entrainment. Although the latter can occur at low wind speeds close the threshold for particle entrainment (or even slightly below), we hypothesize that splash entrainment is the dominating mode at strong saltation whilst aerodynamic entrainment refers to weak saltation. In this work we aim associate the two regimes of weak and strong saltation to the two entrainment modes. As for the previous study, an ultrasonic anemometer to record the turbulent wind velocity and a digital shadowgraphic system records the snow particle mass flux, both in streamwise and vertical direction.

Three criteria to associate the mass flux regime to the entrainment mode were suggested.

- In weak saltation we assume the correlation between the increments of the streamwise mass flux and the vertical mass flux to be negative, corresponding to aerodynamic entrainment. In splash entrainment, when upon an impact of one particle, many more

## Chapter 5. Overall summary and conclusions

---

particles are ejected, the correlation between streamwise and vertical mass flux increments is positive.

- Saltation peaks are a clear feature for strong saltation. Hence we aimed to investigate the dependence of saltation peaks on the entrainment mode. The experiments were subdivided in sets of weak and strong saltation based on a previously determined critical saltation strength. We hypothesized that for aerodynamic entrainment, peaks are local and narrow without much mass flux activity before and after. For strong saltation, mass flux peaks were assumed to persist over a longer time leading to wide peaks.
- To distinguish weak from strong saltation the difference in the mass flux growth rate around a saltation peak was analyzed. We modeled an ejection function corresponding to the mean number of particles ejected upon a particles bed collision. The ejection function would therefore model the increment in the averaged vertical mass flux. In case sharp transition between no vertical mass flux to little vertical mass flux, corresponding to aerodynamic entrainment, the ejection function would be high. For strong saltation, the mass flux time increments, and therefore the ejection function would be low.

Analyzing our data for all three criteria revealed that all of them support the hypothesis that for weak saltation regimes, the dominant mode is aerodynamic entrainment, as opposed to strong saltation regimes which may be referred to splash entrainment.

## 6 Limitations and outlook

Within the different chapters, limitations and outlooks were mentioned already. Nevertheless they shall be addressed here in context of the whole work.

Unlike other types of sediments, snow as material is rather complex, consisting of frozen water dependent on many physical variables. In the atmosphere, the structure of new snow is not round, it forms star-shaped, mostly flat, crystals with branches and ramifications to very small structures. These structure are easily broken due to mechanical forces, either from wind, weight or impacts during the aeolian transport. Also for most experimental conditions, snow is close to its melting point. This makes changes in the snow properties very much prone to changes in temperatures and saturation of the air. Little differences in theses properties during the snow accumulation or at the time of the measurements may imply significant changes on the snow characteristics and therefore on the results of the experiments. Already for conditions below the melt point, snow metamorphosis occurs at the scale of the single particles as well as between particles. Inter-particle bonds are created and dissolved such that the properties of the snow change in a mater of minutes to hours. Based on the large susceptibility of snow to mechanical forces and meteorological conditions every snow fall is unique, even within the same snow fall event, the properties of the snow may vary.

Due to availability of snow, experiments in the wind tunnel were conducted between December and beginning of March. In average, 8 to 11 events had sufficient precipitation and favorable meteorological conditions for the experiments. For the measurements in the field, the conditions were even more challenging. A combination between sufficient snow fall and high enough wind speed only allowed experiments during three occasions between January and March 2017.

A few limitations also concerned the experimental setup. For the quantification of drifting and blowing snow in the saltation layer, snow particle counters were used in all studies presented. One main limitation of this instrument is the interpretation of diameter of the snow particles and their representation as spheres in the mass flux calculations. As discussed previously, snow particles form complex structures. Interpreting their volume as spheres does not represent the

## Chapter 6. Limitations and outlook

---

reality in many cases. The SPC does account for that by a limitation of the particle diameters to below 0.5 mm, such that the error between the actual volume and the equivalent sphere volume for larger particles is decreased. Besides these facts, the SPC device was calibrated by the manufacturer before the experiment season. Results in Chapter 2 and Chapter 3 show that despite the limitations, the mass flux calculations show a good correlation between particle mass flux and the surface change.

Another issue with the SPC is the position of the instrument above the snow surface. In the wind tunnel, the instrument could always be adjusted to a position close to the surface. In the field, it was not possible to mount the SPC as near to the surface as in the wind tunnel.

Theory and measurements suggest typical mass flux profiles as a function of the distance from the surface. Due to ongoing erosion and deposition, the distance between sensor and snow surface was not constant during the experiment. Based on the measurement setup, we could not track the exact distance to the snow surface while the experiments were running. This means that no method exists to measure the total vertically integrated flux reliably.

The present work reports the successful integration of the Kinect as a tool to record the snow surface. Nevertheless there are different shortcomings related to the device that need to be addressed.

The first topic is the sensitivity to small scales. The Kinect's resolution is given to be 1 mm, which is in the order of the changes we are interested in. In order to increase precision and reduce noise, the data had to be filtered using a time average filter. Also in the spatial domain, the surface records were averaged over a certain area. This way, the Kinect's precision was within the range we needed (refer to Chapter 3). Another limitation in field experiments was the fact that recordings were only possible in absence of direct sunlight. First experiments demonstrated that the snow surface could not be resolved in daylight based on the fact that infrared sensor of the Kinect was unable to distinguish between the infrared part of the sunlight reflected at the snow surface and the infrared pattern generated by the device itself. Another practical limitation was the amount of data generated from the Kinect's depth stream. Sampling the depth stream at full resolution limited the time of the recording since an immediate processing exceeded the computational power of the computer used for the recordings.

Despite the limitations presented above, the possibility to quantify the changes of the snow surface as a response to drifting snow in a high temporal and spatial resolution offers the potential to resolve new and open question which arose in the process of this thesis.

One main topic worth to investigate further is the formation of snow surface structures. Both in wind tunnel measurements forced by geometrical structures as well as in field studies observing the development of bedform structures such as snow waves or barchan dunes, using the Kinect technology could be very attractive. Particularly for the latter topic it would be very interesting to combine TLS scans with Kinect measurements to combine local surface

---

changes at a high temporal resolution with changes of the surrounding area based on the laser scans.

Another question that arose was an improvement of the saltation profile model for a better representation of the total mass flux. One open question is the influence of the height of the particle counter above the snow surface on the results of the saltation strength as well as how well an exponential function does represent the saltation profile. Both questions may be answered using two or more SPC sensors in a vertical arrangement.

Another topic which needs to be addressed is the influence of sintering to overall change in the snow surface and its effect on the threshold for particle entrainment. To evaluate this topic snow model outputs may be combined with longterm wind tunnel experiments or field experiments.

Furthermore this study revealed significant temporal variation in the potential of the saltation to change the surface. Particularly the results presented in Chapter 4 show that despite ongoing saltation the amplitude of the surface changes decreased. This means that even though snow particles are transported on top of the snow surface, they do not lead to large amounts of erosion or deposition. This raises the question how such a behavior can be implemented in a mass balance on a much larger scale or in model representations.





# Glossary

$A$	Total measurement area
$A_{i,j}$	Average area of pixel $(i, j)$
$L$	Length scale of the saltation system
$L_P$	Length of the footprint of the erosion
$N$	Total number of pixels per frame
$Q$	Total mass flux
$Q_P$	Integrated particle mass flux
$Q_{SB}$	Total set-averaged surface mass flux
$Q_S$	Total time-averaged surface mass flux
$U_{free,t}$	Threshold freestream velocity
$U_{free}$	Freestream velocity
$U_{max}$	Maximal streamwise velocity
$\alpha$	Depth sensor's angle of the FOV along the y-direction
$\beta$	Depth sensor's angle of the FOV along the x-direction
$\kappa$	von Karman constant
$\lambda$	Parameter that defines $L$
$\rho$	Fluid density
$\rho_{snow}$	Snow density
$\tau$	Shear stress
$dV_{i,j}$	Change of volume at pixel $(i, j)$
$d_i$	Particle diameter of the i-th particle

## Chapter 6. Limitations and outlook

---

$d_{min}$	Minimal particle diameter
$dz_{i,j}$	Change in depth at pixel $(i, j)$
$f_s$	Sampling frequency
$g$	Gravitational constant
$h_0$	Height of the SPC measurement location
$m_{DOF}$	Slope function for the DOF
$np_j$	Number of particles for technique $j$ (PTV of SPC)
$p1$	First linear regression parameter
$p2$	Second linear regression parameter
$q$	Generally refers to the mass flux in streamwise direction
$q_0(t)$	Averaged particle mass flux recorded with the SPC
$q_P(z)$	Particle mass flux at height $z$
$q_S(t)$	Surface mass flux over the entire FOV at time $t$
$q_{i,j}$	Mass flux at pixel $(i, j)$
$q_i$	Mass flux of the $i$ -th particle
$t_{exp}$	Exposure time
$u$	Streamwise wind velocity
$u'$	Streamwise wind velocity fluctuation
$u_*$	Shear stress velocity / Friction velocity
$u_{PTV}$	Mean particle velocity of all PRV particles
$v$	Vertical wind velocity
$v'$	Vertical wind velocity fluctuation
$z$	Usually refers to the height above the snow surface
$z_0$	Aerodynamic roughness length
$z_{SL}$	Vertical expansion of the saltation layer
$v_{p_i}$	Particle velocity of the $i$ -th particle

---

CMOS	Complementary metal–oxide–semiconductor, is a technology for constructing integrated circuits
CSAT3B	Ultrasonic anemometer
DOF	Depth of field
FOV	Field of view
FlowCapt	Acoustic sensor to count saltating particles
IR	Infrared
PEA	Princess Elizabeth station in Antarctica
PF	Particle filter threshold
PP	Particle property filter threshold
PR	Particle recognition filter threshold
PSD	Position-sensible photo detector
PSD	Power spectral density
PTV	Particle tracking velocimetry
RAM	Random-access memory, is a form of computer data storage
RF	Reduction factor
RH	Relative humidity
SG	Shadowgraphy, refers to shadowgraphic PTV
SLF	WSL Institute for Snow and Avalanche Research
SNF	Swiss National Science Foundation
SPC	Snow particle counter, refers to the instrument or the technique
TLS	Terrestrial laser scanning, refers to the instrument or the technique
WFJ	SLF field site on Weissfluhjoch
WSL	Swiss Federal Institute for Forest, Snow and Landscape Research



## Bibliography

- N. O. Aksamit and J. W. Pomeroy. Near-surface snow particle dynamics from particle tracking velocimetry and turbulence measurements during alpine blowing snow storms. *The Cryosphere*, 10(6):3043–3062, 2016. doi: 10.5194/tc-10-3043-2016. URL <https://www.the-cryosphere.net/10/3043/2016/>.
- Charles Amory, Hubert Gallée, Florence Naaïm-Bouvet, Vincent Favier, Etienne Vignon, Ghislain Picard, Alexandre Trouvilliez, Luc Piard, Christophe Genthon, and Hervé Belot. Seasonal variations in drag coefficient over a sastrugi-covered snowfield in coastal east antarctica. *Boundary-Layer Meteorology*, 164(1):107–133, Jul 2017. ISSN 1573-1472. doi: 10.1007/s10546-017-0242-5. URL <https://doi.org/10.1007/s10546-017-0242-5>.
- Robert S Anderson and Peter K Haff. Simulation of eolian saltation. *Science*, 241(4867):820–823, 1988. ISSN 0036-8075. doi: 10.1126/science.241.4867.820. URL <http://science.sciencemag.org/content/241/4867/820>.
- R. A. Bagnold. The transport of sand by wind. *The Geographical Journal*, 89(5):409–438, 1937. ISSN 00167398, 14754959. URL <http://www.jstor.org/stable/1786411>.
- RA Bagnold. The movement of desert sand. *Geogr J*, 85(4):342–365, 1935.
- Ralph A Bagnold. The physics of wind blown sand and desert dunes. *Methuen, London*, 265 (10):256 pp, 1941.
- M Bernhardt, GE Liston, U Strasser, G Zängl, and K Schulz. High resolution modelling of snow transport in complex terrain using downscaled mm5 wind fields. *The Cryosphere*, 4(1): 99–113, 2010.
- W. F. Budd. *The Drifting of Nonuniform Snow Particles I*, pages 59–70. American Geophysical Union, 1966. ISBN 9781118664445. doi: 10.1029/AR009p0059. URL <http://dx.doi.org/10.1029/AR009p0059>.
- WF Budd, WRJ Dingle, and U Radok. The byrd snow drift project: outline and basic results. *Studies in Antarctic Meteorology*, pages 71–134, 1966. doi: 10.1029/AR009p0071.
- Katrin Burri, Christof Gromke, Michael Lehning, and Frank Graf. Aeolian sediment transport over vegetation canopies: A wind tunnel study with live plants. *Aeolian R*, 3(2):205–213, 2011. doi: 10.1016/j.aeolia.2011.01.003.

## Bibliography

---

- G. Castellani, C. L  kes, S. Hendricks, and R. Gerdes. Variability of arctic sea-ice topography and its impact on the atmospheric surface drag. *Journal of Geophysical Research: Oceans*, 119(10):6743–6762, 2014. ISSN 2169-9291. doi: 10.1002/2013JC009712. URL <http://dx.doi.org/10.1002/2013JC009712>.
- V Chritin, R Bolognesi, and H Gubler. Flowcapt: a new acoustic sensor to measure snowdrift and wind velocity for avalanche forecasting. *Cold Regions Science and Technology*, 30(1):125 – 133, 1999. ISSN 0165-232X. doi: [https://doi.org/10.1016/S0165-232X\(99\)00012-9](https://doi.org/10.1016/S0165-232X(99)00012-9). URL <http://www.sciencedirect.com/science/article/pii/S0165232X99000129>.
- Andrew Clifton, Jean-Daniel R  edi, and Michael Lehning. Snow saltation threshold measurements in a drifting-snow wind tunnel. *J Glaciol*, 52(179):585–596, 2006. doi: 10.3189/172756506781828430.
- Andrew Clifton, Costantino Manes, Jean-Daniel R  edi, Michele Guala, and Michael Lehning. On shear-driven ventilation of snow. *Boundary-Layer Meteorol*, 126(2):249–261, 2008. doi: 10.1007/s10546-007-9235-0.
- Luigi Colombo and Barbara Marana. Terrestrial laser scanning. *GIM INTERNATIONAL*, (12, vol. 24):17–20, 2010. URL <https://www.gim-international.com/content/article/terrestrial-laser-scanning-2>.
- Francesco Comola and Michael Lehning. Energy and momentum conserving model of splash entrainment in sand and snow saltation. *Geophysical Research Letters*, pages n/a–n/a, 2017. ISSN 1944-8007. doi: 10.1002/2016GL071822. URL <http://dx.doi.org/10.1002/2016GL071822>. 2016GL071822.
- Vaughan Cornish. *Waves of Sand and Snow and the Eddies Which Make Them*. TF Unwin, London, U.K., 1914. ISBN 1153234688.
- P. Crivelli, E. Paterna, S. Horender, and M. Lehning. Quantifying particle numbers and mass flux in drifting snow. *Boundary-Layer Meteorology*, June 2016. doi: 10.1007/s10546-016-0170-9.
- P. Crivelli, E. Paterna, and M. Lehning. Space - time dynamics of erosion/deposition versus horizontal mass flux of snow. 2017.
- P. Crivelli, E. Paterna, N. Wever, and M. Lehning. Spatiotemporal dynamics of short term erosion/deposition in drifting and blowing snow. 2018.
- Ruzica Dadic, Rebecca Mott, Huw J. Horgan, and Michael Lehning. Observations, theory, and modeling of the differential accumulation of antarctic megadunes. *Journal of Geophysical Research: Earth Surface*, 118(4):2343–2353, 2013. ISSN 2169-9011. doi: 10.1002/2013JF002844. URL <http://dx.doi.org/10.1002/2013JF002844>.
- Elham Dolatabadi, Babak Taati, and Alex Mihailidis. Vision-based approach for long-term mobility monitoring: Single case study following total hip replacement. *Journal of rehabilitation research and development*, 51(7):1165–1176, 2014. ISSN 0748-7711. doi: 10.1682/jrrd.2013.12.0263. URL <http://dx.doi.org/10.1682/JRRD.2013.12.0263>.

- Zhibao Dong and Guangqiang Qian. Characterizing the height profile of the flux of wind-eroded sediment. *Environmental Geology*, 51(5):835–845, 2007. ISSN 1432-0495. doi: 10.1007/s00254-006-0363-5. URL <http://dx.doi.org/10.1007/s00254-006-0363-5>.
- Zhibao Dong, Xiaoping Liu, Hongtao Wang, Aiguo Zhao, and Xunming Wang. The flux profile of a blowing sand cloud: a wind tunnel investigation. *Geomorphology*, 49(3&??4):219 – 230, 2003. ISSN 0169-555X. doi: [http://dx.doi.org/10.1016/S0169-555X\(02\)00170-8](http://dx.doi.org/10.1016/S0169-555X(02)00170-8). URL <http://www.sciencedirect.com/science/article/pii/S0169555X02001708>.
- Judith J. Doorschot, Michael Lehning, and Anouck Vrouwe. Field measurements of snow-drift threshold and mass fluxes, and related model simulations. *Boundary-Layer Meteorol*, 113(3):347–368, 2004. ISSN 1573-1472. doi: 10.1007/s10546-004-8659-z. URL <http://dx.doi.org/10.1007/s10546-004-8659-z>.
- Olaf Eisen, Massimo Frezzotti, Christophe Genthon, Elisabeth Isaksson, Olivier Magand, Michiel R. van den Broeke, Daniel A. Dixon, Alexey Ekaykin, Per Holmlund, Takao Kameda, Lars Karlöf, Susan Kaspari, Vladimir Y. Lipenkov, Hans Oerter, Shuhei Takahashi, and David G. Vaughan. Ground-based measurements of spatial and temporal variability of snow accumulation in east antarctica. *Reviews of Geophysics*, 46(2):n/a–n/a, 2008. ISSN 1944-9208. doi: 10.1029/2006RG000218. URL <http://dx.doi.org/10.1029/2006RG000218>. RG2001.
- Kyis Essmaeel, Luigi Gallo, Ernesto Damiani, Giuseppe De Pietro, and Albert Dipanda. Temporal denoising of kinect depth data. In *Signal Image Technology and Internet Based Systems (SITIS), 2012 Eighth International Conference on*, pages 47–52. IEEE, 2012. doi: 10.1109/SITIS.2012.18.
- Kyis Essmaeel, Luigi Gallo, Ernesto Damiani, Giuseppe De Pietro, and Albert Dipanda. Comparative evaluation of methods for filtering kinect depth data. *Multimedia Tools and Applications*, 74(17):1–24, 2014. ISSN 1573-7721. doi: 10.1007/s11042-014-1982-6. URL <http://dx.doi.org/10.1007/s11042-014-1982-6>.
- Simon Filhol and Matthew Sturm. Snow bedforms: A review, new data, and a formation model. *Journal of Geophysical Research: Earth Surface*, 120(9):1645–1669, 2015. ISSN 2169-9011. doi: 10.1002/2015JF003529. URL <http://dx.doi.org/10.1002/2015JF003529>. 2015JF003529.
- M. Frezzotti, S. Gandolfi, and S. Urbini. Snow megadunes in antarctica: Sedimentary structure and genesis. *Journal of Geophysical Research: Atmospheres*, 107(D18):ACL 1–1–ACL 1–12, 2002a. ISSN 2156-2202. doi: 10.1029/2001JD000673. URL <http://dx.doi.org/10.1029/2001JD000673>. 4344.
- Massimo Frezzotti, Stefano Gandolfi, Floriana La Marca, and Stefano Urbini. Snow dunes and glazed surfaces in antarctica: new field and remote-sensing data. *Annals of Glaciology*, 34: 81–88, 2002b. doi: 10.3189/172756402781817851.

## Bibliography

---

- Dale A. Gillette and Theodore R. Walker. Characteristics of airborne particles produced by wind erosion of sandy soil, high plains of west texas. 123(2):97–110, 1977. URL [http://journals.lww.com/soilsci/Fulltext/1977/02000/CHARACTERISTICS\\_OF\\_AIRBORNE\\_PARTICLES\\_PRODUCED\\_BY.4.aspx](http://journals.lww.com/soilsci/Fulltext/1977/02000/CHARACTERISTICS_OF_AIRBORNE_PARTICLES_PRODUCED_BY.4.aspx).
- Mark Gordon and Peter A Taylor. Measurements of blowing snow, part i: Particle shape, size distribution, velocity, and number flux at churchill, manitoba, canada. *Cold Reg Sci Technol*, 55(1):63–74, 2009. ISSN 0165-232X. doi: 10.1016/j.coldregions.2008.05.001. URL <http://www.sciencedirect.com/science/article/pii/S0165232X08000736>.
- Mark Gordon, Sergiy Savelyev, and Peter A Taylor. Measurements of blowing snow, part ii: Mass and number density profiles and saltation height at franklin bay, nwt, canada. *Cold Reg Sci Technol*, 55(1):75–85, 2009. doi: 10.1016/j.coldregions.2008.07.001. URL <http://www.sciencedirect.com/science/article/pii/S0165232X0800102X>.
- Christof Gromke, Costantino Manes, Benjamin Walter, Michael Lehning, and Michele Guala. Aerodynamic roughness length of fresh snow. *Boundary-Layer Meteorol*, 141(1):21–34, 2011. doi: 10.1007/s10546-011-9623-3.
- Christof Gromke, Stefan Horender, Benjamin Walter, and Michael Lehning. Snow particle characteristics in the saltation layer. *J Glaciol*, 60(221):431–439, 2014. doi: 10.3189/2014JoG13J079.
- CD Groot Zwaafink, A Cagnati, A Crepaz, C Fierz, G Macelloni, M Valt, and M Lehning. Event-driven deposition of snow on the antarctic plateau: analyzing field measurements with snowpack. *The Cryosphere*, 7(1):333–347, 2013. doi: 10.5194/tc-7-333-2013.
- T. Grünwald, M. Schirmer, R. Mott, and M. Lehning. Spatial and temporal variability of snow depth and ablation rates in a small mountain catchment. *Cryosphere*, 4(2):215–225, 2010. doi: 10.5194/tc-4-215-2010. cited By 0.
- M Guala, Costantino Manes, A Clifton, and M Lehning. On the saltation of fresh snow in a wind tunnel: profile characterization and single particle statistics. *J Geophys Res: Earth Surface (2003–2012)*, 113(F3), 2008. doi: 10.1029/2007JF000975.
- M. Hämmerle, B. Höfle, J. Fuchs, A. Schröder-Ritzrau, N. Vollweiler, and N. Frank. Comparison of kinect and terrestrial lidar capturing natural karst cave 3-d objects. *IEEE Geoscience and Remote Sensing Letters*, 11(11):1896–1900, Nov 2014. ISSN 1545-598X. doi: 10.1109/LGRS.2014.2313599.
- R Kawamura. Sand movement by wind. *Kagaku*, 18(11):24–30, 1948.
- Ryuma Kawamura. Study on sand movement by wind (relationship between sand flow and wind friction, and vertical density distribution of sand). *Tokyo Daigaku Rikogaku Kenkyusho Hokoku, (Tokyo)*, 5(3):95–112, 1951.



- Ki Seong Kim and Sung-Soo Kim. Drop sizing and depth-of-field correction in tv imaging. *Atomization and Sprays*, 4(1):65–78, 1994. doi: 10.1615/AtomizSpr.v4.i1.30.
- Maruyama T. Ishimaru T. Kimura, T. Design and making of spc-vii. pages 665 – 670, 1993.
- Shun’ichi Kobayashi and Tamotu Ishida. Interaction between wind and snow surface. *Boundary-Layer Meteorology*, 16(1):35–47, Mar 1979. ISSN 1573-1472. doi: 10.1007/BF02220405. URL <https://doi.org/10.1007/BF02220405>.
- Jasper F Kok and Nilton O Renno. A comprehensive numerical model of steady state saltation (comsalt). *Journal of Geophysical Research: Atmospheres (1984–2012)*, 114(D17), 2009.
- Jasper F Kok, Eric JR Parteli, Timothy I Michaels, and Diana Bou Karam. The physics of wind-blown sand and dust. *Reports on Progress in Physics*, 75(10):106901, 2012.
- Kenji Kosugi, Kouichi Nishimura, and Norikazu Maeno. Snow ripples and their contribution to the mass transport in drifting snow. *Boundary-Layer Meteorology*, 59(1):59–66, Apr 1992. ISSN 1573-1472. doi: 10.1007/BF00120686. URL <https://doi.org/10.1007/BF00120686>.
- LaVision-GmbH. Product-manual for davis 8.0. pages 9–46, 2011.
- M. Lehning, F Naaim, M. Naaim, B. Brabec, J. Doorschot, Y. Durand, G. Guyomarc’h, J.-L. Michaux, and M. Zimmerli. Snow drift: acoustic sensors for avalanche warning and research. *Natural Hazards and Earth System Science*, 2(3/4):121–128, 2002. URL <https://hal.archives-ouvertes.fr/hal-00330878>.
- Mathias Lemmens. Terrestrial laser scanning. In *Geo-information*, pages 101–121. Springer, 2011. ISBN 978-94-007-1667-4. doi: 10.1007/978-94-007-1667-4\_6.
- Kenneth David Mankoff and Tess Alethea Russo. The kinect: A low-cost, high-resolution, short-range 3d camera. *Earth Surface Processes and Landforms*, 38(9):926–936, 2012.
- R Meister. Influence of strong winds on snow distribution and avalanche activity. *Annals of Glaciology*, 13:195–201, 1988.
- ROLAND Meister. Wind systems and snow transport in alpine topography. *IAHS Publ*, 162: 265–279, 1987.
- M Mellor. Gauging antarctic drift snow. *Antarctic Meteorology*, pages 347–354, 1960.
- J-L Michaux, F Naaim-Bouvet, M Naaim, M Lehning, and G Guyomarc’h. Effect of unsteady wind on drifting snow: first investigations. *Natural Hazards and Earth System Science*, 2(3/4):129–136, 2002.
- R. L. Miller, R. V. Cakmur, J. Perlwitz, I. V. Geogdzhayev, P. Ginoux, D. Koch, K. E. Kohfeld, C. Prigent, R. Ruedy, G. A. Schmidt, and I. Tegen. Mineral dust aerosols in the nasa goddard institute for space sciences modele atmospheric general circulation model. *Journal of Geophysical Research: Atmospheres*, 111(D6):n/a–n/a, 2006. ISSN 2156-2202. doi: 10.1029/2005JD005796. URL <http://dx.doi.org/10.1029/2005JD005796>. D06208.

## Bibliography

---

- Rebecca Mott, Michael Schirmer, M Bavay, T Grünewald, and M Lehning. Understanding snow-transport processes shaping the mountain snow-cover. *The Cryosphere*, 4(4):545–559, 2010.
- Florence Naaim-Bouvet, Herve Bellot, and Mohamed Naaim. Back analysis of drifting-snow measurements over an instrumented mountainous site. *Annals of Glaciology*, 51:207 – 217, 2010. doi: 10.3189/172756410791386661.
- Florence Naaim-Bouvet, Mohamed Naaim, Herv Bellot, and Kouichi Nishimura. Wind and drifting-snow gust factor in an alpine context. *Annals of Glaciology*, 52(58):223–230, 2011. doi: 10.3189/172756411797252112.
- Philip Nalpanis, J. C. R. Hunt, and C. F. Barrett. Saltating particles over flat beds. *Journal of Fluid Mechanics*, 251:661–685, 06 1993. doi: 10.1017/S0022112093003568. URL <https://www.cambridge.org/core/article/saltating-particles-over-flat-beds/8DE2946DC16791422597F8AA2E10261C>.
- M. Nemoto and K. Nishimura. Numerical simulation of snow saltation and suspension in a turbulent boundary layer. *Journal of Geophysical Research: Atmospheres*, 109(D18):n/a–n/a, 2004. ISSN 2156-2202. doi: 10.1029/2004JD004657. URL <http://dx.doi.org/10.1029/2004JD004657>. D18206.
- J.R Ni, Z.S Li, and C Mendoza. Vertical profiles of aeolian sand mass flux. *Geomorphology*, 49(3):205 – 218, 2003. ISSN 0169-555X. doi: [https://doi.org/10.1016/S0169-555X\(02\)00169-1](https://doi.org/10.1016/S0169-555X(02)00169-1). URL <http://www.sciencedirect.com/science/article/pii/S0169555X02001691>.
- Lindsey I. Nicholson, Michał Pełlicki, Ben Partan, and Shelley MacDonell. 3-d surface properties of glacier penitentes over an ablation season, measured using a microsoft xbox kinect. *Cryosphere*, 10(5):1897 – 1913, 2016. ISSN 19940416. URL <http://search.ebscohost.com/login.aspx?direct=true&AuthType=ip&db=asx&AN=118322388&site=eds-live>.
- K. Nishimura and J. C. R. Hunt. Saltation and incipient suspension above a flat particle bed below a turbulent boundary layer. *Journal of Fluid Mechanics*, 417:77–102, 2000. doi: 10.1017/S0022112000001014.
- K Nishimura, K Sugiura, M Nemoto, and N Maeno. Measurements and numerical simulations of snow-particle saltation. *Ann Glaciol*, 26:184–190, 1998.
- Kouichi Nishimura and Masaki Nemoto. Blowing snow at mizuho station, antarctica. *Philos Trans Roy Soc*, 363(1832):1647–1662, 2005. doi: 10.1098/rsta.2005.1599.
- P Rr Owen. Saltation of uniform grains in air. *J. Fluid Mech*, 20(2):225–242, 1964.
- E. Paterna, P. Crivelli, and M. Lehning. Decoupling of mass flux and turbulent wind fluctuations in drifting snow. *Geophys Res Lett*, pages n/a–n/a, 2016. ISSN 1944-8007. doi: 10.1002/2016GL068171. URL <http://dx.doi.org/10.1002/2016GL068171>. 2016GL068171.

- E. Paterna, P. Crivelli, and M. Lehning. Wind tunnel observations of weak and strong snow saltation dynamics. *Journal of Geophysical Research: Earth Surface*, pages n/a–n/a, 2017. ISSN 2169-9011. doi: 10.1002/2016JF004111. URL <http://dx.doi.org/10.1002/2016JF004111>. 2016JF004111.
- Chris Petrich, Hajo Eicken, Christopher M. Polashenski, Matthew Sturm, Jeremy P. Harbeck, Donald K. Perovich, and David C. Finnegan. Snow dunes: A controlling factor of melt pond distribution on arctic sea ice. *Journal of Geophysical Research: Oceans*, 117(C9):n/a–n/a, 2012. ISSN 2156-2202. doi: 10.1029/2012JC008192. URL <http://dx.doi.org/10.1029/2012JC008192>. C09029.
- Ghislain Picard, Laurent Arnaud, Jean-Michel Panel, and Samuel Morin. Design of a scanning laser meter for monitoring the spatio-temporal evolution of snow depth and its application in the alps and in antarctica. *The Cryosphere*, 10:1495 – 1511, 2016. doi: 10.5194/tc-10-1495-2016. URL <https://hal-insu.archives-ouvertes.fr/insu-01392026>.
- ML Pokorny and S Horender. Measurement of particle rotation in a saltation layer. *Earth Surf Process Landf*, 39(13):1803–1811, 2014. doi: 10.1002/esp.3568.
- J. W. Pomeroy and D. M. Gray. Saltation of snow. *Water Resources Research*, 26(7):1583–1594, 1990. ISSN 1944-7973. doi: 10.1029/WR026i007p01583. URL <http://dx.doi.org/10.1029/WR026i007p01583>.
- JW Pomeroy. Transport and sublimation of snow in wind-scoured alpine terrain. *Snow, Hydrology and Forests in Alpine Areas*, edited by: Bergman, H., Lang, H., Frey, W., Issler, D., and Salm, B., IAHS Press, 205:131–140, 1991.
- A. Prochazka, M. Schatz, F. Centonze, J. Kuchynka, O. Vsata, and M. Valis. Extraction of breathing features using ms kinect for sleep stage detection. *Signal, Image and Video Processing*, 10(7):1279–1286, 2016. doi: 10.1007/s11760-016-0897-2. cited By 0.
- Soerensen M. & Willets B.B. Rasmussen, K.R. Measurement of saltation and wind strength on beaches. volume 2, pages 301–325, 1985.
- Michael Schirmer, Michael Lehning, and Jürg Schweizer. Statistical forecasting of regional avalanche danger using simulated snow-cover data. *J Glaciol*, 55(193):761–768, 2009. doi: 10.3189/002214309790152429.
- Hermann Schlichting, Klaus Gersten, Egon Krause, and Herbert Oertel. *Boundary-layer theory*, volume 7. Springer, 9 edition, 1955. ISBN 978-3-662-52919-5. doi: 10.1007/978-3-662-52919-5.
- RA Schmidt. *A system that measures blowing snow*. Rocky Mountain Forest and Range Experiment Station, Forest Service, US Department of Agriculture, 1977.
- RA Schmidt. Threshold wind-speeds and elastic impact in snow transport. *Journal of Glaciology*, 26:453–467, 1980.

## Bibliography

---

- RA Schmidt. Properties of blowing snow. *Reviews of Geophysics*, 20(1):39–44, 1982.
- RA Schmidt. Transport rate of drifting snow and the mean wind speed profile. *Boundary-Layer Meteorol*, 34(3):213–241, 1986. ISSN 1573-1472. doi: 10.1007/BF00122380.
- R.A. Schmidt, Roland Meister, and Hansueli Gubler. Comparison of snow drifting measurements at an alpine ridge crest. *Cold Regions Science and Technology*, 9(2):131 – 141, 1984. ISSN 0165-232X. doi: [http://dx.doi.org/10.1016/0165-232X\(84\)90005-3](http://dx.doi.org/10.1016/0165-232X(84)90005-3). URL <http://www.sciencedirect.com/science/article/pii/0165232X84900053>.
- Simon Schneiderbauer and Alexander Prokop. The atmospheric snow-transport model: Snow-drift3d. *Journal of Glaciology*, 57(203):526–542, 2011.
- Yaping Shao and An Li. Numerical modelling of saltation in the atmospheric surface layer. *Boundary-Layer Meteorology*, 91(2):199–225, May 1999. ISSN 1573-1472. doi: 10.1023/A:1001816013475. URL <https://doi.org/10.1023/A:1001816013475>.
- Christian G. Sommer, Michael Lehning, and Charles Fierz. Wind tunnel experiments: Influence of erosion and deposition on wind-packing of new snow. *Frontiers in Earth Science*, 6:4, 2018. ISSN 2296-6463. doi: 10.3389/feart.2018.00004. URL <https://www.frontiersin.org/article/10.3389/feart.2018.00004>.
- JE Stout and TM Zobeck. Intermittent saltation. *Sedimentology*, 44(5):959–970, 1997.
- Roland B. Stull. *An Introduction to Boundary Layer Meteorology*, volume 13. Springer, Dordrecht, 2012. ISBN 978-94-009-3027-8. doi: 10.1007/978-94-009-3027-8.
- Konosuke Sugiura, Kouichi Nishimura, Norikazu Maeno, and Tadashi Kimura. Measurements of snow mass flux and transport rate at different particle diameters in drifting snow. *Cold Reg Sci Technol*, 27(2):83–89, 1998. doi: 10.1016/S0165-232X(98)00002-0.
- Masao Takeuchi. Vertical profile and horizontal increase of drift-snow transport. *Journal of Glaciology*, 26(94):481–492, 1980. doi: 10.3189/S0022143000010996.
- Ernesto Trujillo, Jorge A. Ramírez, and Kelly J. Elder. Topographic, meteorologic, and canopy controls on the scaling characteristics of the spatial distribution of snow depth fields. *Water Resources Research*, 43(7):n/a–n/a, 2007. ISSN 1944-7973. doi: 10.1029/2006WR005317. URL <http://dx.doi.org/10.1029/2006WR005317>. W07409.
- Ernesto Trujillo, Katherine Leonard, Ted Maksym, and Michael Lehning. Changes in snow distribution and surface topography following a snowstorm on antarctic sea ice. *Journal of Geophysical Research: Earth Surface*, 121(11):2172–2191, 2016. ISSN 2169-9011. doi: 10.1002/2016JF003893. URL <http://dx.doi.org/10.1002/2016JF003893>. 2016JF003893.
- David G Vaughan. Recent trends in melting conditions on the antarctic peninsula and their implications for ice-sheet mass balance and sea level. *Arctic, Antarctic, and Alpine Research*, 38(1):147–152, 2006. doi: 10.1657/1523-0430(2006)038[0147:RTIMCO]2.0.CO;2.

- V. Vionnet, G. Guyomarc'h, F. Naaim Bouvet, E. Martin, Y. Durand, H. Bellot, C. Bel, and P. Pugliese. Occurrence of blowing snow events at an alpine site over a 10-year period: Observations and modelling. *Advances in Water Resources*, 55:53 – 63, 2013. ISSN 0309-1708. doi: <http://doi.org/10.1016/j.advwatres.2012.05.004>. URL <http://www.sciencedirect.com/science/article/pii/S0309170812001145>. Snow and Atmosphere Interactions and Hydrological Consequences.
- B Walter, S Horender, C Voegeli, and M Lehning. Experimental assessment of owen's second hypothesis on surface shear stress induced by a fluid during sediment saltation. *Geophys Res Lett*, 41(17):6298–6305, 2014. doi: 10.1002/2014GL061069.
- Benjamin Walter, C Gromke, K Leonard, A Clifton, and Michael Lehning. Spatially resolved skin friction velocity measurements using irwin sensors: a calibration and accuracy analysis. *J Wind Eng Ind Aerodyn*, 104:314–321, 2012a. doi: 10.1016/j.jweia.2012.02.018.
- Benjamin Walter, Christof Gromke, and Michael Lehning. Shear-stress partitioning in live plant canopies and modifications to raupach's model. *Boundary-Layer Meteorol*, 144(2): 217–241, 2012b. doi: 10.1007/s10546-012-9719-4.
- Benjamin Walter, Christof Gromke, Katherine C Leonard, Costantino Manes, and Michael Lehning. Spatio-temporal surface shear-stress variability in live plant canopies and cube arrays. *Boundary-Layer Meteorol*, 143(2):337–356, 2012c. doi: 10.1007/s10546-011-9690-5.
- E. Yavsan and A. Ucar. Gesture imitation and recognition using kinect sensor and extreme learning machines. *Measurement: Journal of the International Measurement Confederation*, 94:852–861, 2016. doi: 10.1016/j.measurement.2016.09.026. cited By 0.
- Charles S. Zender, David Newman, and Omar Torres. Spatial heterogeneity in aeolian erodibility: Uniform, topographic, geomorphic, and hydrologic hypotheses. *Journal of Geophysical Research: Atmospheres*, 108(D17):n/a–n/a, 2003. ISSN 2156-2202. doi: 10.1029/2002JD003039. URL <http://dx.doi.org/10.1029/2002JD003039>. 4543.
- CD Groot Zwaafink, M Diebold, S Horender, J Overney, G Lieberherr, MB Parlange, and M Lehning. Modelling small-scale drifting snow with a lagrangian stochastic model based on large-eddy simulations. *Boundary-Layer Meteorol*, 153(1):117–139, 2014. doi: 10.1007/s10546-014-9934-2.



## Personal details

Philip Crivelli  
Bahnhofstrasse 4  
7270 Davos Platz

[philipcrivelli@hotmail.com](mailto:philipcrivelli@hotmail.com)

[philip.crivelli@slf.ch](mailto:philip.crivelli@slf.ch)

+41 79 540 26 90

+41 81 417 02 58



Date of birth: 16. Oktober 1985  
Nationality: Swiss  
Marital status: Married  
Languages: German, English, French

## Education

---

Since 2013	<b>WSL Institut for Snow und Avalanche Reserch, SLF, Davos</b> PhD Student, Team Snow cover and Micro - meteorology
2011 – 2012	<b>ETH-Zurich, Masters-Studies</b> Mechanical Engineering Focus: Rehabilitation Engineering
Master-Thesis	Influence of course setting on skiers mechanics in alpine ski racing, ETH Zurich, SLF Davos, NIH Oslo
2007 – 2011	<b>ETH-Zurich, Bachelors-Studies</b> Mechanical Engineering Fokus: Biomedical Engineering
Bachelor Thesis	Completion of construction and commissioning of an automated, highthroughput mechanical testing

apparatus for tissue-engineered constructs, ETH  
Zürich

2000 – 2005

**Schweizerisches Sportgymnasium Davos SSGD,**  
Matura

## Akademic Experience

---

Winter/Spring 2012/2013

**Norwegian Ski Federation, Scientific Staff**

- Evaluation of videoanalysis and mechanical analysis

**SLF Davos/NIH Oslo, Internship**

- Data Interpretation: Influence of the course setting on the skiers mechanics in alpine ski racing

Winter 2012/2013

**NIH Oslo, Scientific Staff**

- Biomechanics in Powerlifting

Summer/Fall 2010

**SLF / Bächler Top Track AG, Industrial internship**

- Implementation of a prototype for a measurement-tool
- Developing of software in Labview
- Realization of a measurement tool.
- Realization of the field tests according project guidelines

Winter 2008

**HILTI AG, Schaan FL, Manufacturing internship**

- Skill workshop for mechanical engineers

## Interests

---

Sports

Ski, Alpinism, Mountainbike, Trailrunning

Traveling & foreign cultures

Voluntary work

Ski Club Davos – Leader Resort Alpine

Guiding for ‘Kids on Bike’



